

American University in Cairo

AUC Knowledge Fountain

Theses and Dissertations

2-1-2013

Carbon nanotubes-cellulose acetate nanocomposites: membranes for water desalination

Nouran Ashraf El Badawi

Follow this and additional works at: <https://fount.aucegypt.edu/etds>

Recommended Citation

APA Citation

El Badawi, N. (2013). *Carbon nanotubes-cellulose acetate nanocomposites: membranes for water desalination* [Master's thesis, the American University in Cairo]. AUC Knowledge Fountain.

<https://fount.aucegypt.edu/etds/1197>

MLA Citation

El Badawi, Nouran Ashraf. *Carbon nanotubes-cellulose acetate nanocomposites: membranes for water desalination*. 2013. American University in Cairo, Master's thesis. *AUC Knowledge Fountain*.

<https://fount.aucegypt.edu/etds/1197>

This Thesis is brought to you for free and open access by AUC Knowledge Fountain. It has been accepted for inclusion in Theses and Dissertations by an authorized administrator of AUC Knowledge Fountain. For more information, please contact mark.muehlhaeusler@aucegypt.edu.

THE AMERICAN UNIVERSITY IN CAIRO
Department of Chemistry

Carbon Nanotubes-Cellulose Acetate Nanocomposites

Membranes for Water Desalination

By

Nouran Ashraf

BS, Chemistry, The American University in Cairo, 2006

Advisors:

Dr. Adham Ramadan

Department of Chemistry

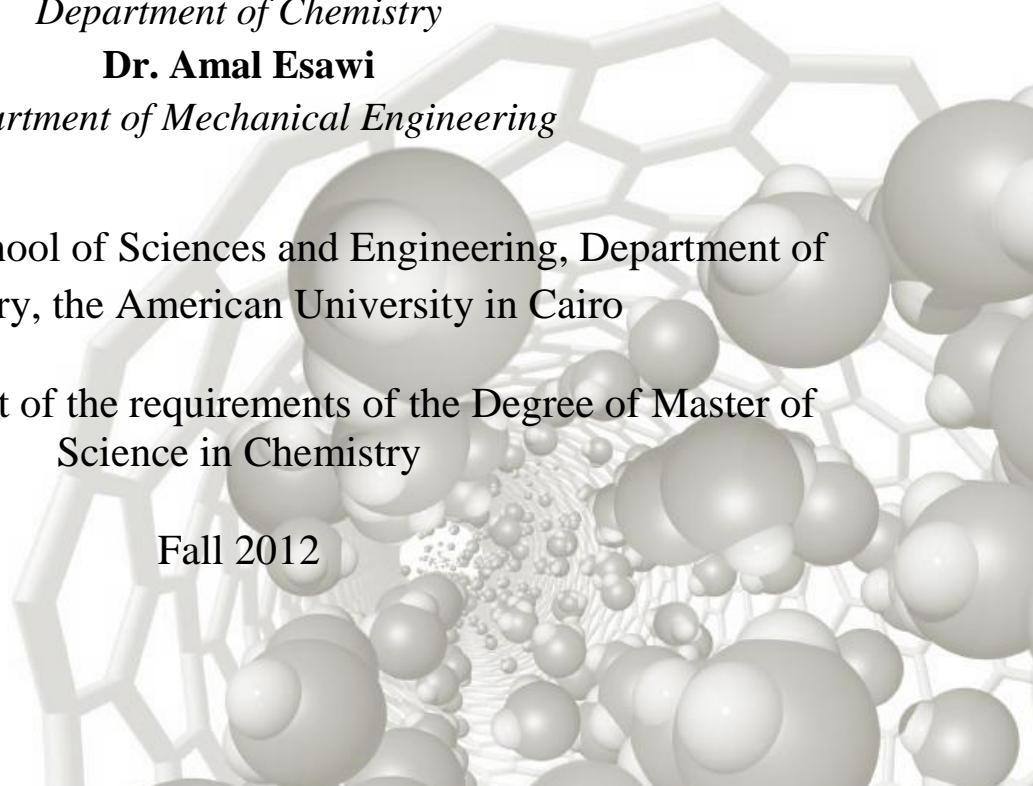
Dr. Amal Esawi

Department of Mechanical Engineering

Submitted to the School of Sciences and Engineering, Department of
Chemistry, the American University in Cairo

In partial fulfillment of the requirements of the Degree of Master of
Science in Chemistry

Fall 2012



*To the martyrs of January 25th revolution,
May you all rest in heaven*

Abstract

Cellulose acetate (CA) ($M_w = 52,000$ Da) membranes were prepared by phase inversion (PI) using acetone as a solvent. Investigation of different preparation conditions were carried out. The effect of membrane casting thickness, CA content, coagulation bath temperature (PI temperature), solvent evaporation, addition of a non-solvent (deionized water), and addition of multi-walled carbon nanotubes (MWCNTs) on membrane morphology and performance (permeation rates and salt rejection rates) were investigated. Membranes morphologies were studied using scanning electron microscopy (SEM). Membranes permeations rates and salt rejection rates were investigated using 1000 ppm NaCl solution. Optimum conditions for developing a CA based nanocomposites were attained, entailing 15 wt% CA content, 20 wt% H₂O non-solvent additive, low functionalized CNTs contents (0.0005, 0.005, and 0.01 wt%), PI at room temperature, and sonication time for CNTs proper dispersion less than 1 minute.

MWCNTs/CA nanocomposites membranes were prepared. MWCNTs were first functionalized by oxidation purification in a strong acidic medium to enhance their dispersion within the polymer matrix, and the success of the functionalization of MWCNTs was characterized using Fourier transform infrared (FTIR) spectroscopy. The nanocomposites morphologies were characterized by several methods by SEM and nitrogen adsorption. SEM images showed large networks of MWCNTs, randomly oriented and properly dispersed, with a significant decrease in the number of macrovoids development with CNT content increase at the same final thickness of the nanocomposites. This was verified by analysis of pore sizes (differential volumes and surface areas), which were found to decrease with the increase in CNT content. Nanocomposites permeations rates and salt rejection rates were investigated using 1000 ppm NaCl solution, and it was found that permeation improved significantly with the addition of CNTs, with the improvement being highest for lowest CNT content. Salt rejection was found to decrease with the presence of CNTs. However the decrease was minimal for low CNT contents. In this respect, it was possible to prepare CA-CNT nanocomposite membranes with improved permeation of 19.57 L/m²h, together with a minimal decrease of salt retention performance of 69.4% at 24 bars operating pressure. The membranes performance could be explained by membrane morphology (surface areas and porosity).

Acknowledgment

I would like to deeply thank my advisor and mentor Dr. Adham Ramadan and my co-advisor Dr. Amal Esawi for giving me the time, effort, and guidance to carry out this project. Their encouragement, patience, and constructive feedbacks were such a positive energy that kept me going until seeing this through. Their moral support on all matters, academic and personal significantly affected my life as a whole, not only my research skills. No words will ever fulfill my gratitude, and I am really honored to have them as my advisors. Thank you.

I would also like to express my deep appreciation for the Youssef Jameel Science and Technology Research Center (YJSTRC) for their financial support, through a full fellowship, over my years of study for the Masters degree in Chemistry. I cannot fail to mention Dr. Sherif Sedky, the former director of YJSTRC, who always believed in me, and Dr. Ehab Abdel Rahman, the current director of YJSTRC, who always encouraged me. This has been a wonderful research experience in a well renowned facility. I also want to thank Eng. Rami Wasfi, Dr. Omar Zaki, and Eng. Ehab Salama, for training me on how to use some of the equipment in the research center, for, without them, I wouldn't have been able to carry on the work done.

I also wish to thank the faculty and staff members of the Chemistry Department who have always had their doors wide open for all students who needed help in any matter. I would specially like to thank Dr. Nahed Yaqoub for her time in aiding me with many of the calculations carried out. The Chemistry Department has been my second home for more than eleven years. It is the place which expanded my horizon to new possibilities, and offered me new chances of education and achievements. It is the place where I have a real sense of belonging.

I would also like to thank Dr. Mohammed Morsi, Mechanical Engineering Department, for helping me carry out the permeation measurements. His time and effort are greatly appreciated.

On more personal bases, I would love to thank my parents for being my lighthouse when life darkened the most. Their unconditional love and devotion humble me. No daughter can ever have better parents, for they are, and forever will be my comfort zone.

I would also love to thank my best friends Haidy Youssef, Noha Khattab, Samaa Nawaar, Dina Nemr, and Ayaat Mahmoud for being there for me all the time and never letting me down.

Last, I wish to express my gratefulness, love, and admiration to my *Tahrir* buddies: Hany el Kady, Ayaat Mahmoud, Dina Nemr, Mahmoud Bizzari, Samaa Nawaar, Essam Omar, Nada Nashaat, Nadeem Gawad, Ramy el Gohari, Haidy Youssef, Hani Tawfeek, and Amr Zeid. These people are treasure. They had my back, cherished my life over theirs, and helped me survive the past two years both psychologically and physically. I owe them more than I can possibly pay back, and I am really blessed to have them in my life.

Thank you all for an overwhelming wonderful and challenging experience.

Contents

Abstract.....	ii
Acknowledgment.....	iii
List of Figures.....	vii
List of Tables.....	xiii
List of Abbreviations.....	xiv
1 Introduction.....	1
1.1 History.....	2
1.2 Desalination Technologies.....	2
1.2.1 Multi-Stage Flash (MSF).....	3
1.2.2 Multiple-Effect Distillation (MED).....	4
1.2.3 Reverse Osmosis (RO).....	5
1.2.4 Other Processes.....	7
2 Literature Background.....	9
2.1 Introduction.....	10
2.2 Effect of Different Additives.....	10
2.2.1 Effect of Solvents and Non-Solvents.....	10
2.2.2 Effect of Pore Formers.....	13
2.2.3 Effect of Using Polymer Blends.....	17
2.2.4 Effect of Inorganic Additives.....	21
2.2.5 Effect of Using Carbon Nanotubes.....	22
2.3 Research Aim.....	26
3 Theoretical Background.....	27
3.1 Cellulose Acetate in Desalination.....	28
3.1.1 CA Structure and Properties.....	28
3.1.2 CA Membrane Preparation.....	29
3.2 Permeation and Retention Rates Calculation.....	32
3.3 Nanocomposites.....	34
3.4 Carbon Nanotubes as Nanofillers.....	35
3.4.1 CNTs Structure and Properties.....	35
3.4.2 Functionalization of CNTs by Oxidation Purification.....	37

3.4.3	CNTs in Water Desalination and Treatment	38
3.5	Inside CNTs Molecular Dynamics (MD).....	38
3.6	Membrane Characterization	41
3.6.1	Scanning Electron Microscope (SEM).....	41
3.6.2	Surface Analysis by Gas Sorption.....	42
4	Experimental	49
4.1	Materials Used.....	50
4.2	Stock Solutions Preparation	50
4.2.1	CA Stock Solution.....	50
4.2.2	CA Stock Solution with Pristine (non-functionalized) Carbon Nanotubes (pNTs)	50
4.2.3	CA Stock Solution with Functionalized CNTs (fNTs)	51
4.3	Methods and Instrumentation.....	51
4.3.1	Functionalization of Carbon Nanotubes.....	51
4.3.2	Membrane Casting	52
4.3.3	Sample Surface Area and Porosity Determination.....	52
4.3.4	Infrared Analysis	53
4.3.5	Scanning Electron Microscopy	53
4.3.6	Liquid Test Cell.....	53
4.4	Investigating Preparation Conditions	54
4.4.1	Membrane Casting Thickness	55
4.4.2	Coagulation Bath Temperature (CBT) (PI Temperature)	57
4.4.3	CA Content.....	57
4.4.4	Solvent Evaporation	57
4.4.5	Addition of H ₂ O (Non-Solvent)	58
4.4.6	Addition of CNTs.....	59
4.5	Optimal Preparation Conditions Samples	60
5	Results and Discussion	61
5.1	Effect of Preparation Conditions on Membranes Morphology.....	62
5.1.1	Membrane Casting Thickness	63
5.1.2	Coagulation Bath Temperature (CBT).....	67
5.1.3	CA Content.....	70

5.1.4	Solvent Evaporation	73
5.1.5	Addition of H ₂ O (Non-Solvent)	77
5.1.6	Addition of CNTs	82
5.2	Optimal Preparation Conditions	91
5.3	Membrane Surface Properties	92
5.3.1	Differential Pore Sizes	92
5.3.2	Adsorption Isotherms	97
5.3.3	The t-Plots	99
5.4	Membranes Performance	102
5.4.1	Permeation Rates	102
5.4.2	Salt Retention Rates	103
5.4.3	BET Surface Areas	105
5.4.4	Membrane Morphology and Performance: General Discussion	107
6	Conclusions	112
6.1	Conclusion	113
6.2	Future Work	114
	References	116
	Appendix I	124

List of Figures

Image on the front page is the cover page of nanotoday, vol.6, no. 2, December 2007

Figure 1.1 Desalination saline sources % worldwide [11]	3
Figure 1.2 Desalination processes % worldwide [11]	3
Figure 1.3 Diagram of Multi Stage Flash Process [13]	4
Figure 1.4 Diagram of Multiple Effect Distillation Process [13]	5
Figure 1.5 Osmosis and Reverse Osmosis flow [17].....	6
Figure 1.6 Pore size distribution of each membrane type [14].....	7
Figure 2.1 Flux rates vs. Rejection rates of 2000 ppm NaCl solution for temperature ranges of 60,65, 70, 75, and 80°C, (a) data of 20 wt% cellulose acetate membranes, (b) data of 22 wt% cellulose acetate membranes [23].....	12
Figure 2.2 Pure water flux and BSA rejection rates vs. Pluronic F127 content [26].....	14
Figure 2.3 (a) SEM of blank cellulose acetate membrane in pure water gelation medium, (b) SEM of cellulose acetate membrane with 30 wt% silica nanoparticles prepared in HCl gelation medium (pH 1) [33].....	17
Figure 2.4 Effect of PVP wt% on metal ions rejection: (a) blank cellulose acetate, (b) 75/25 wt% CA/PSF [31]	18
Figure 2.5 SEM of the effect of PVP on morphology; (a) 2.5 wt% PVP in 100/0 wt% CA/PSF respectively, (b) 7.5 wt% PVP in 100/0 wt% CA/PSF respectively, (c) 2.5 wt% PVP in 75/15 wt% CA/PSF respectively, (d) 7.5 wt% PVP in 75/15 wt% CA/PSF respectively [31].....	19
Figure 2.6 ^{31}P NMR of $(\text{HPO}_4)^{2-}$ vs. $\text{Zr}(\text{HPO}_4)^{2-}$. (a) singlet of phosphorous of $(\text{HPO}_4)^{2-}$, (b) singlet of phosphorous of $\text{Zr}(\text{HPO}_4)^{2-}$ [36]	21
Figure 2.7 SEM of the cross section of CNTs/PSF membrane, (a) 0 wt% CNTs blank PSF membrane, (b) 2 wt% CNTs/PSF membrane [38].....	23
Figure 2.8 MWCNTs contents effect on PWF and PEG rejection rates [39].....	24
Figure 2.9 A schematic representation of how CNTs concentration can block pores, thus reduce pore sizes [40].....	25
Figure 3.1 Membrane lifetime vs. pH [48]	29
Figure 3.2 Schematic diagram of a film applicator and a casting knife	29

Figure 3.3 Interpretation of the demixing process	30
Figure 3.4 Chart elaborating the effect of solvents on membrane morphology [51].....	31
Figure 3.5 Schematic representation of an asymmetric membrane developed via PI, modified from [52]	32
Figure 3.6 Permeation cell (modified from [29]).....	33
Figure 3.7 Illustration of how the particle number increase as their sizes decrease in a given volume [61]	34
Figure 3.8 (a), (b), (c) SWCNTs different structures with highlight on C-C bond orientation vs. the nanotube axis [67], (d) MWCNTS structure [63].....	36
Figure 3.9 (a) (n, m) vector indication [64], (b) Different conformation of CNTs, their chiral angles, and indices [68].....	36
Figure 3.10 Section of an oxidized CNT reflecting terminal and wall oxidation [71]	37
Figure 3.11 1D wired mode of water molecules inside (8, 2) CNT [68].....	39
Figure 3.12 Water molecules structure inside CNTs (a) Spiral-like layered mode, (b) bulky mode [68]	40
Figure 3.13 Schematic diagram showing the main components of SEM [80]	41
Figure 3.14 The dimension of a MWCNT.....	42
Figure 3.15 Different stages of gas physisorption on sample surface with pressure increase [85]	43
Figure 3.16 Different types of isotherm linear plots [84]	44
Figure 3.17 BET plot to evaluate V_m [91].....	46
Figure 3.18 t-plot comparison between porous and nonporous surface [92].....	47
Figure 4.1 Elcometer 4040 Automatic Film Applicator	52
Figure 4.2 Micrometrics ASAP 2020 instrument [94].....	53
Figure 4.3 Sterlitech HP4750 Stirred Cell	54
Figure 4.4 Different preparation conditions.....	55
Figure 5.1 SEM of an asymmetric membrane	62

Figure 5.2 SEM of 17 wt% CA membranes, PI carried out at room temperature: (a) ICT = 500 μm , final thickness = $\sim 55 \mu\text{m}$, (b) ICT = 600 μm , final thickness = $\sim 75 \mu\text{m}$, (c) ICT = 800 μm , final thickness = $\sim 122 \mu\text{m}$ 63

Figure 5.3 SEM of 15 wt% CA membranes, PI carried out at room temperature: (a) ICT = 600 μm , final thickness = $\sim 79 \mu\text{m}$, (b) ICT = 700 μm , final thickness = $\sim 114 \mu\text{m}$, (c) ICT = 800 μm , final thickness = $\sim 122 \mu\text{m}$ 64

Figure 5.4 SEM of 17 wt% CA + 10 wt% H₂O membranes, PI at room temperature: (a) ICT = 700 μm , final thickness = $\sim 137 \mu\text{m}$, (b) ICT = 800 μm , final thickness = $\sim 226 \mu\text{m}$ 65

Figure 5.5 SEM of 15 wt% CA + 5 wt% H₂O membranes, PI at room temperature: (a) ICT = 300 μm , final thickness = $\sim 30 \mu\text{m}$, (b) ICT = 400 μm , final thickness = $\sim 44 \mu\text{m}$, (c) ICT = 500 μm , final thickness = $\sim 55.4 \mu\text{m}$, (d) ICT = 600 μm , final thickness = $\sim 110 \mu\text{m}$ 65

Figure 5.6 A plot showing the non-linear change in final thickness of 17 wt% CA membranes with the increase in ICT. PI was done at room temperature 67

Figure 5.7 SEM of 17% CA content, ICT = 1000 μm : (a) FT = $\sim 180 \mu\text{m}$, PI at room temperature, (b) Voids necks at high magnification for PI at room temperature (c) FT = $\sim 172 \mu\text{m}$, PI at 40°C, (d) Voids necks at high magnification for PI at 40°C .68

Figure 5.8 SEM of 14% CA content, ICT = 1000 μm : (a) FT = $\sim 138 \mu\text{m}$, PI at room temperature, (b) Voids necks at a high magnification, PI at room temperature, (c) FT = $\sim 138 \mu\text{m}$, PI at 40°C , (d) Voids necks at a high magnification, PI at 40°C ..69

Figure 5.9 SEM of three 13 wt% CA membranes prepared with ICT = 1200 μm : (a) final thickness = $\sim 173 \mu\text{m}$, (b) final thickness = $\sim 186 \mu\text{m}$, (c) final thickness = $\sim 216 \mu\text{m}$ 71

Figure 5.10 SEM of 13 wt% CA membranes, ICT = 1000 μm : (a) final thickness= $\sim 155 \mu\text{m}$, (b) final thickness= $\sim 185 \mu\text{m}$ 72

Figure 5.11 SEM of membranes prepared with PI at room temperature, ICT = 800 μm , final thickness of $\sim 122 \mu\text{m}$: (a) 17 wt% CA, (b) 15 wt% CA 72

Figure 5.12 SEM of 17 wt% CA membranes: (a) complete PI for 7.5 min, final thickness = $\sim 180 \mu\text{m}$, (b) PI for 5.5 min, followed by solvent evaporation for 3.5 min, final thickness = $\sim 138 \mu\text{m}$, (c) PI for 2.5 min followed by solvent evaporation for 3.5 min, final thickness = $\sim 135 \mu\text{m}$ 74

Figure 5.13 SEM of 17 wt% CA membranes, PI at room temperature for 7.5 minutes: (a) ISE = 0 sec, final thickness = $\sim 180 \mu\text{m}$, (b) ISE = 60 sec, final thickness = $\sim 77 \mu\text{m}$... 75

Figure 5.14 SEM of 13 wt% CA membranes, ICT = 1000 μm , and PI at room temperature: (a) and (b) are two different locations on the same sample with ISE = 30 sec, final thickness range = 217-161 μm , (c) uniform sample prepared with ISE = 60 sec., final thickness = 123.5 μm	77
Figure 5.15 SEM of 17 wt% CA, PI at room temperature, ICT = 700 μm : (a) 0 wt% H_2O , final thickness = ~ 80 μm , (b) 10 wt% H_2O , final thickness = ~ 137 μm , (c) 15 wt% H_2O , final thickness = ~ 153 μm , (d) 20 wt% H_2O , final thickness = ~ 246 μm	78
Figure 5.16 SEM of 15 wt% CA, PI at room temperature, ICT = 300 μm : (a) 5 wt% H_2O , final thickness = ~ 30 μm , (b) 20 wt% H_2O , final thickness = ~ 80 μm	79
Figure 5.17 SEM of 14 wt% CA, PI at room temperature, ICT = 1000 μm : (a) 0 wt% H_2O , final thickness = ~ 138 μm , (b) 5 wt% H_2O , final thickness = ~ 199 μm , (c) 10 wt% H_2O , final thickness = ~ 264 μm (non-uniform).....	80
Figure 5.18 SEM displaying compaction difference in the middle sections of 13 wt% CA membranes, PI at room temperature: (a) 0 wt% pNTs at 5KX, (b) 0 wt% pNTs at 10KX, (c) 0.5 wt% pNTs at 5KX, (d) 0.5 wt% pNTs at 10KX	82
Figure 5.19 SEM displaying compaction difference in the middle sections of 17 wt% CA membranes, PI at room temperature: (a) 0 wt% pNTs at 5KX, (b) 0.5 wt% pNTs at 5KX	83
Figure 5.20 SEM of agglomerates of pNTs in 17 wt% CA membranes at 25KX in the middle section of the membranes: (a) 0.5 wt% pNTs at 25KX, (b) 1 wt% pNTs at 25KX	83
Figure 5.21 SEM of the pores structures in the middle section of 17 wt% CA membranes at 25KX: (a) 0 wt% pNTs membrane, (b) 0.5 wt% pNTs membrane, (c) 1 wt% pNTs membrane	84
Figure 5.22 SEM image of both pNTs and fNTs: (a) an agglomerate of pNTs at 700X, (b) a bundle of pNTs at 100 KX, (c) agglomerates of fNTs at a small magnification (700X), (d) arrays of fNTs at 100 KX	85
Figure 5.23 FTIR spectrum of non-functionalized MWCNTs	86
Figure 5.24 FTIR spectrum of functionalized MWCNTs.....	86
Figure 5.25 Beakers filled with 0.01 g CNTs, sonication time for 1 minute in 20 ml deionized water, (a) fNTs fully dispersed giving opaque black solution, (b) pNTs poorly dispersed forming agglomerates throughout the solution and on the bottom of the beaker	87
Figure 5.26 MWCNTs networks in 0.0005/15/20 wt% fNT/CA/ H_2O nanocomposite at different SEM magnifications, (a) at 25KX, (b) at 50KX.....	88

Figure 5.27 MWCNTs networks in 0.005/15/20 wt% fNT/CA/H ₂ O nanocomposite at different SEM magnifications, (a) at 50KX, (b) at different location at 50KX, (c) at 100KX, (d) at different location at 100KX	88
Figure 5.28 MWCNTs networks in 0.01/15/20 wt% fNT/CA/H ₂ O nanocomposite at different SEM magnifications, (a) at 25 KX, (b) at 50KX, (c) at 100KX, (d) at 300KX	89
Figure 5.29 SEM of morphology at same final thickness (100±10 μm): (a) 0/15/20 wt% fNT/CA/H ₂ O, (b) 0.0005/15/20 wt% fNT/CA/H ₂ O, (c) 0.005/15/20 wt% fNT/CA/H ₂ O, (d) 0.01/15/20 wt% fNT/CA/H ₂ O	90
Figure 5.30 Plot of differential pore volumes	92
Figure 5.31 Plot of differential pore volumes for micro and mesopores	93
Figure 5.32 Plot of differential pore volumes for macropores	93
Figure 5.33 Plot of differential pore areas	94
Figure 5.34 Plot of differential pore areas for micro and mesopores	94
Figure 5.35 Plot of differential pore areas for macropores	95
Figure 5.36 Adsorption isotherm of 0/15/20 wt% fNT/CA/H ₂ O at ICT = 350 μm and FT = 100±10 μm	97
Figure 5.37 Adsorption isotherm of 0/15/20 wt% fNT/CA/H ₂ O at ICT = 400 μm and FT = 120±10 μm	97
Figure 5.38 Adsorption isotherm of 0.0005/15/20 wt% fNT/CA/H ₂ O at ICT = 400 μm and FT = 100±10 μm	98
Figure 5.39 Adsorption isotherm of 0.005/15/20 wt% fNT/CA/H ₂ O at ICT = 400 μm and FT = 100±10 μm	98
Figure 5.40 Adsorption isotherm of 0.01/15/20 wt% fNT/CA/H ₂ O at ICT = 400 μm and FT = 100±10 μm	99
Figure 5.41 t- plot of 0/15/20 wt% fNT/CA/H ₂ O at ICT = 350 μm and FT = 100±10 μm	99
Figure 5.42 t- plot of 0/15/20 wt% fNT/CA/H ₂ O at ICT = 400 μm and FT = 120±10 μm	100
Figure 5.43 t- plot of 0.0005/15/20 wt% fNT/CA/H ₂ O at ICT = 400 μm and FT = 100±10 μm	100
Figure 5.44 t- plot of 0.005/15/20 wt% fNT/CA/H ₂ O at ICT = 400 μm and FT = 100±10 μm	101

Figure 5.45 t- plot of 0.01/15/20 wt% fNT/CA/H ₂ O at ICT = 400 μm and FT = 100±10 μm	101
Figure 5.46 Plot showing the effect of fNTs on CA membrane permeation	103
Figure 5.47 Plot showing the effect of fNTs on CA membrane salt retention rates.....	104
Figure 5.48 Representation of the effect of functionalized fNTs addition on the membrane overall performance at same FT.....	104
Figure 5.49 Plot showing the effect of different wt% of fNTs on CA membranes surface area	105
Figure 5.50 Representation of the effect of surface area on the membranes permeation rates at same FT.....	106
Figure 5.51 Representation of the effect of surface area on the membranes salt retentions at same FT.....	106

List of Tables

Table 2.1 Preparation conditions vs. membrane performance of the top 10 membranes. Measurements done at 40 bars, Evaporation time (Ev time), Annealing time (An time), Annealing temperature (T), Permeation rate (P in L/m ² h.bar), Retention (R in %) [25]	13
Table 2.2 PWF rates at different CA/silica contents [32].....	16
Table 2.3 Permeation rates of metal ions using CA/PSF/PVP blend membranes [31]	18
Table 2.4 PWF rates of CA/PES blend membranes with different PEG 600 additive concentrations [34].....	20
Table 2.5 Pore size and density and pure water flux of the CA/ZrO ₂ UF membranes [37] ...	22
Table 2.6 Permeation and rejection rates as a function of CNTs concentration for 10 wt% PA at 39 bars and 25°C [41].....	26
Table 5.1 Macrovoids numbers and dimensions relative to CA content, non-solvent content, and membrane thickness	66
Table 5.2 Macrovoids numbers and dimensions relative to CA content and PI temperature..	70
Table 5.3 Macrovoids numbers and dimensions relative to CA content	73
Table 5.4 Macrovoids numbers and dimensions relative to solvent evaporation	75
Table 5.5 Macrovoids numbers and dimensions relative to non-solvent addition	81
Table 5.6 Macrovoids numbers and dimensions relative to fNTs addition	90
Table 5.7 Summary of surface area measurements, and micropores volumes	102
Table 5.8 Effect of fNTs wt% on permeation, salt retention, and surface area, rate measurements are for 15/20 wt% CA/H ₂ O membranes using 1000 ppm NaCl solution at 24 bars and room temperature	107
Table 5.9 Calculated change in permeation rates and salt retention rates at same membrane final thickness.....	108
Table 5.10 Calculated change in permeation rates and salt retention rates at same membrane initial casting thickness	108

List of Abbreviations

Abbreviation	Meaning
BSA	Bovine Serum Albumin
CA	Cellulose Acetate
CBT	Coagulation Bath Temperature
CNTs	Carbon Nanotubes
DMAc	N,N-Dimethylacetamide
DMF	N,N-Dimethylformamide
ED	Electrodialysis
fNTs	Functionalized Carbon Nanotubes
FT	Final Thickness
FTIR	Fourier Transform Infrared Spectroscopy
GA	Glutaraldehyde
GBA	γ -Butyrolactone
ICIC	Isocyanate and Isophthaloyl Chloride
ICT	Initial Casting Thickness
IPA	Isopropanol
ISE	Initial Solvent Evaporation
MD	Molecular Dynamics
MED	Multiple-Effect Distillation
MF	Microfiltration
MSF	Multi-Stage Flash
MWCNTs	Multi-Walled Carbon Nanotubes
NF	Nanofiltration
NMP	1-Methyl-2-Pyrrolidone

Abbreviation	Meaning
NMR	Nuclear Magnetic Resonance
NOCC	N,O-Carboxymethyl Chitosan
PA	Aromatic Polyamide
PEG	Polyethylene Glycol
PEO	Polyethylene Oxide
PES	Polyethersulfone
PI	Phase Inversion
pNTs	Pristine (Non-Functionalized) Carbon Nanotubes
PSF	Polysulfone
PVP	Polyvinylpyrrolidone
PWF	Pure Water Flux
RO	Reverse Osmosis
SEM	Scanning Electron Microscope
SLS	Sodium Lauryl Sulphate
SWCNTs	Single-Walled Carbon Nanotubes
TFC	Thin Film Composite
UF	Ultrafiltration
v/v	Volume by Volume
VCD	Vapor Compression Distillation
wt%	Weight Percent

1 Introduction

1.1 History

Water is the basic ingredient in life, and man knew this since dawn age. He looked for sources of drinkable water and settled right next to them. As history tells, the search of good tasting water was recorded on the tombs of the Pharaohs [1]. In the ancient Greek books, sailors used the classical distillation method of boiling seawater and using wool condensation to get fresh one [2]. But it was not until the early 17th century that water desalination laboratory experiments were suggested in the hope of removing salts from saline water (sea and ocean sources) and converting them into drinkable water using salt filters. Then in 1685, the 1st recorded experiment was carried out in which the Italian physician Lucas Portius used multiple sand filters with different grain sizes distributed along the filter system in order to produce the best tasting water [1]. As time passed by, man depended on either sand filters or distillation methods to purify water. The alternative was carrying large amounts of freshly stored water in tanks during trips. It wasn't until WWII that the need of 'light' portable desalination filters was the focus of governments to aid military troops in different arid regions. Later in the mid 20th century, different countries established research and development programs funded by their governments to improve water desalination technologies to produce drinkable and irrigation water at the lowest possible costs [3-4]. Since then, thousands of research investigations focusing on water treatment were carried out worldwide and large numbers of desalination plants were established to reach 14,451 plants producing 59.9 million cubic meters per day in 2009 with an annual growth rate of ~12% each year according to Lisa Henthorne, the president of the International Desalination Association [5].

However, this is still not enough especially that natural fresh water is nothing permanent and is possibly depleting due to the enormous annual population increase, extensive water consumption, and water sources pollution [6]. Locally, Egypt is expected to face a grave water scarcity problem in less than 12 years from today according to the Water Research Center of Egypt where 60% of the farmers won't be able to retrieve water for irrigation due to the shortage of fresh water supplies [7]. In 2010, the UN announced that Egypt is below the water poverty line with only 1000 m³ of water per person per year, while the world average is 7000 m³ of water per person per year [8], even though the country has ~2,500 km worth of coastline [9], as well as 35,000 km of brackish water canals [10]. Accordingly, with sufficient number of desalination plants established, the government could meet the large water demands especially for coastal cities, and irrigation areas.

1.2 Desalination Technologies

Desalination technologies are concerned with finding alternative sources for drinkable and irrigation water, as well as water used for industrial purposes, other than the ground and the underground fresh water. Sources usually include seawater, brackish water, and wastewater. Figure 1.1 shows the shares of different saline water sources used in desalination industries [11]. Typical seawater has salt content ranging between 30,000 to 50,000 ppm, but on average it contains 35,000 ppm. Brackish water has 500 to 30,000 ppm salinity, while fresh water contains less than 500 ppm salinity, yet, saline content in drinkable water

shouldn't exceed 250 ppm [12]. As for wastewater, its desalination and purification for industrial purposes and even to be used as a drinkable water source is a relatively new concept. Yet indeed, it can't be denied that it is an excellent recycling technology since wastewater is usually discharged without further use [13].

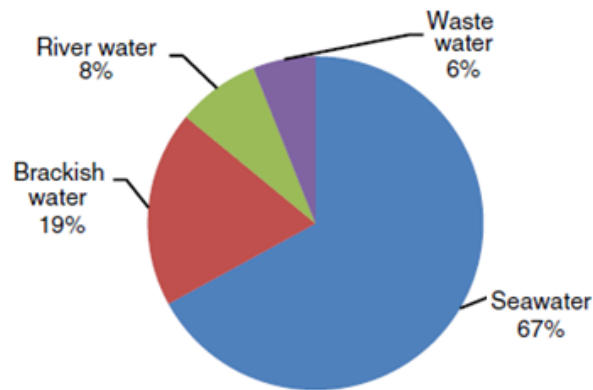


Figure 1.1 Desalination saline sources % worldwide [11]

To date, among the many types of desalination processes, only few were converted into large industries of fresh water production because commercializing a desalination process is limited by the amount of energy required for production, the price of cubic meter of freshwater produced by different processes, and environmental impact especially for brine discharge [11, 13]. Figure 1.2 shows the different shares of each process globally [11], where reverse osmosis (RO), multi-stage flash (MSF), and multiple-effect distillation (MED) take the lead. Other desalination processes include electrodialysis (ED), vapor compression distillation (VCD), and micro, ultra, and nanofiltration (MF, UF, NF respectively). In the next sections, a briefing about all mentioned processes is given.

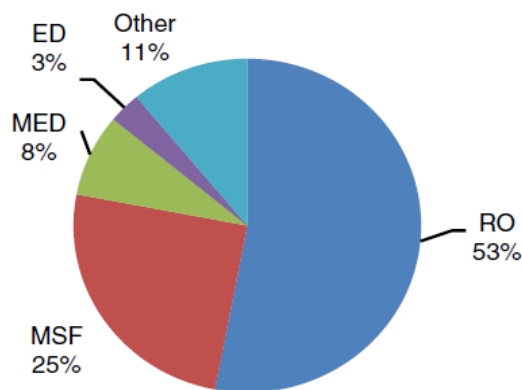


Figure 1.2 Desalination processes % worldwide [11]

1.2.1 Multi-Stage Flash (MSF)

MSF, a thermal desalination process, was first introduced in the early 1960's, and then it conquered the desalination market in 1980's and 1990's because it proved to be a simple

reliable process [11, 13-14]. Today, MSF represents more than 93% of all the thermal desalination processes' share [15] and 25% of the global desalination processes' share [11].

MSF is a simple evaporation and condensation process, where the saline feedwater is first preheated by passing over a series of closed pipes. It is there heated in a brine heater. Next, the hot saline enters a series of flashing chambers (called vessels or stages) of progressively low pressures. The lower pressure of each stage compared to the one before it results in an immediate boiling (flashing) of the heated saline and evaporation of the fresh water. The steam is collected and directed inside the closed pipes in which heat exchange takes place between the vapor and the feedwater (that becomes preheated in the first step), while the steam condensates. The distillate is gathered by collector trays, and directed as an output of fresh water. The remaining feedwater (now becoming brine) is partially disposed, and partially recirculated into the stages to recover more fresh water. Finally, the remaining brine now with 15-20% more salt concentration than the initial saline feedwater is cooled and then discharged.

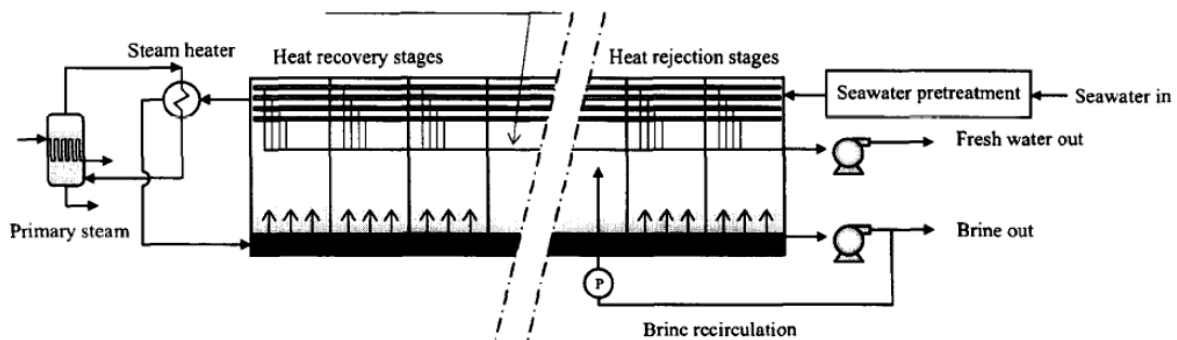


Figure 1.3 Diagram of Multi Stage Flash Process [13]

It is worth mentioning that in each stage, only small percentages of saline feedwater vaporize, due to the limited pressure drop from one stage to the next. That is why in order to retrieve large percentage of fresh water, up to 40 stages would be used, with an average of 18 to 25 stages in regular MSF plants [11].

The main advantages of MSF are simplicity, reliability, irrelevance of the saline feedwater concentrations or existence of suspended particle, and very low salt concentration in the retrieved fresh water. However the main disadvantage of this process is its electrical and thermal energy requirements that make it an expensive technology [11, 13-14].

1.2.2 Multiple-Effect Distillation (MED)

MED, also a thermal desalination process was first introduced in the mid 19th century to be classified as the oldest industrial desalination technique. Yet, after the introduction of MSF and RO, the demand for MED significantly decreased over the years and represents only 8% of today's world desalination industrial share [11, 14].

The process, similarly to MSF, depends on evaporation and condensation at progressively lower pressures, and temperatures within 8 to 16 consecutive effects. Yet, the structure of

MED setup is different. The saline feedwater is first preheated, and then introduced into the first effect where it passes over a series of tubes filled with hot steam, and through heat exchange, the feedwater is heated until boiling, while the steam inside the tubes condensates. The resultant steam is introduced into the second effect condensation tubes, while the remaining feedwater is introduced outside the tubes inside the effect at lower pressure and temperature. Then, the process of evaporation and condensation continues inside different successive effects. The final steam is directed into the primary condenser where preheating of the feedwater takes place. As for the brine formed, it is cooled and discharged [11, 13-14].

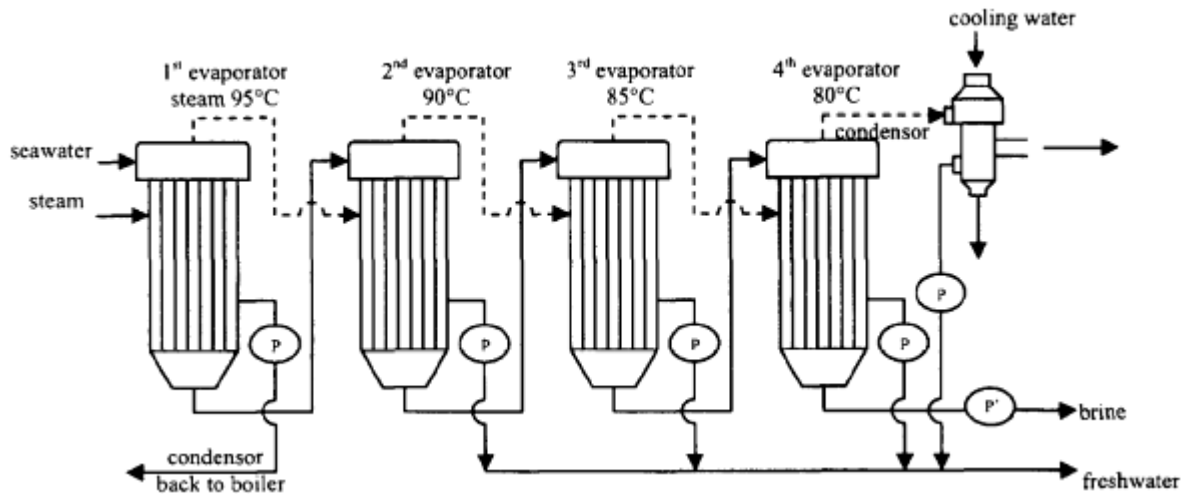


Figure 1.4 Diagram of Multiple Effect Distillation Process [13]

The advantage of MED over MSF is that it requires lower thermal and electrical energy, making it more environmentally friendly since the lower energy required means lower fuel used and lower exhaust. However, due to its more complex setup, MED faces corrosion and scaling inside the condensation tubes that are difficult to remove, which is a major disadvantage.

1.2.3 Reverse Osmosis (RO)

RO, a membrane desalination process, is the global leading technology in fresh water production by desalting with a 53% share, and its use is rapidly increasing due to the large ongoing research and development in the membrane technology [11, 16]. This process depends on reversing the osmotic flow through a semipermeable membrane by applying pressure as indicated in Figure 1.5.

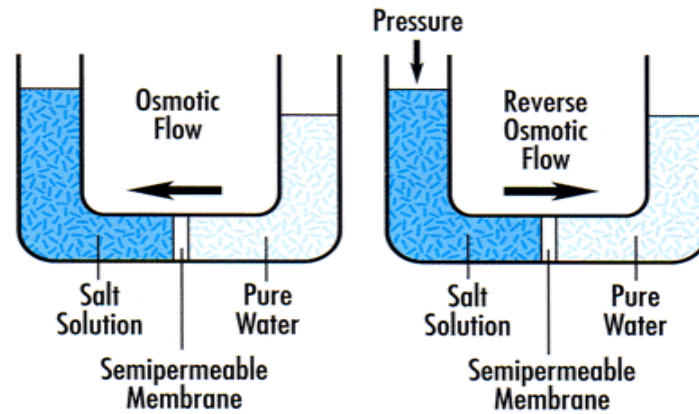


Figure 1.5 Osmosis and Reverse Osmosis flow [17]

The nominal pore size of RO membranes is 1 to 10 Å, which is capable of filtering out colloidal particles, bacteria, viruses, and ions including monovalent ones, while allowing only pure water to pass through [17]. In practice, the saline water is introduced into a pressurized sealed vessel, and pumped against the semipermeable membrane, which is capable of filtering up to 70% of the salts with a target final salt concentration of 250 ppm or less from a single run [11, 14]. The required pressure depends on the degree of water salinity. For example, seawater desalination requires 56 to 105 bars, while brackish water desalination requires 14 to 42 bars [18]. The pressure values, (thus the amount of energy consumed), could be reduced by developing membranes with nanopores, large enough to allow the passage of large volumes of water, but small enough to block the passage of monovalent ions [16]. A good example of low pressure developed membranes was created by Loeb and Sourirajan in 1963 using cellulose acetate, which is an asymmetric porous membrane with high permeation rates and good salt rejection. Another material used in RO membranes is polysulfone mixed with aromatic polyamides to form the so called thin film composite membrane [14].

The major disadvantage of RO process is its membrane fouling which is a key problem, requiring good pretreatment processes to minimize its effects. Fouling happens due to the precipitation of a foulant on, in, and/or near the membrane surface, blocking the nanopores, reducing the water flux, possibly increasing salt passage, significantly increasing the operational pressure, and consequently the energy involved in the process [19]. There are 4 types of fouling [14, 19]:

1. Inorganic fouling: (also called scaling) it is the precipitation of dissolved salts from iron, aluminum, calcium, and sulfates under the concentration polarization effect. That is the accumulation of salts in high concentrations at the membrane boundary compared to their concentration in the remaining feedwater.
2. Colloidal fouling: it is the precipitation of colloidal solids of 5µm or little less, such as clays or silica, resulting in the formation of a secondary layer, resistant to water flow.
3. Organic fouling: it is the development of a thin film of organic compounds like proteins, polysaccharides, polyphenolic molecules, or hydrocarbons on the membrane.

4. **Biofouling:** it is the development of a biofilm on the membrane surface from bacterial colonies, fungi, or algae that are able to reduce water flux, increase transmembrane pressure, and/or degrade the membrane either by enzymatic biochemical degradation or by creating a local pH at the membrane surface, resulting in membrane hydrolysis.

Fouling pretreatment plans are usually prepared according to the initial constituents of the feedwater, i.e. they are directly related to the water source [19]. For example, feedwater from sources located near sea ports need to consider organic fouling from types of organic compounds that don't normally exist with such high concentrations in seawater (ships' fuel wastes).

1.2.4 Other Processes

Electrodialysis (ED): it is an electrical desalination process in which salt ions from saline water are transported toward two membranes (a cation and an anion) by applying a potential difference between them, thus the saline water becomes fresh. It is a very useful technique for desalting brackish low saline concentration water [11, 13].

Vapor compression distillation (VCD): it is a mechanical desalination process that resembles MSF and MED in using steam to convert the feedwater into vapors, yet it uses mechanical compressors to condensate the distillate into fresh water instead of heat exchange. This technique is utilized in small scale desalination industries [13-14].

Microfiltration, Ultrafiltration, and Nanofiltration (MF, UF, NF): those are semipermeable membranes, used mainly as pretreatment steps in desalination plants. Figure 1.3 shows the pore size distribution of each membrane type [11, 14, 17].

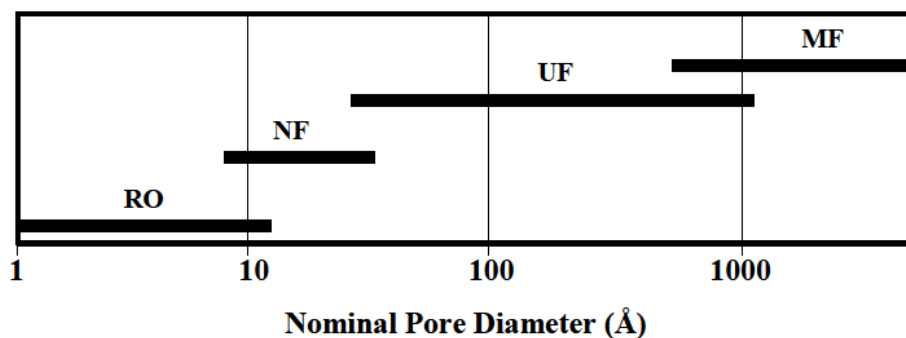


Figure 1.6 Pore size distribution of each membrane type [14]

Microfiltration (MF) membranes have the largest pore diameter, thus they could be used in removal of large suspended particles, some microorganisms like large bacteria and algae, and reduction of turbidity. MF membranes materials include poly (vinylidene fluoride), polysulfone, poly (acrylonitrile), poly (acrylonitrile)- poly (vinyl chloride) copolymers, cellulose acetate-cellulose nitrate blends, nylons, and poly (tetrafluoroethylene) [14, 17].

Ultrafiltration (UF) membranes come second in pore size diameters where it can reject large colloidal particles, bacteria, some viruses, organic compounds of high molecular weight, and

macromolecules such as proteins. UF membranes are made of some of the same materials of MF membranes such as poly (vinylidene fluoride), polysulfone, and poly (acrylonitrile), yet under different preparation conditions to have smaller pores. UF membranes are also manufactured from poly (ether sulfone), which is the most common material used [14, 17].

Nanofiltration (NF) membranes come third in pore size diameters between UF and RO membranes. They are used in the removal of everything that MF and UF membranes can remove, in addition to organic compounds, multi-valent ions, and viral particles. NF membranes are manufactured from materials similar to RO and UF membranes, using different preparation conditions. These include cellulose acetate blends, polyamide composites, or sulfonated polysulfone [14, 17].

2 Literature Background

2.1 Introduction

For membrane research, different investigations targeted different directions for membrane development, however, the final aim is the same: developing a membrane that at the lowest possible pressures gives high water permeation rates and high salt retention, while being resistant to different fouling factors with long durability. Such a difficult to reach combination of requirements opened lots of areas of variation in membranes' preparation conditions. Typically, work focused on material types, concentrations, solvent and non-solvent types, presence of additives, preparation temperature, and/or a blend of different materials to achieve the requirements.

The first ever reported RO membrane with effective salt retention (98%) was manufactured in 1959 by Reid and Breton. It was a hand cast symmetrical thin film of cellulose acetate (CA) with a water permeation rate less than $0.01 \text{ L/m}^2\text{h}$. In less than 5 years, Loeb and Sourirajan developed the famous CA asymmetric membrane with a little higher salt retention (99%) than Reid's, and much higher water permeation rate of $14.6 \text{ L/m}^2\text{h}$ to become the first high flux asymmetric RO membrane [20]. Then, a new introduction of materials took place in 1970's when Cadotte et al. prepared a multiple layered membrane using *in situ* polymerization of branched polyethyleneimine and 2,4-diisocyanate to form a polyamide deposited on the surface of a porous polysulfone membrane. They called it thin film composite (TFC), and when tested, it gave water flux of $3.5 \text{ L/m}^2\text{h}$ and salt retention of 94.5 % [19]. Since then, RO membranes were either manufactured from CA or TFC while varying preparation conditions and additives to get better performance.

The literature background will address CA membranes in filtration applications, as well as the usage of carbon nanotubes in water desalination since these are the materials used in the current study.

2.2 Effect of Different Additives

Additives refer to the addition of an extra material (a second solvent, a non-solvent, a nanofiller, or a surface modifier) during the membrane preparation with the aim of enhancing permeation rates and salt retention. However, permeation rates and retention are inversely proportional to one another since increasing pore sizes across the membrane to enhance the flux, usually leads to allowing more solutes to pass through. Thus, experiments target the highest possible salt rejection at acceptable rates. Achieving this is controlled by the concentration and type of the additive, which directly affect the macrovoids sizes and location across the membrane. This also affects the porosity of the top dense layer, changing the membrane type from ultra to nano or to RO filter membranes.

2.2.1 Effect of Solvents and Non-Solvents

Experimentally, Li et al. [21], who used different concentrations of γ -butyrolactone (GBA) (secondary solvent) added to 11 wt% CA dissolved in 1-methyl-2-pyrrolidone (NMP) to convert an UF CA membrane to a NF one, and to check how this affects its pure water flux

(PWF) and salt retention. The membranes were prepared by phase inversion (PI) process at room temperature, and water as non-solvent in the coagulation bath. When GBA concentration was 50 wt%, PWF was as high as $\sim 150 \text{ L/m}^2\text{h}$ at 10 bars, yet, with 0% salt retention. Once GBA concentration increased to 80%, salt retention increased (though by only 10%), which means that the membrane became a NF, yet a poor one. At the same time, PWF decreased dramatically to only $0.2 \text{ L/m}^2\text{h}$. The paper concluded that by using good solvent mixtures, membrane porosity could be modified to serve a designated purpose.

Ye et al. [22] went further in trying to mix different solvents, where they compared membranes formed from 20 wt% CA at 20°C and dissolved in one solvent with CA membranes dissolved in a mixture of two solvents. Both sets of membranes were prepared by PI at room temperature and water as non-solvent in the coagulation bath. Then they compared the two sets to CA membranes formed from a mixture of two solvents and a non-solvent, also prepared with PI at room temperature, and water as non-solvent in the coagulation bath. Membranes formed from CA dissolved in only *N,N*-dimethylformamide (DMF) gave a permeation rate of $7.5 \text{ L/m}^2\text{h}$. On adding 40 wt% acetone (secondary solvent), the rate decreased to $1.7 \text{ L/m}^2\text{h}$. Further addition of isopropanol (IPA) non-solvent to give 30/20 wt% of acetone/IPA respectively increased PWF to $15.8 \text{ L/m}^2\text{h}$, which is almost double the initial rate. All permeation tests were carried out at the same temperature and pressure. The results indicate that the presence of a non-solvent could enhance water permeation rates, more than simply mixing two solvents together. It is worth mentioning though, that the paper focused on how these membranes could be used in blood purification for the removal of macromolecules such as Methyl orange, Cytochrome C, Albumin, and γ -Globulin. This means that the manufactured membranes can't be used in desalination since salt ions' sizes are much smaller than the mentioned molecules.

Haddad et al. [23] succeeded in creating nanofilter membranes from 20 and 22 wt% CA using a mixture of acetone solvent and formamide non-solvent with a ratio of 2:1. This was made possible via manipulation of the preparation conditions, where in the PI step, the gelation medium was distilled water at a temperature of 4°C , and the casted solution remained in the medium for 1 hour. Then the membranes were immersed individually in annealing water baths at temperature ranges from 60 to 80°C for 10 minutes to study the effect of annealing temperature on membrane performance. The final membranes' thicknesses were $70\text{-}90 \mu\text{m}$. PWF measurements were done at different pressure ranges ($4\text{-}16$ bars), and the study showed that PWF is directly proportional to pressure increase which made perfect sense, and inversely proportional to temperature increase, which was expected because the idea behind annealing is reduction of pore sizes by creating denser membranes under the effect of temperature. This was further supported by scanning electron microscope (SEM) images. Salt rejection and permeation rates were tested using a 2000 ppm NaCl solution at transmembrane pressure of 16 bars. At the same salt rejection rates, membranes with less CA content (20 wt%) showed higher flux rates. On comparing flux rates with rejection rates, the results showed that the higher the flux rates the better the rejection rates, which is a trend supported in the literature [24]. Finally, on comparing rejection rates to annealing temperature, as expected, higher temperature of 75 and 80°C resulted in higher

rejection rates, the highest of which was ~87% with permeation rate of ~10 L/m²h for the 20 wt% CA, and the best conditions were found to be for membranes with 20 wt% CA, annealed at 75°C to have permeation rate of ~75 L/m²h and rejection rate of ~85%. Figure 2.1 displays the results found.

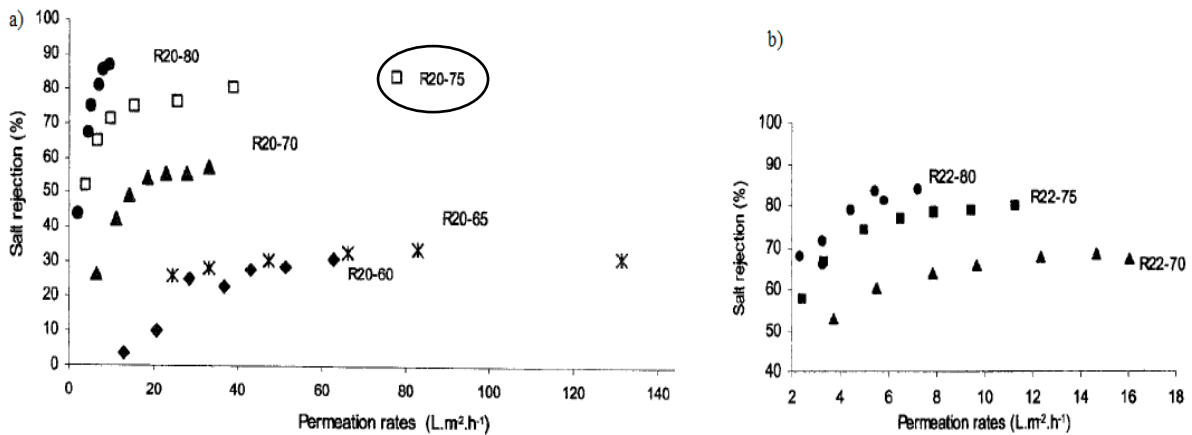


Figure 2.1 Flux rates vs. Rejection rates of 2000 ppm NaCl solution for temperature ranges of 60,65, 70, 75, and 80°C, (a) data of 20 wt% cellulose acetate membranes, (b) data of 22 wt% cellulose acetate membranes [23]

Odena et al. [25] also managed to create nanofilter CA membranes by studying the effect of a very wide variation of preparation conditions. CA wt% ranged from 12 to 21 wt%, a mixture of acetone and dioxane solvents were used, and further mixed with methanol non-solvent. PI coagulation medium was distilled water kept at constant temperature of 4°C, while the annealing temperature ranged from 65 to 85°C. The initial solvent evaporation (ISE) before gelation was tried for 30, 60, 90, or 120 seconds, and the membranes' performances were tested with 5000 ppm NaCl solution at operational pressure of 40 bars, at room temperature. Of all these conditions, the highest salt rejection rates were for two membranes, the first with 19 wt% CA, 7.5 wt% methanol prepared with ISE of 60 seconds, and annealing temperature of 75°C for 2 minutes, and gave rejection rate of 82.55% and permeation rate of 48 L/m²h at 40 bars. The second was prepared with 21 wt% CA, 12 wt% methanol, with ISE of 60 seconds, and annealing temperature of 75°C for 6 minutes, and it gave a salt rejection rate of 79.9% and permeation rate of only 2.4 L/m²h at 40 bars. This significant drop in permeation rate from membrane 1 to 2 could be explained by the increase in both CA wt% and annealing time, each of which contribute to the formation of denser membranes. On the other hand, the increase in non-solvent content was expected to increase the macrovoids and thus the permeation rate, but it seems that the effect of *densing* membrane 2 over-ruled the effect of increasing macrovoids numbers or size via the non-solvent. As for the rest of the membranes prepared, their performance was tested using ibuprofen, a small micro-pollutant used in drugs manufacturing that is commonly found in drinking water. The best ten membranes that gave high permeation and retention rates are displayed in Table 2.1.

Table 2.1 Preparation conditions vs. membrane performance of the top 10 membranes. Measurements done at 40 bars, Evaporation time (Ev time), Annealing time (An time), Annealing temperature (T), Permeation rate (P in L/m²h.bar), Retention (R in %) [25]

Membrane	CA (wt%)	Methanol (wt%)	Dioxane (wt%)	Acetone (wt%)	Ev time (s)	An time (min)	T (°C)	P	R
M2-12	20	13	47	20	60	14	80	0.49	90.35
M3-39	19	7.5	54	20	120	2	75	1.1	73.4
M3-47	19	7.5	54	20	60	2	75	1.2	82.5
M4-20	19	7.5	54	20	30	2	75	1.3	77.8
M3-21	18	12	50	20	60	6	80	0.9	79.4
M1-8	13	14	52	20	30	14	85	1.0	87.7
M3-11	13	12	55	20	30	14	80	0.49	89.45
M1-4	13	6.2	60.8	20	60	6	75	0.96	70.57
M4-11	12	23	45	20	30	10	75	0.7	80.00
M4-46	12	17	51	20	60	14	70	0.69	77.95

According to the results, the highest rejection rate (90.35%) is found for the 20 wt% CA membrane, since it had more polymer content than the rest. As for the highest permeation rate (52 L/m²h at 40 bars) is for the 19 wt% CA with the shortest ISE and annealing periods. The data above is a clear example of how manipulation of conditions can give the same results though the polymer contents are different.

2.2.2 Effect of Pore Formers

Lv et al. [26] thought of adding to CA a copolymer that acts as a pore former, and see how this would affect the membrane behavior. A pore former is a term used to describe an additive, solid or liquid, organic or inorganic, that is more polar and less volatile than the solvent. At the same time, a pore former is soluble/miscible in the non-solvent used in PI such that when the main polymer matrix starts gelation, the pore former leachability creates macrovoids that enhances permeation rates [27]. Putting this idea in practice, membranes of 16 wt% of CA mixed with different concentrations of Pluronic F127, dissolved in DMF were tested for PWF and rejection rates of bovine serum albumin (BSA), since they were expected to be ultrafiltration membranes. Operational pressure was 1 bar and temperature was 25±1°C. Prior to the tests, membranes were subjected first to 1.5 bars for 30 minutes to overcome the compaction effect of pressure. At 0 wt% Pluronic F127, the blank CA membrane gave a very low PWF rate of only 3 L/m²h, which increased with the increase of Pluronic F127 content to give a PWF of 93.24 L/m²h at 20 wt%. BSA rejection tests showed that using the additive, the membrane is able to reject higher BSA contents compared to blank membranes. Interpreting membranes morphology using SEM at different Pluronic F127 wt% showed that the more additive used, the more porous the membrane becomes, which justifies the PWF increase by an order of magnitude from the blank to the CA membranes prepared with the additive. Yet, the rejection rates didn't show a linear increase with Pluronic F127 wt% increase, instead, the rate increased to a maximum of 77% at additive content of 8 wt%, then it started decreasing again. A suggesting interpretation to this is that addition of small contents of Pluronic F127 decreased the pore size on the membrane surface (while increasing the size of the macrovoids) until a flipping point at which further addition would only increase the pore sizes. Figure 2.2 shows the membrane performance as a function of Pluronic F127 wt%.

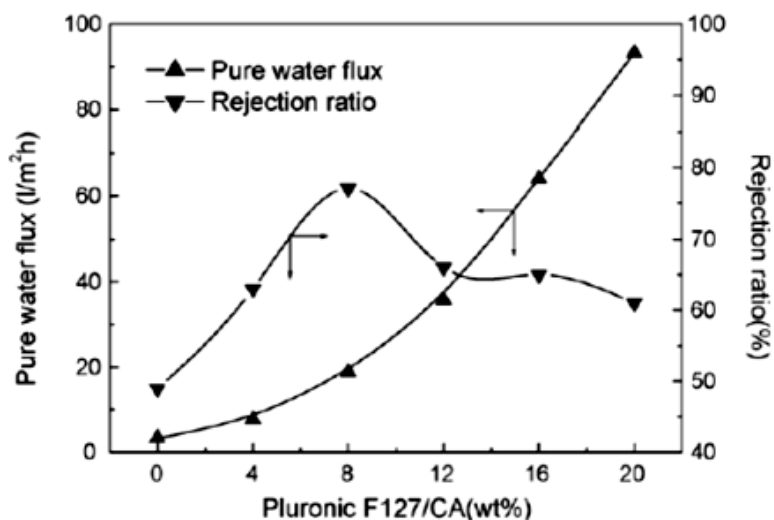


Figure 2.2 Pure water flux and BSA rejection rates vs. Pluronic F127 content [26]

Saljoughi et al. [28] tried using a different pore forming agent, polyethylene glycol 600 (PEG polymer), on CA membranes. Small different concentrations were added to 15.5 wt% CA dissolved in NMP at 23°C and transmembrane pressure of 0.2 bars. Initially, with 0 wt% PEG 600, the PWF rate was 7.75 L/m²h. By adding 5 wt% of PEG 600, the PWF increased more than 11 times the initial rate to give 90 L/m²h. Further increase of PEG 600 (10 wt%) increased the rate again to give 200 L/m²h. This shows that the presence of a pore former could enhance the formation of macrovoids across the membrane, which in turn enhances the PWF rates. It is worth mentioning, though, that when Lv et al. [26] tried using 4 and 8 wt% of PEG 2000 instead of PEG 600 with a 16 wt% CA, the membranes didn't allow permeation of water since it interacted with the CA too strongly to leach out during PI. Thus, the molecular weight of the additive is important. As for rejection rates, Saljoughi et al. didn't mention anything about the molecular weight cut off of the developed membranes. They only suggested that the membranes could be used in ultrafiltration applications.

Idris et al. [29] used a lower molecular weight PEG 400 as a pore former, and added to it distilled water as a swelling agent to have narrow pores to maximize rejection rates. Different contents of PEG 400, water, and CA were dissolved in acetic acid, and permeation experiments for 2000 ppm BSA solution were carried out at 25°C and transmembrane pressure of 2 bars. PWF was not measured though. The highest permeation rate of the 2000 ppm BSA solution was 56.67 L/m²h and was found to be for the membrane with the lowest CA and water contents of 15 and 5 wt% respectively, and 10 wt% PEG. However, on increasing CA and water contents to 20 and 10 wt% respectively, permeation rate dropped more than half its value to be 25.24 L/m²h. On the other hand, this decrease was accompanied by an increase in BSA rejection rate from 90.19 to 96.19%. The team tried one more contents combination of 20/5/5 wt% for CA/PEG/H₂O respectively. This resulted in the lowest permeation rate of 17.54 L/m²h and rejection rate of 42.54% for the 2000 ppm BSA solution. A possible explanation to these values was at lower PEG and water contents, there is more of the acetic acid solvent that reduced the polymer packing density, creating larger pores, but not macrovoids. Thus, rejection rates decreased since the pores are too large to prevent the

protein from passing through, yet, they are too small to allow high flux rates. On increasing PEG and water to 10 wt% each at 20 wt% CA, more macrovoids were created to increase the permeation rate, and at the same time, the packing density of the polymer increased to maximize the protein rejection rate. Finally, decreasing only the swelling agent (water to 5 wt%) and CA (15 wt%) gave the maximum earlier mentioned permeation rate, since the pore forming agent PEG created the necessary macrovoids, and at the same time, less polymer and less swelling agent existed.

Saljoughi et al. [30] studied the effect of using a different pore former polyvinylpyrrolidone (PVP). They used different concentrations added to 15.5 wt% CA dissolved in NMP, and prepared the membranes using PI at 25°C. Permeation tests were carried out at room temperature and transmembrane pressure of 0.35 bars. They found that the addition of 3 wt% PVP increased macrovoids formation, consequently PWF reached 65 L/m²h vs. only 18 L/m²h for CA membrane prepared without PVP at the mentioned temperature and pressure. Further increase in PVP concentration (6 wt%) led to decrease in PWF to give a rate of 39 L/m²h. The team concluded that increasing the second polymer concentration doesn't necessarily mean increasing water flux rates, since there could be a flipping point at which too much of the polymers suppress the macrovoids formation, instead of enhancing it. Yet, the team failed to mention how the addition of PVP affects salt or protein rejection.

Sivakumar et al. [31] also studied the effect of adding different concentrations of PVP to 17.5 wt% CA dissolved in DMF on PWF, macrovoids formation, and heavy metals filtration. Membranes were prepared using PI at 10°C in a coagulation bath filled with water, DMF, and sodium lauryl sulphate (SLS) surfactant, used in reducing the surface tension at the developing membrane non-solvent interface. Tests were carried out at transmembrane pressure of 4.14 bars and room temperature. An increase in PWF from 14.1 to 78.8 L/m²h with the increase of PVP weight content from 0% to 7.5% was observed. Comparing such result with Saljoughi et al. [30] consequently shows that the solvent type and its interaction with PVP is playing a role in enhancing/suppressing macrovoids formation, thus PWF rates, since Sivakumar et al. used higher PVP and CA wt% and still got higher PWF rates.

Arthanareeswaran et al. [32] used an inorganic pore former added to 17.5 wt% CA membranes to test their performance. Tetraethyl orthosilicate (aka silica) nanoparticles with different concentrations (0-40%) were mixed with CA dissolved in DMF, to have a fixed CA/silica concentration of 17.5 wt%. PI was carried out after an ISE for 30 seconds. Gelation medium was a mixture of water (non-solvent), DMF (solvent), and SLS surfactant. PI lasted for 30 minutes to ensure a complete removal of the solvent and the pore former from the membrane, and membranes' final thicknesses were 200±20 µm. Flux rates were measured at operational pressure of 3.45 bars. PWF rate for 0% silica membranes was 15.58 L/m²h that increased to 46.74 L/m²h for the 60/40 % CA/silica content as shown in Table 2.2.

Table 2.2 PWF rates at different CA/silica contents [32]

Polymer (17.5 wt.%)		Solvent (wt.%)	PWF at 345 kPa ($\text{lm}^{-2} \text{h}^{-1}$)
CA	SiO ₂	DMF	
100	0	82.5	15.58
90	10	82.5	35.83
80	20	82.5	42.07
70	30	82.5	45.18
60	40	82.5	46.74

According to tabulated results, the increase in silica content had a direct effect on PWF that increased 3 times from 0% silica to 40% silica content. This was directly reflected in the membrane performance in the proteins' permeation and rejection rates. BSA, Trypsin, Pepsin, and albumen permeation increased with the increase in silica contents. For example, BSA permeation rate increased from ~5.2 to ~19.7 L/m²h. However, all proteins' rejection rates decreased with silica increase. For example, BSA rejection decreased from ~94 to ~81% for the 60/40% CA/silica contents, indicating larger macrovoids formation with silica contents increase.

Chen et al. [33] also used different concentrations of silica nanoparticles (0-30 wt%) added to 16 wt% CA dissolved in DMF to test the membranes' performance. PI gelation medium varied from pure water to acidic medium (pH 1) and basic medium (pH 13) to try to understand the effect of different pHs on the efficiency of the nanoparticles leachability from the polymer matrix, as well as on the membranes' permeability and rejection rates. In both the acidic and basic mediums, SiO₂ nanoparticles were unable to effectively leave the polymer matrix. This was characterized by Fourier transform infrared (FTIR) spectroscopy that gave clear absorption peaks for Si-OH and Si-O-Si bonds, the hydrolyzed and polycondensated forms of the silica nanoparticles, after being catalyzed by HCl or NaOH in both mediums. Further analysis using transmission electron microscopy (TEM) proved the existence of circular shaped beads imbedded into the matrix. Energy dispersive X-ray (EDX) spectroscopy mapping for Si element showed a homogenous distribution of the nanoparticles throughout the membrane. This could be due to the cross-linkage formed between the nanoparticles and the polymeric chains of CA. In pure water medium, the story was different, where silica nanoparticles totally leached out of the CA membranes, and no absorption peaks could be seen. Flux rates were studied for all membranes at operational pressure of 1 bar, after initially leaving the membrane for 30 minutes at 1.5 bars to eliminate compaction effect. For blank (0 wt% silica) CA membranes, PWF was very low (approximately 1.7 L/m²h), which didn't change regardless of the gelation medium type. The addition of silica enhanced PWF significantly, especially in the acidic medium, where 30 wt% silica in pH 1 gave PWF of 436.6 L/m²h, indicating drastic increase in the number and size of pores as shown in Figure 2.3.

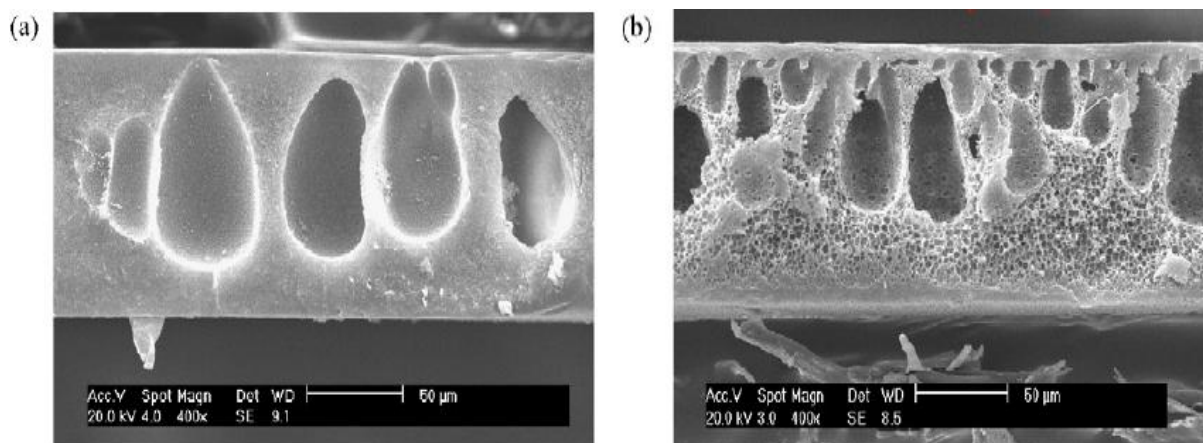


Figure 2.3 (a) SEM of blank cellulose acetate membrane in pure water gelation medium, (b) SEM of cellulose acetate membrane with 30 wt% silica nanoparticles prepared in HCl gelation medium (pH 1) [33]

With regards to rejection rates, the membranes were tested using BSA solution. The rejection rates decreased from 49% for pure CA membranes to 10% and 13% for CA-30 wt% SiO₂ in HCl and CA-30 wt% SiO₂ in NaOH gelation medium respectively. The membranes were also tested for oil separation in a 900 ppm oil/water emulsion solution. All membranes gave the same rejection rate of 99.8% regardless of the presence or absence of silica nanoparticles, or gelation medium type. Permeation rates for BSA solutions were not investigated. However, oil/water flux rates were studied. The pure water flux rates over the first 30 minutes were as high as ~400 L/m²h that decreased to ~100 L/m²h on the introduction of the oil/water emulsion. When the membrane was washed to be reused for the second, third, and fourth times, it gave the same pattern of flux change regardless of the gelation medium and silica concentration for all CA-silica membranes (except for 0 wt% silica). This indicated that the CA-silica membranes have antifouling effect for organic compounds, i.e. the oil droplets adsorbed and desorbed easily on and from the membrane surface and the membrane could be easily washed with pure water to be reused for further cycles.

2.2.3 Effect of Using Polymer Blends

Attempting to enhance the membrane performance furthermore, Sivakumar et al. [31] added polysulfone (PSF), a polymer also used in manufacturing RO membranes, to the CA-PVP blend, such that the final CA/PSF content is always 17.5 wt% of the total stock weight. At 0 wt% PVP, the CA/PSF blend with composition 75/25 wt% respectively gave PWF of 48.1 L/m²h, which was about 3 times more than what blank CA membranes gave. Incorporating the three polymers together with compositions 7.5 wt% PVP and CA/PSF of 75/25 wt% gave PWF of 115 L/m²h, more than twice the PWF of CA-PVP membranes, and more than 8 times of what blank CA membranes gave. The research addressed the effect of enhancing water permeation on salt rejection rates. Table 2.3 shows the significant increase in permeation rates for individual 1000 ppm saline solutions of each metal ion with the increase in PVP content at constant CA/PSF composition.

Table 2.3 Permeation rates of metal ions using CA/PSF/PVP blend membranes [31]

Composition (wt%)		PVP (wt%)	Permeate flux ($1\text{ m}^{-2}\text{ h}^{-1}$)			
CA	PSf		Metal ions			
			Cu ²⁺	Ni ²⁺	Zn ²⁺	Cd ²⁺
100	0	0	2.3	3.5	4.4	9.9
75	25	0	18.9	20.7	26.4	29.9
75	25	2.5	19.5	24.7	31.5	39.4
75	25	5.0	40.5	43.5	45.0	46.7
75	25	7.5	47.5	51.9	55.3	58.6

However, the existence of large voids created by the addition of PVP reduced the rejection rates remarkably as illustrated in Figure 2.4.

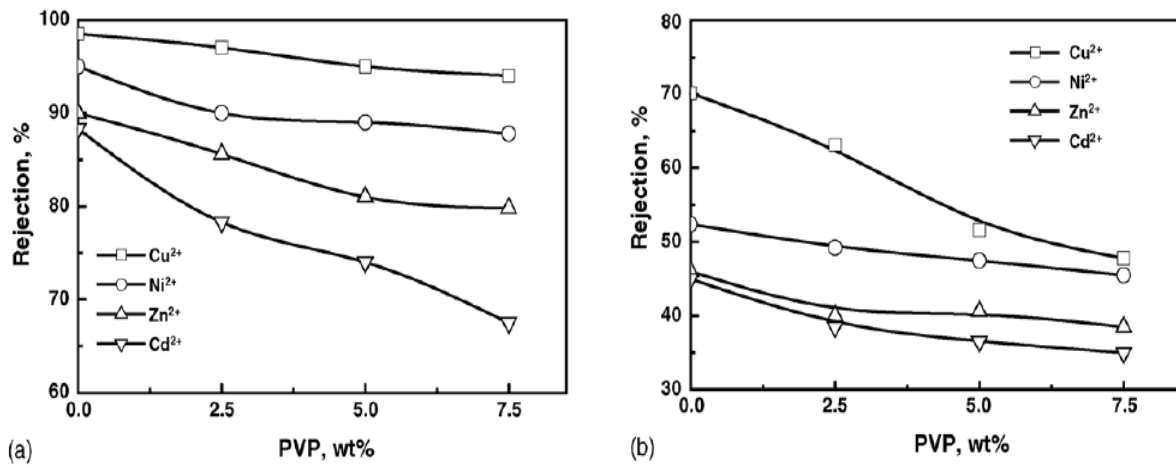


Figure 2.4 Effect of PVP wt% on metal ions rejection: (a) blank cellulose acetate, (b) 75/25 wt% CA/PSF [31]

A plausible explanation to the high permeation rates was that the incompatibility of cellulose acetate and polysulfone created repulsive forces between the polymers, which led to a macrophase separation during PI. This was further enhanced by the rapid percolation of PVP that speeded up the solvent/non-solvent demixing process, resulting in large numbers of macrovoids. Through visual inspection using SEM, it was clear that the more PVP wt% added, the larger the pore size especially the long finger like voids, for both the CA membranes and the CA/PSF blend membranes as shown in Figure 2.5. On the other hand, metal ions retention rates decreased significantly with both the increase in PVP and PSF contents since the pore sizes increased.

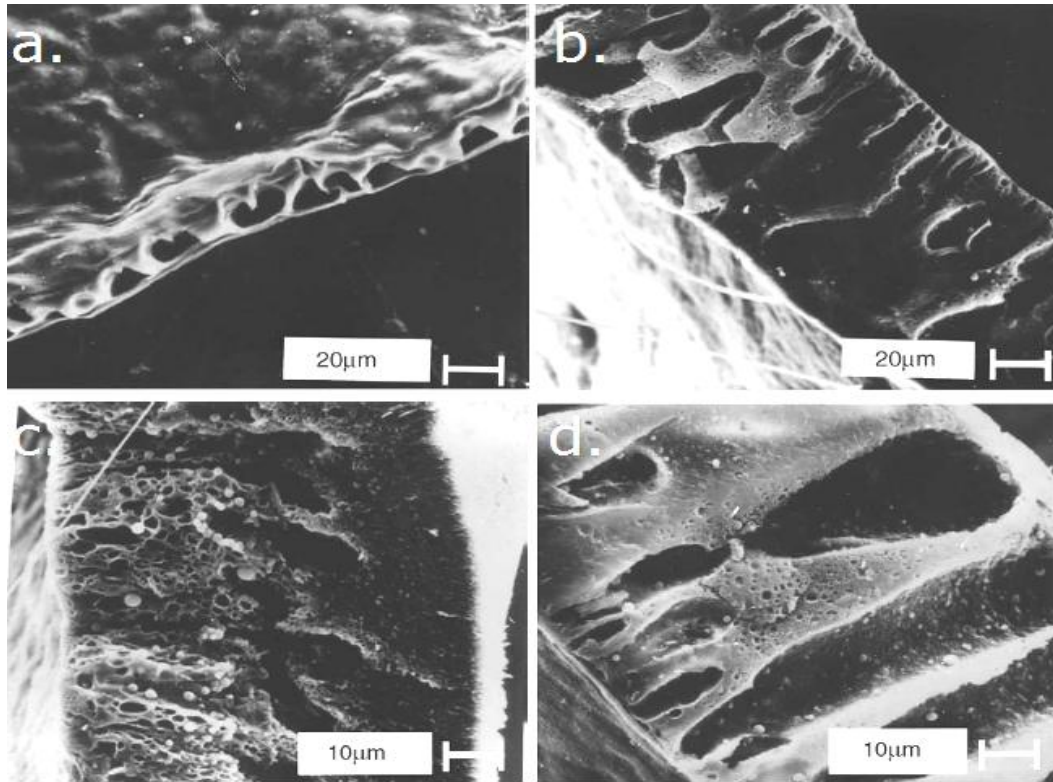


Figure 2.5 SEM of the effect of PVP on morphology; (a) 2.5 wt% PVP in 100/0 wt% CA/PSF respectively, (b) 7.5 wt% PVP in 100/0 wt% CA/PSF respectively, (c) 2.5 wt% PVP in 75/15 wt% CA/PSF respectively, (d) 7.5 wt% PVP in 75/15 wt% CA/PSF respectively [31]

Mahendran et al. [34] tried mixing CA with polyethersulfone (PES) to have a final polymer concentration of 17.5 wt% dissolved in DMF. They also used PEG 600 as an additive with different concentrations to study the resultant membrane performance. PI gelation medium contained distilled water as a non-solvent, 2.5 % (v/v) DMF that reduced the rate of the demixing process to reduce macrovoids volume, as well as 0.2 wt% SLS surfactant. Permeation rates were carried out at 3.45 bars transmembrane pressure, after subjecting the membrane to an initial transmembrane pressure of 4.14 bars for 4-5 hours until a steady flow rate is attained to eliminate any measurements errors resulting from membrane compaction. Trying different combinations for the concentration of the two polymers and the additive showed that 75/25 wt% CA/PES with 10 wt% PEG 600 gave the highest PWF rate of 275.7 L/m²h when compared to blank CA membranes that gave only 12.9 L/m²h as shown in Table 2.4. Trials of adding more than 10 wt% of PEG 600 to the blend failed since the blend solution became highly incompatible with the additive.

Table 2.4 PWF rates of CA/PES blend membranes with different PEG 600 additive concentrations [34]

Blend composition		Pure water flux at 345 kPa ($\text{m}^{-2} \text{hr}^{-1}$), PEG 600 concentration (wt%)				
Cellulose acetate (%)	Polyethersulfone (%)	0	2.5	5.0	7.5	10.0
100	0	12.9	37.2	50.3	80.6	89.2
95	5	21.7	45.8	61.7	92.6	94.0
90	10	28.5	51.3	78.9	110.8	151.6
85	15	46.1	62.4	90.6	140.8	196.3
80	20	55.8	74.1	121.8	233.0	236.5
75	25	66.5	80.8	144.5	251.1	275.7

Note: total polymer concentration at 17.5 wt%.

Such high PWF rates were suggested to be primarily due to the fact that PES is more hydrophilic than CA. Thus in PI, PES water's affinity accelerated the solvent/non-solvent demixing and created macrovoids large enough to allow water permeation with such high rates. The research suggested that the pore former PEG 600 solubility in water had no effect on the PI process, and that the low molecular weight PES (in comparison to that of CA) is mainly responsible for the morphology of the dense top layer of the membrane since PES precipitates faster than CA. The researchers didn't address, though, the reasons for using 2% (v/v) DMF in the gelation medium that was expected to slow down the demixing rate, even though they used a surfactant and a highly hydrophilic secondary polymer, both of which are used to increase the rate of the demixing. Furthermore, they didn't study the performance on the membrane in nanofiltration, but rather for ultrafiltration applications on proteins with different molecular weights that ranges from 20 to 60 kDa.

Boricha et al. [24] studied the performance of N,O-Carboxymethyl Chitosan (NOCC)/CA blend membranes with a compositions of 4/6 NOCC/CA dissolved in acetone. The solution was casted and left for complete solvent evaporation until a clear transparent membrane was formed. Since NOCC is water soluble, keeping it within the blend requires that it is cross-linked with the CA polymer. This was carried out by immersing the membrane in a solution of glutaraldehyde (GA) at 60°C for 1 hour. The membrane was then left to stand vertically for GA to drain, and any excess was washed out using deionized water. The membrane's performance was tested for permeation and rejection of a solution of 168 ppm and 74 ppm of chromium and copper respectively at different applied pressures, feed flow rates, temperatures, and feed pH. The highest permeation rate was found to be ~168 L/m²h, with ions rejection rates of 83.4% and 72.6% for chromium and copper ions respectively at 10 bars and feed flow rate of 960 L/h. It was also found that the permeation and rejection rates were directly proportional to the applied pressure and feed flow rate, thus, decreasing the pressure below 10 bars gave less cations rejection and solution permeation, which is a trend that was reported earlier by Haddad et al. [23]. As for the temperature effect on the membrane performance, it was found that with temperature increase, the permeation rate increased, yet, rejection rates decreased which is expected since temperature was expected to affect the membrane morphology and pore sizes. It could also affect the viscosity of the feed solution. Finally, pH effects were investigated and it was found that with pH increase, solution

permeation decreased, which is thought to be due to the shrinkage of the nanofilter membrane under the influence of pH increase, which is a behavior that was reported for different nanofilters in the literature [35]. As chromium and copper ions rejection rates, they were not significantly influenced by pH change, where chromium rejection rate increased with pH increase, and copper rejection rate decreased with pH increase.

2.2.4 Effect of Inorganic Additives

Inorganic additives include silica nanoparticles as mentioned in an earlier section that act as pore formers. Another example of inorganic additives is zirconium dioxide that was studied in filtration applications.

Filho et al. [36] prepared two membranes S1 and S2 with 13 and 11 wt% CA dissolved in acetic acid and acetone using PI with an ISE of 30 seconds. After having the membranes ready, ZrO_2 particles were developed into the membranes by hydrolysis through immersing the membranes in a solution of 2.2 wt% $Zr(PrO)_4$ -propanol for 6 minutes, and then immersing them in 0.0009M HNO_3 solution, individually. Membranes' final thicknesses were 90 and 150 μm , and zirconia contents were 0.59 ± 0.5 and 0.51 ± 0.5 wt% for S1 and S2 respectively. Permeation and rejection rates were carried out for 2.5 ppm phosphate ions solution at operational pressure of 1.72 bars. S1 and S2 showed flux rates of 22 ± 10 and 78 ± 12.6 L/m^2h , and rejection rates of 90% and 75% respectively. A blank membrane of S1 composition (without zirconia) was developed, and when tested for phosphate rejection, it gave 0% rejection. From this finding, it was assumed that the presence of zirconia is the main factor in phosphate retention. This was further supported by investigating the presence of phosphorous adsorbing on zirconia in the membrane using P^{31} nuclear magnetic resonance (NMR) technique. The characterization was done for $Zr(HPO_4)^{2-}$ versus $(HPO_4)^{2-}$, where both gave clear singlets due to phosphorous but the singlet of the $Zr(HPO_4)^{2-}$ was shifted to the right due to the presence of the Zr attached to the phosphate group, thus affecting the ^{31}P resonance energy as shown in Figure 2.6.

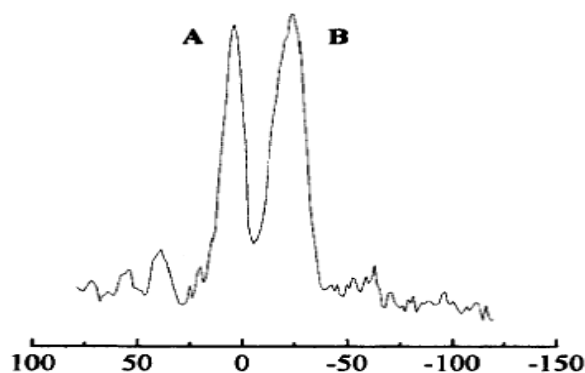


Figure 2.6 ^{31}P NMR of $(HPO_4)^{2-}$ vs. $Zr(HPO_4)^{2-}$. (a) singlet of phosphorous of $(HPO_4)^{2-}$, (b) singlet of phosphorous of $Zr(HPO_4)^{2-}$ [36]

Arthanareeswaran et al. [37] incorporated 0 to 7 wt% ZrO_2 microparticles in CA membranes, with a CA/ ZrO_2 ratio that is equivalent to 17.5 wt% of the total solution weight,

dissolved in DMF. PWF experiments were carried out at transmembrane pressure of 3.45 bars. The lowest PWF rate was found to be 15.6 L/m²h for the pure CA membrane. As ZrO₂ weight content increased, PWF increased to reach 46.7 L/m²h with the 7 wt%, which indicates an increase in the membranes pore sizes. This was supported by the pore radius and pore density values that were calculated using the membranes rejection rates for different molecular weight proteins like Trypsin, Pepsin, Egg albumin, and BSA, with average solute radius of 21.5, 28.5, 33, and 45 Å respectively. Table 2.5 is a summary of the CA/ZrO₂ ratios, PWF, pore radii, and pore density.

Table 2.5 Pore size and density and pure water flux of the CA/ZrO₂ UF membranes [37]

Membrane type	CA:ZrO ₂ ratio	PWF (lm ⁻² h ⁻¹)	Average pore radius, <i>R</i> (Å)	Pore density, number of pores/cm ² , $\eta \times 10^9$
CA-0	Pure CA	15.58	26.88	6.77
CA-1	9:1	20.25	33.93	6.98
CA-2	8:2	24.93	35.95	7.37
CA-3	7:3	43.62	38.82	7.99
CA-4	6.4	46.74	47.52	8.36

This work did not report the rejection rates of any of the membranes. However, one can deduce by comparing the pore sizes and average solute radii of the proteins that some membranes like the CA-4 is less likely to efficiently reject Trypsin or Pepsin. This could also be supported by the permeation rates of the proteins reported in the investigation, where the more the wt% of ZrO₂, the higher the permeation rates of protein solutions. For example BSA permeation increased from 5.19 to 19.79 L/m²h from CA-0 to CA-4, which applied for the rest of the proteins with different values. This increase can also be explained by the increase in the hydrophilicity of the membrane due to the inorganic additive, which allowed more BSA solution to pass through.

2.2.5 Effect of Using Carbon Nanotubes

Carbon nanotubes (CNTs) as additives have started to draw researchers' interest over the past ten years, especially with all the molecular dynamics simulations that strongly suggest that water passage through the nanotubes is expected to be exceptionally high as explained in the previous chapter. CNTs were added to polymers like polysulfones (PSF), aromatic polyamides, and chitosan in polymer based nanocomposites used in filtration applications, and there are reports in the literature that suggest changes in the produced membranes performance in terms of permeation and rejection rates. However, the use of CNTs/CA nanocomposites was not reported previously in the literature.

Choi et al. [38] prepared multi-walled carbon nanotubes (MWCNTs)/PSF blend membranes in the same exact manner used to prepared ultra and nano CA filtration membranes using PI. A known volume of NMP was divided into two beakers. PSF was completely dissolved in one. At the same time, CNTs were first functionalized by oxidation purification, and then fully dispersed into the other beaker of NMP in the other via sonication

for 80 seconds. Once the two stocks were ready, they were mixed thoroughly to have a final composition of CNTs-PSF/NMP of 15/85. As for the CNTs contents, they were varied from 0 to 4 wt%. Then the solution was cast at thickness of 150 μm and inserted in a coagulation bath of distilled water at room temperature for 24 hours to have a complete PI. Membrane performance was evaluated by measuring the PWF rates, and permeability and rejection rates for different solutions of 1000 ppm PVP and polyethylene oxide (PEO) at 1-4 bars operational pressure at room temperature. PWF increased with the increase in applied pressure, which was expected. PWF also increased with MWCNTs wt% until a flipping point at which the rate decreased. This was explained by the fact that the increase in CNT wt% increased the membrane hydrophilicity and pore sizes until a point at which too much of the CNTs resulted in small pore sizes that reduced permeation rate. This was also supported by SEM images of the pores and macrovoids of the membranes as in Figure 2.7.

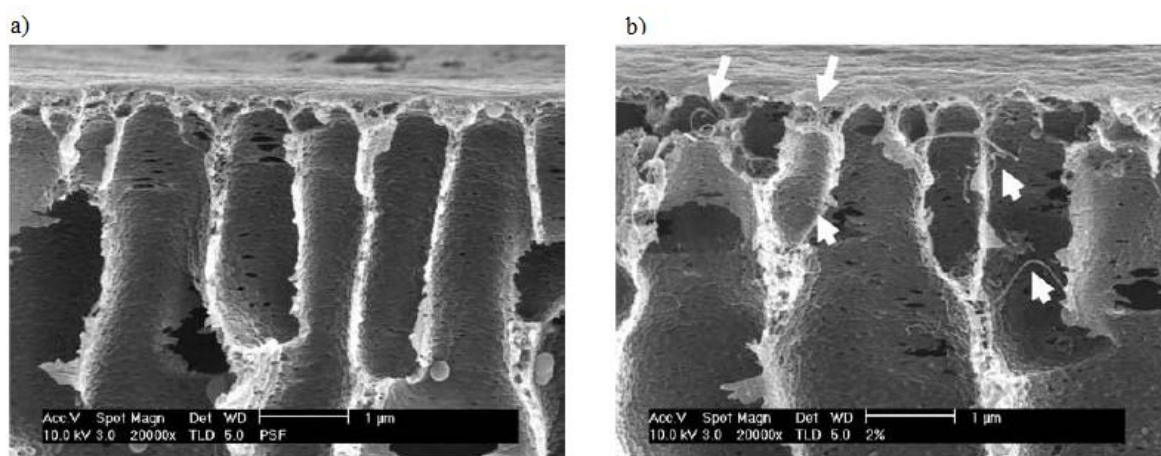


Figure 2.7 SEM of the cross section of CNTs/PSF membrane, (a) 0 wt% CNTs blank PSF membrane, (b) 2 wt% CNTs/PSF membrane [38]

The flipping point is thought to be due to the increase in CNTs/PSF stock solution viscosity, which affects the PI process. In viscous cast membranes undergoing PI, the solvents diffusion out of the cast is more favorable than the non-solvent diffusion into the cast, resulting in smaller pore sizes. Permeation measurements of PEO agreed with the results of the PWF when studying the effect of CNTs on the membrane, yet permeation rates were smaller than PWF due to the fouling effect from the accumulation of the polymer into the small pores. Rejection rates were found to be inversely proportional to the permeation rates, which is common for ultrafiltration membranes, and both permeation and rejection rates increased with the applied pressure. PVP showed a similar trend in permeation and rejection rates to PEO, but had higher values since PVP is smaller than PEO. However, PVP rejection rates decreased with the applied pressure since the size of the PVP molecules were small enough to pass through the membrane under the effect of increasing pressure. The paper concluded that CNTs could be a good improvement to the hydrophilicity of membranes used in filtration applications.

Qiu et al. [39] also embedded different wt% of modified CNTs into PSF membranes via PI. Here, CNTs were functionalized by oxidation purification first, then further by the

addition of isocyanate and isophthaloyl chloride (ICIC) functional groups to their surface. DMF solvent was used for both the dissolution of PSF and for CNTs dispersion. After having a homogenous CNTs/PSF stock solution, cast solution was immersed in distilled water coagulation bath for PI to take place. Ultra filtration tests were carried out for 50 ppm PEG solution at operational pressure of 1 bar and room temperature. PWF were also measured, and the results showed an increase in rates with the increase in CNTs content until a flipping point at which the rate started decreasing again, which agrees with Choi et al. [38] in trend, not in values. On the other hand, rejection rate trends for PEG didn't match the PWF trend as shown in Figure 2.8.

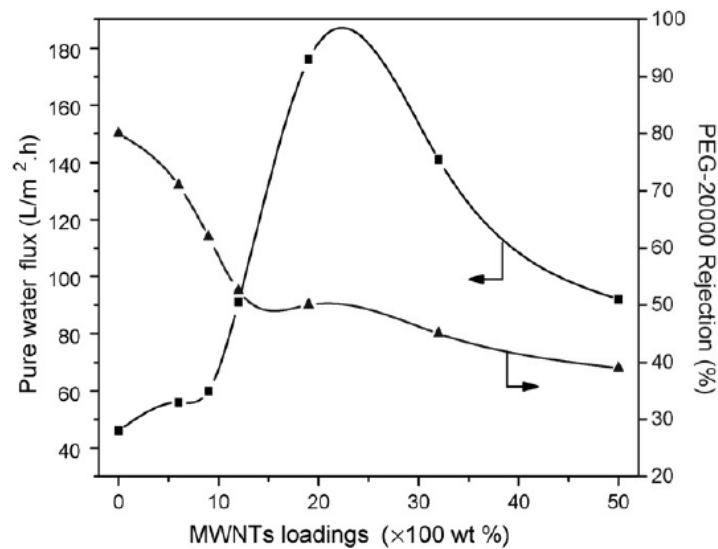


Figure 2.8 MWNTs contents effect on PWF and PEG rejection rates [39]

This decrease in rejection rates was explained by measuring the average pore diameter for different CNTs/PSF membranes. For 0, 0.12, 0.15, 0.19, 0.32, 0.5 wt% CNTs, the pore sizes were 5.2, 18.6, 25.7, 38.9, 34.1, and 30.3 nm respectively. Though the trend of pore sizes matches the rotation of PWF rates, it could also explain the reason behind the continuous decrease in rejection rates, since the pore sizes changed from 5.2 to 18.6 nm and above. This possibly meant that for better rejection to take place, the pores had to stay smaller than 18.6 nm. From Figure 2.8, the steepness of the rejection rate decrease was not large (within ~10% change), i.e. all pores resulted from CNTs addition were too large to reject PEG. Thus, CNTs managed to increase pore sizes in PSF membranes, and with the proper conditions and CNTs contents, membrane performance could be enhanced.

Tang et al. [40] prepared CNTs/chitosan nanocomposites with different concentrations of CNTs (ranging from 0 to 13%) added to 2% (w/v) chitosan. They also incorporated two different molecular weights pore formers PEG 6000 and PEG 10,000 to different solution blends, and used acetic acid solvent to dissolve/disperse chitosan, PEG, and CNTs. Instead of using PI, complete solvent evaporation took place, and followed by placing the resultant solid membranes in a water bath for the PEG to dissolve leaving a 130-140 μm porous membrane behind. PWF rates were measured to test the membrane performance at 1 bar and room temperature. For the membranes prepared with PEG 6K, PWF increased with the increase in

MWCNTs content until a flipping point at which the permeation rate started decreasing again. This agrees with the pattern found in the literature since the membrane pore sizes increase until a point at which too much of CNTs reduces the pore sizes. Interesting enough, the maximum PWF as a result of CNTs presence was 128.1 L/m²h, which was 4.6 times that of blank chitosan membrane PWF (27.6 L/m²h). Figure 2.9 illustrates how CNTs could block pores.

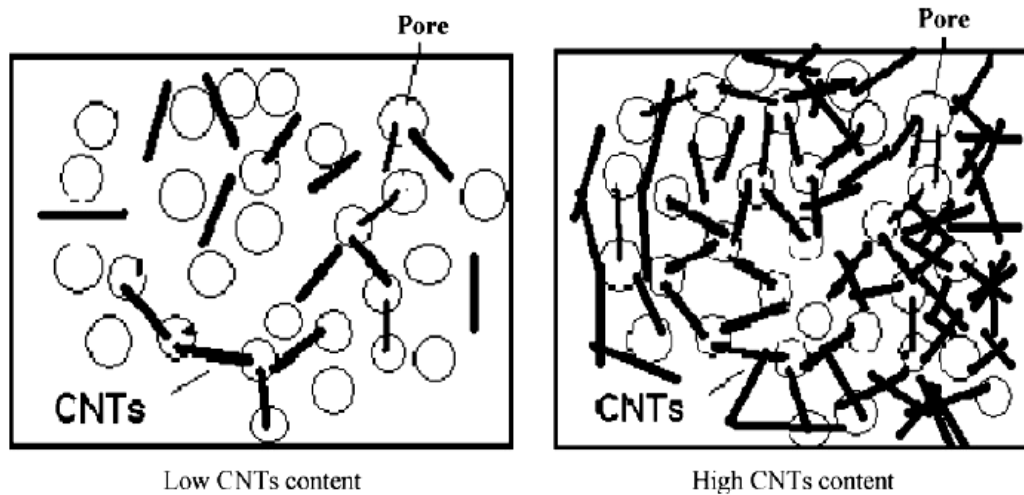


Figure 2.9 A schematic representation of how CNTs concentration can block pores, thus reduce pore sizes [40]

From the figure above, though CNTs could create alternative channels for water passage, thus increase flux rates, the increasing amounts of CNTs could block the existing pores thus reduce pore sizes. As for membranes prepared with PEG 10K, PWF values decreased with the increase in MWCNTs concentration, unlike PWF trend of membranes prepared with PEG 6K. This could be explained by the fact that PEG 10K created bigger pores than those by PEG 6K due to its larger size and its poor compatibility with chitosan. Thus, the further addition of CNTs to the membrane didn't significantly contribute to increasing pore sizes. On the contrary, addition of CNTs decreased the pore sizes, thus PWF rates.

Shawky et al. [41] prepared CNTs/aromatic polyamide (PA) nanocomposites using different concentrations of CNTs added to 10 wt% PA. The team didn't use the PI method, but rather complete solvent evaporation. N,N-dimethylacetamide (DMAc) was used for MWCNTs dispersion and PA dissolution. To prevent agglomeration, benzoyl peroxide was used to create free radicals on the polymer and the CNTs surface to maximize CNTs dispersion. After having a homogeneous mixture, the solution was cast and left in the oven for complete solvent evaporation, and a final membrane thickness of 200 μ m. Membrane performance, flux and rejection rates, was measured using a 4000 ppm NaCl solution at operational pressure of 39 bars at room temperature. The results showed that permeation rates decreased with the addition of CNTs. However, salt rejection increased significantly from 24% to 76%. Table 2.6 displays the results.

Table 2.6 Permeation and rejection rates as a function of CNTs concentration for 10 wt% PA at 39 bars and 25°C [41]

MWCNTs loading (mg/g)	Permeability (L/m ² /h bar)	Flux (L/m ² h)	Salt rejection (%)
0	0.76 ± 0.08	32 ± 0.7	24 ± 1.1
2.5	0.75 ± 0.09	32 ± 0.4	28 ± 1.0
5	0.73 ± 0.07	31 ± 1.1	35 ± 0.7
10	0.72 ± 0.10	30 ± 0.9	69 ± 0.9
15	0.71 ± 0.11	28 ± 0.8	76 ± 1.1

This large increase in rejection rates was believed to be due to the membrane compactness resulting from the strong interaction between the CNTs and the polymer matrix, thus creating a network structure responsible for enhancing salt rejection. On testing the same membranes with larger molecules like humic acid, an organic molecule that is larger than salts but much smaller than proteins and polymers, the 10 mg/g CNTs/PA membrane was able to reject up to 90% of the acid. That is to say, CNTs addition was able to enhance the membranes' performance significantly.

2.3 Research Aim

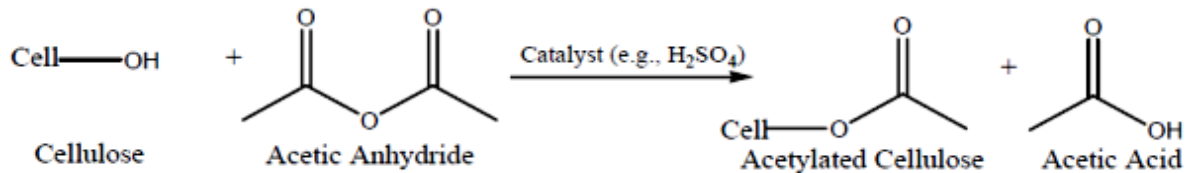
The thesis project aims at studying the effect of adding functionalized CNTs as nanofillers to cellulose acetate membranes, as well as studying the effect of varying the nanocomposite preparation conditions on the membrane morphology, and its performance in terms of permeability and selectivity in water desalination applications.

3 Theoretical Background

3.1 Cellulose Acetate in Desalination

3.1.1 CA Structure and Properties

CA is a relatively cheap, mechanically tough, chlorine resistant, hydrophilic abundant polymer [28, 42-44] that results from the acetylation of cellulose as in the reaction below [14]:



As mentioned earlier, CA membranes were first developed in the 1960's to become the first high flux asymmetric (anisotropic) membranes, used in a large number of applications including reverse osmosis, micro, ultra and nanofiltration, gas separation, water desalination, and wastewater treatment [21, 44-46].

Water permeation and salt rejection rates are affected by the acetylation degree of CA. In general, cellulose structure has three OH groups that could be partially or fully substituted. Completely substituted cellulose by three acetate groups (equivalent to 44.2 wt% of acetyl groups), known as cellulose triacetate, was found to have high salt rejection rates of 99.5% from seawater feed, while water flux is the lowest possible. On the other hand, lower acetylation percentage gave higher permeation rates but with lower salt rejection. The commercial cellulose acetate membranes used in RO desalination for example have 40 wt% acetate, equivalent to acetyl content of 2.7 on the scale of 0 to 3, where 0 means the 3 OH groups were not substituted, while 3 means fully substituted. Those membranes can yield 98-99% salt rejection rates at reasonable water fluxes [47].

Regarding membrane fouling, CA membranes are relatively protected from biofoulants due to their hydrophilic smooth surface, which doesn't leave inter-membrane gaps or interfacial water-resistant areas for foulants to grow. Being chlorine resistant (up to 1 ppm of continuous exposure to free chlorine) helps in using them in high bacterial count water sources, pretreated with chlorine [21, 45, 47-48]. CA membrane surfaces are also neutrally charged, thus reducing the charged macromolecules fouling.

On the other hand, CA membrane surfaces change with the increase in temperature due to the formation of a dense layer that requires high pressure to diffuse water through. Typical operational temperature range is 30-50°C maximum. Beyond that, the membrane may be hydrolyzed and degraded [45, 47-48]. Furthermore, CA membranes could also be hydrolyzed by pH changes in the medium. This limits their usage in treatment of water with organic foulants since the tolerance pH range is narrow (only 4-6) [45, 47-48] as shown in Figure 3.1.

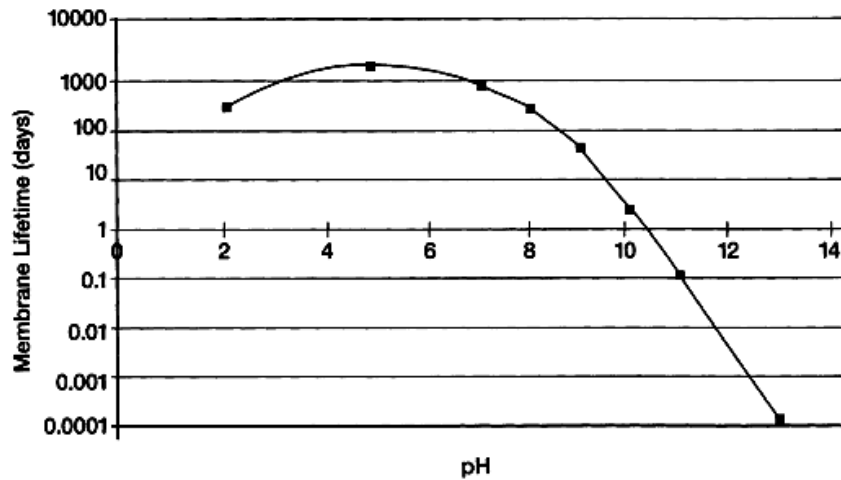


Figure 3.1 Membrane lifetime vs. pH [48]

CA membranes' main application is for brackish and seawater desalination at an operational pressure of 15-30 bars, above which the membrane surface is literally “crushed”, forming a compact dense layer that prevents water or salt passage. This range is significantly smaller than the earlier mentioned in section 1.2.3, making the RO process using CA membranes cost effective and energy saving [21, 45, 47-48].

3.1.2 CA Membrane Preparation

The most common preparation method of CA membranes is known as PI or wet phase separation process. In this method, CA is first dissolved in a solvent until a clear solution is attained. Then, on a substrate, usually glass, the solution is homogeneously spread using a casting knife to maintain a uniform casting thickness, as shown in Figure 3.2.

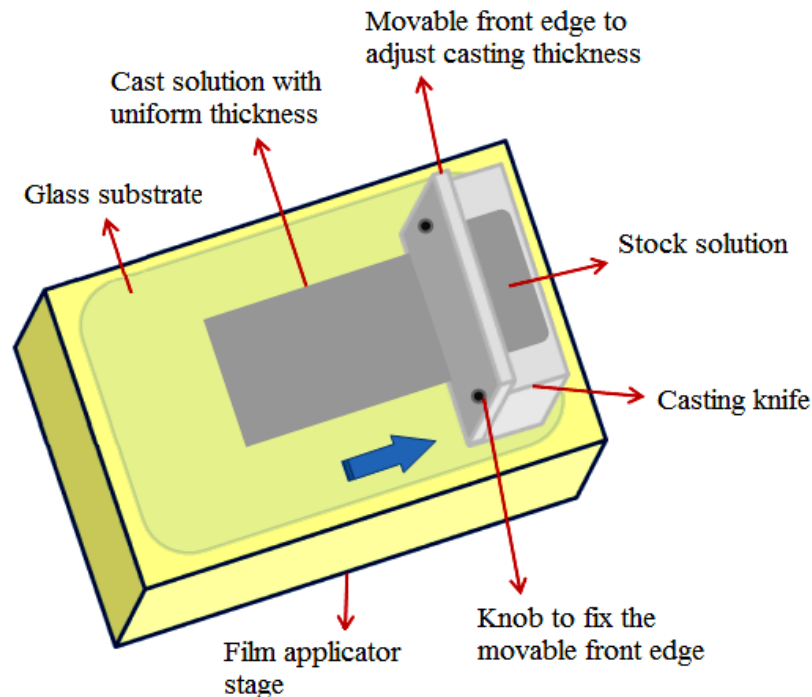


Figure 3.2 Schematic diagram of a film applicator and a casting knife

The cast film is then immersed into a coagulation bath filled with a CA non-solvent solution, usually water that is highly miscible with the solvent used. At this point, liquid-liquid demixing takes place, where the cast solution starts developing a dense nascent skin layer which is either nonporous or has very small pores (nanometers in diameter) on its top surface. This is the result of an immediate polymer precipitation at the top layer once the cast solution is in contact with the non-solvent. Below that layer, a phase separation process takes place due to the invading non-solvent, resulting in a polymer rich and polymer lean phases. The polymer rich phase consists of the solidifying CA polymer that is being drained out of its solvent. The polymer lean phase consists of the extracted solvent mixed with the non-solvent solutions [30, 49]. The polymer rich phase starts shrinking since more solvent is being expelled into the polymer lean phase via diffusion. As for the polymer lean phase, nucleation (pores) develops as a result of solvent-non-solvent exchange within the membrane, where nucleation grows as long as demixing continues [30, 49]. Figure 3.3 gives a schematic interpretation of how demixing takes place.

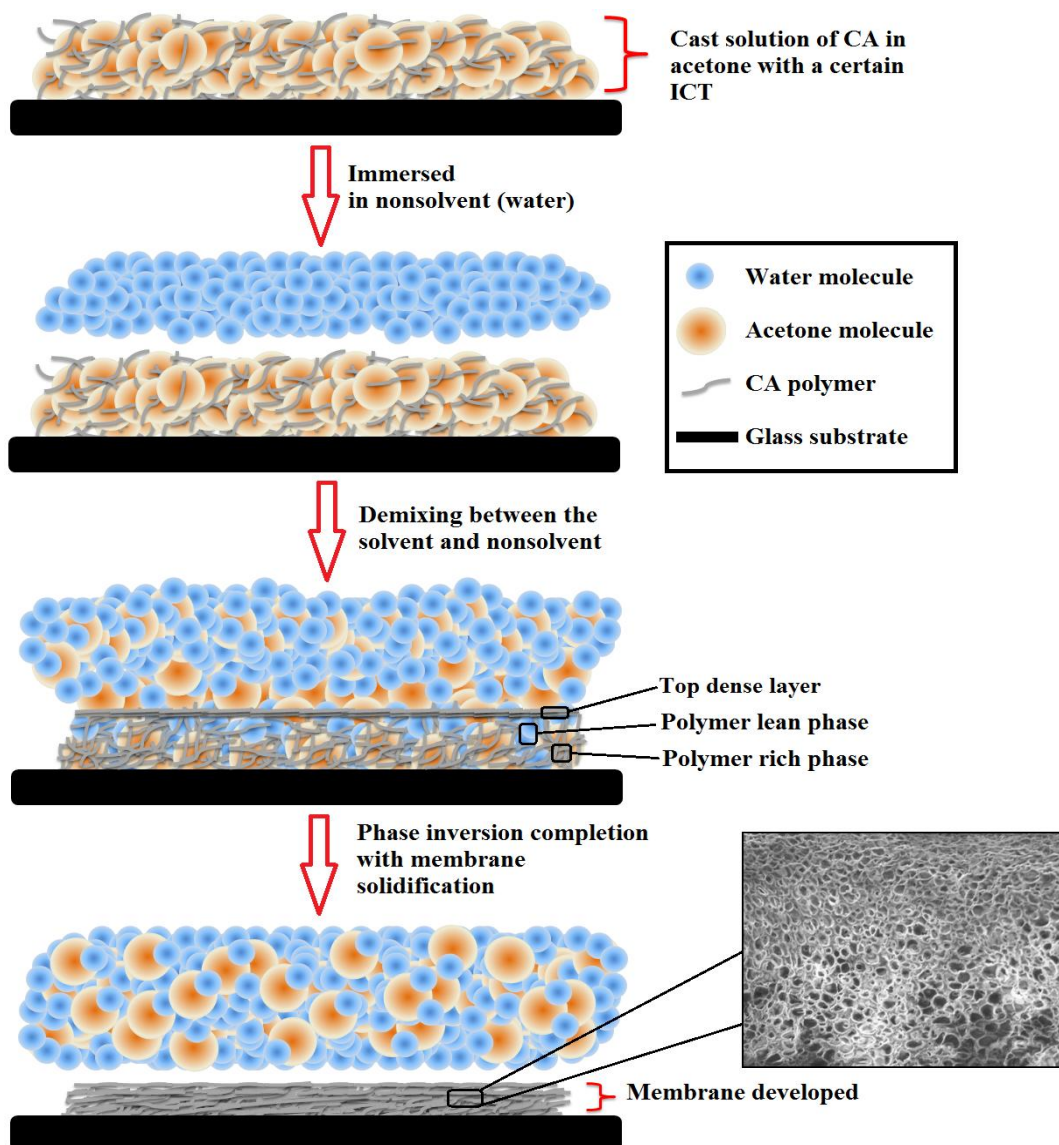


Figure 3.3 Interpretation of the demixing process

A post treatment step could be used in modifying the membrane morphology, known as annealing. At this step, the membrane is placed for a short period of time (few minutes) in a hot water bath after PI. This is used to compact the nascent top layer and narrow the pores size so that the membranes' retention ability is enhanced [18], where high temperature gives the top layer the ability to reorganize its crystalline arrangements to treat any defects on the membrane surface [50]. The membrane is finally placed in storage medium (usually distilled water) to remove the excess remaining solvent [30, 49].

There are two types of demixing that are controlled by the coagulation bath temperature, solvent types, and coagulation time [30, 49]. The first is slow (delayed) demixing at which the water/solvent diffusion and exchange is slow giving a symmetrical porous membrane. The slow diffusion requires several conditions to be present, most commonly are low coagulation bath temperature and solvents with low solubility property for the polymer. Figure 3.4 shows the different types of solvents and their effect on membrane porosity evaluated by membrane's water content.

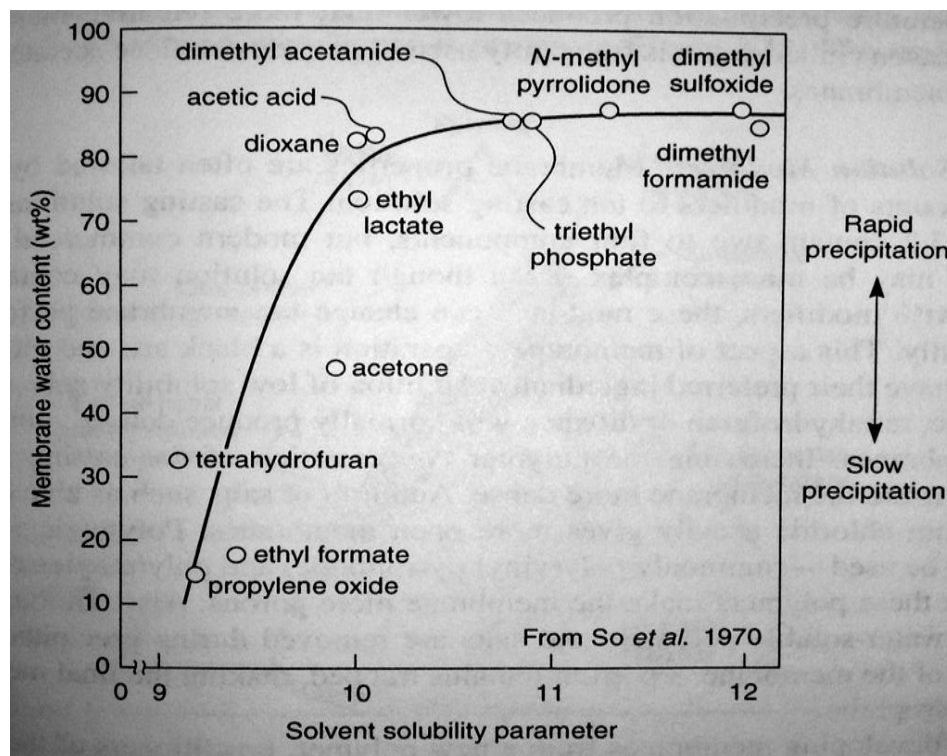


Figure 3.4 Chart elaborating the effect of solvents on membrane morphology [51]

The second type of demixing is instantaneous demixing at which long macrovoids are formed throughout the membrane since the precipitation process takes place in a very short time, leading to classical drop-like shaped voids appearing.

The mechanism of macrovoids formation has been explained by several ways. The main factors studied to suppress the development of macrovoids were found to be: a choice of a solvent-non-solvent with low tendency of demixing, the addition of the solvent to the non-solvent bath before cast solution immersion, an ISE before PI, and the increase in the polymer content in the cast solution which increases cast solution viscosity. Moreover, the

addition of the non-solvent to the polymer-solvent stock solution can suppress macrovoids formation if its content exceeds a certain minimal limit that could be evaluated experimentally [52]. As just mentioned, macrovoids are formed during the instantaneous demixing PI, where the non-solvent is trapped in the polymer lean phase. At the interface of the non-solvent at the boundaries of the nuclei, however, the type of demixing taking place was found to be different from that taking place throughout the rest of the cast solution. It was suggested, and later experimentally verified, to be delayed demixing. What happens is the solvent defusing into the non-solvent droplets is greater than the non-solvent defusing into the polymer rich phase, thus the size of the nuclei increase [52-53]. This can be explained by osmosis phenomenon, where inside the non-solvent droplets, the concentration of the expelled solvent keeps increasing to a point at which the rate of exchange of the solvent-non-solvent decreases, thus delayed demixing occurs at the same time as the surrounding polymer rich phase is shrinking and solidifying [54]. Figure 3.5 shows the different layers of an asymmetric membrane and the difference in the type of demixing occurring within the layers.

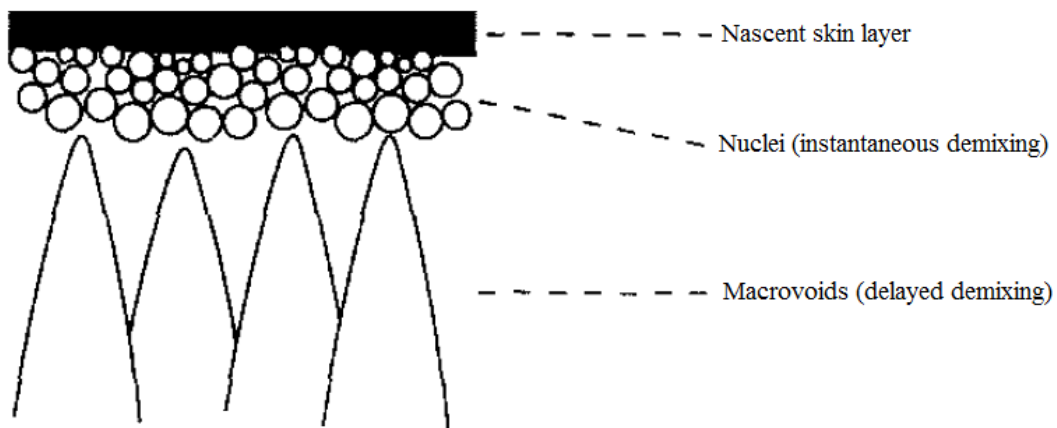


Figure 3.5 Schematic representation of an asymmetric membrane developed via PI, modified from [52]

3.2 Permeation and Retention Rates Calculation

To evaluate membrane performance in filtration applications, measurements of permeability and selectivity are carried out under applied pressure in a specially designed liquid cell as shown in Figure 3.6 [29]. In such a cell, the membrane is placed on a highly porous metal support at the bottom of the cell, with its top layer (the metallic side) facing the solution, since it is the layer that is expected to filter off the solute and allow the solvent through. Then a known quantity of the solution is placed on top of the membrane, and the cell is tightly closed. The inlet on the top of the cell allows gas in (usually nitrogen gas) to apply pressure on the system. Once a steady flow rate is attained from the outlet part at the bottom of the cell, the permeation rate is measured. The rejection rate can be measured as well by analyzing the permeate.

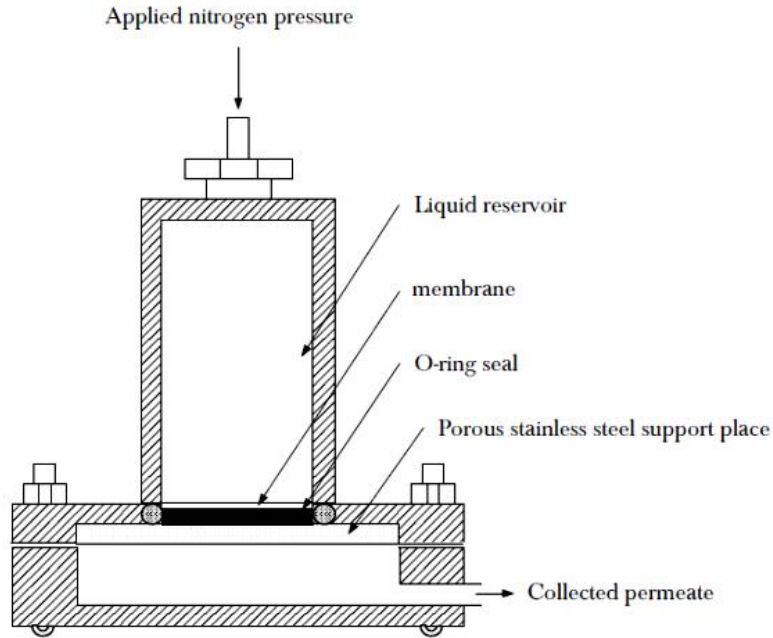


Figure 3.6 Permeation cell (modified from [29])

Mathematically, to evaluate membranes' performance under different pressures and facilitate their comparison with similar or even different membranes, liquid permeability P ($L/m^2 h \text{ bar}$) is calculated as such:

$$P = \frac{J}{\text{Appl. Prs}}$$

where J is the permeation flux ($L/m^2 h$), and *Appl. Prs* is the applied pressure (bars). As for the permeation flux rate, J , it is calculated using the following equation:

$$J = \frac{V}{A \cdot t}$$

where V is permeate volume that passed through the membrane (L), A is the total area of the membrane on which pressure is applied (m^2), while t is the time taken for the permeate to fill a certain volume V (h) [40].

On the other hand, salt retention rates, R , (%) is calculated from the following equation:

$$R = 100\% \times \left(1 - \frac{C_p}{C_f}\right)$$

where R (%) is an evaluation of how much solute is rejected by the membrane, C_p is the solute concentration of the permeate, C_f is the solute concentration in the feed solution [21].

Membranes' morphology can be manipulated by varying the preparation conditions such as CA content, initial casting thickness (ICT), coagulation bath temperature, and presence of organic or inorganic additives [28, 49]. It could also be manipulated by mixing CA with other

polymers to form a blend [22, 30], adding different types of inorganic compounds [42, 55], or by adding nanofillers like alkoxy silane [56] to form a nanocomposite.

3.3 Nanocomposites

A nanocomposite is a synthesized material made up of mixing two or more components, different in their physical and/or chemical properties to give a final structure with a preserved phase difference between its constituents. One or more of those components, called nanofillers, has one or more of its dimensions (length, width, or thickness) on the nanoscale, ranging in size from 1 to 100 nm [57-58]. Bones, for instance, are the natural example of nanocomposites since they are designed from organized layers of ceramic tablets and organic binders, giving a final structure of a remarkable difference in properties from its constituting components [59].

The exceptional high *surface to volume ratio* is the main factor controlling the structure/property relationship of nanocomposites, since particle size is directly related to particle number in a given volume [60] as shown in Figure 3.7.

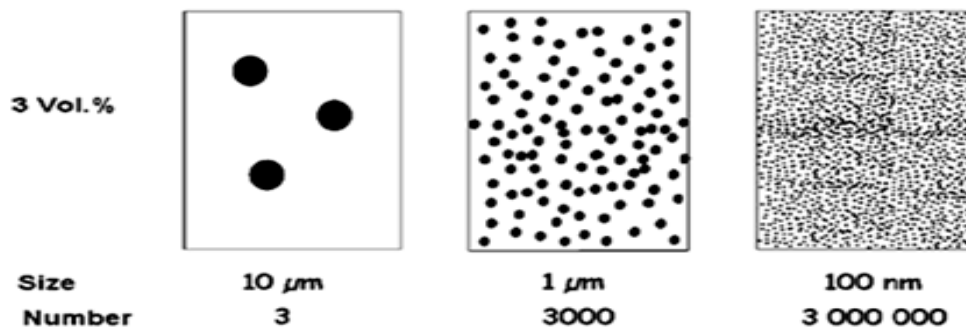


Figure 3.7 Illustration of how the particle number increase as their sizes decrease in a given volume [61]

In a fixed volume, say 3% as in the figure, nanofillers occupy more space than larger particles of the same material, leading to more surface exposure at the interface, i.e. an enormous increase of the interfacial area [61]. This directly affects the nanocomposites' properties to become dependent on the size of the nanofiller, since properties are dominated by the strong interactions at the interface between the nanofiller and the corresponding filled matrix without even a significant change in the density of the latter [57, 60-61].

In order to maximize the use of the interfacial properties, designing nanocomposites is controlled by two important morphological conditions. First, nanofillers must be homogeneously distributed within the matrix without any agglomerating particles in order to avoid reduction in interfacial area and surface to volume ratio. Second, the surfaces of the nanofiller and the matrix have to be compatible in order to achieve the best possible interaction between them to assure an effective load transfer across the nanocomposite, since under the effect of external forces, like an applied RO pressure on a non-properly interacted nanofiller-matrix nanocomposite, the stress will not be uniformly distributed, leading to the rupture of the nanocomposite. Furthermore, without proper interactions at the interface, the

matrix properties wouldn't be modified since they are dominated by the interactions at the interface as just explained [61].

Nanocomposites membranes can be prepared by several methods, including PI. Yet, there are two additional steps in the previously explained procedure. The nanofiller is first functionalized to create the best possible interaction at the interface between them and the matrix. The second step is having the nanofiller homogeneously mixed with the polymer solution before casting takes place, to guarantee the formation of a nanocomposite without any bulky agglomerating particles [61].

Polymers offer a great option for matrices that can be reinforced by the different types of nanofillers such as clays, ceramics, nanowires, and nanotubes. CNTs in particular have been of a major interest for researchers due to their unique structure, novel properties, and wide applications, as will be explained below.

3.4 Carbon Nanotubes as Nanofillers

3.4.1 CNTs Structure and Properties

In 1991, Sumio Iijima attempted to vaporize graphene sheets using the high current arc discharge process, but instead, he observed using a high-resolution electron microscope that the graphene sheets wrapped up to give a hollow tubular shape of elongated fullerenes. This novel arrangement of carbons is capped at each end, and the walls are made of hexagonal bonded carbons with a single crystalline conformation. The nanotube diameter is around 10 nm, its length is a few micrometers long, which makes it 1000 times more than that of the diameter [62-65].

There are two classes of CNTs, classified according to their structure. The first class is Single Walled CNT (SWCNT), which are wrapped single layers of graphene sheets, and which usually exist in bundles or ropes, with an outer diameter of 10-30 nm. The orientation of the carbon-carbon bonds compared to the tubular axis divides SWCNTs into three subgroups: i. armchair nanotubes whose carbon-carbon bond is perpendicular to the nanotube axis, ii. zigzag nanotubes, whose carbon-carbon bond is parallel to the nanotube axis, iii. chiral (helical) nanotubes, whose hexagon bonding carbons are wrapped up in a helical shape around the axis of the nanotube [63, 66].

The second class of CNTs entails MWCNTs. Those are what was originally observed by Iijima before catalyzing the process two years later to manufacture SWCNTs [63]. A MWCNT is a group of concentric coinciding SWCNTs whose diameters increase successively outwards, yet, remain within the nanoscale dimensions. The number of shells could be as large as a dozen [63]. Figure 3.8 gives an idea of the shapes of SWCNTs and MWCNTs.

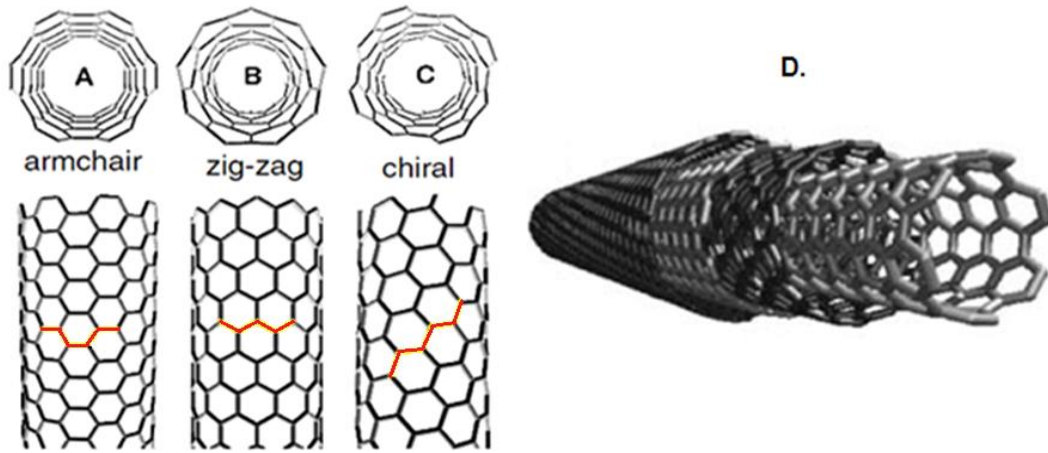


Figure 3.8 (a), (b), (c) SWCNTs different structures with highlight on C-C bond orientation vs. the nanotube axis [67], (d) MWCNTS structure [63]

Mathematically, CNTs conformations are specified by their two integer rolled-up vectors (n, m) [64] which are used to calculate both the diameter (d) and the chiral angle (θ) of the nanotube from the following equations [68]:

$$d = \sqrt{3} \frac{(n^2 + m^2 + nm)^{1/2}}{\pi} a$$

where a is the distance between two bonding carbons and it is equal to 1.421 Å [68], and

$$\theta = \arctan\left(\frac{\sqrt{3}m}{m + 2n}\right)$$

where θ ranges from 0° to 30° . For instance, zigzag nanotubes have $m = 0$ at $\theta = 0^\circ$, armchair nanotubes have $n = m$ at $\theta = 30^\circ$, and helical nanotubes have $0^\circ < \theta < 30^\circ$ [68] as shown in Figure 3.9.

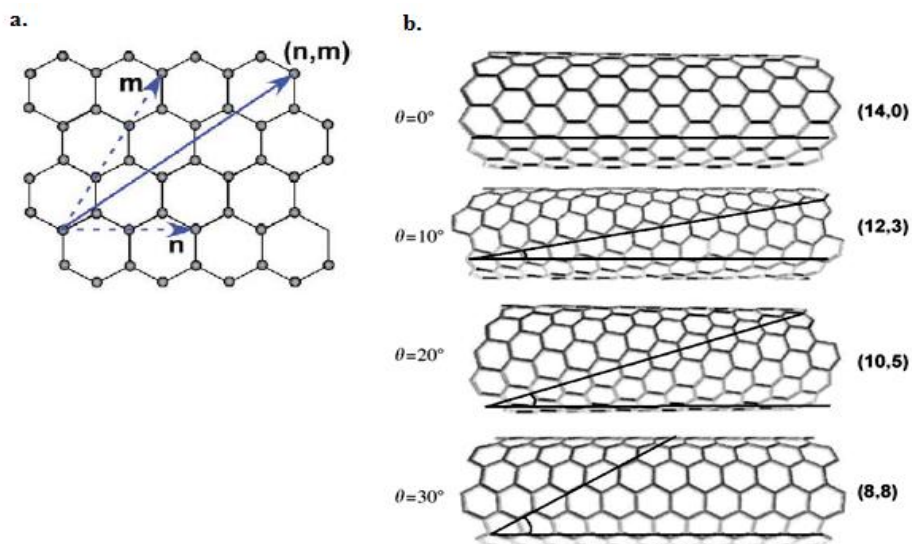


Figure 3.9 (a) (n, m) vector indication [64], (b) Different conformation of CNTs, their chiral angles, and indices [68]

CNT structures are considered to be one of the strongest in nature due to the “covalent in-plane” bonding between carbons, similar to the bonding type between carbons of the unfolded graphene sheets [65]. This strongly influences CNTs thermal, electrical, and elastic properties in exceptional ways, where for example SWCNTs stiffness is comparable to diamonds, tensile strength is much higher than that of steel, density is half that of aluminum, electrical conduction is comparable to copper wires, thermal conductivity is nearly double that of diamonds, and last, but not least, SWCNTs are thermally stable up to 2800°C in vacuum and 750°C in air, while metal wires (for example in the ones used in microchips) would melt at 600–1000°C [62, 69-70].

Ideal nanofillers for polymer matrices as they may seem, CNTs are highly stable, that it is extremely difficult for them to interact chemically or physically with other materials such as solvents, polymers matrices, or other nanofillers. They are insoluble in water or organic solvents. They are wet resistant and tend to agglomerate in clusters due to the high van der Waal interaction between them, making their dispersion into solvents very challenging. As for penetrating their bonding system, it requires very high energy to rupture due to its high stability. Their ends caps are closed so they cannot be used as channels for fluids transportation [62, 70]. For these reasons, CNT functionalization is crucial for creating functional groups on CNTs surfaces to allow them to interact with other materials, as well as for opening their ends caps to allow them to act as transportation channels for fluids.

3.4.2 Functionalization of CNTs by Oxidation Purification

Oxidation purification is the most common method used for functionalizing CNTs with the purpose of homogeneously mixing them with polymer matrices. In this process, carbons on the defected sites of the crystalline structure of CNTs, or on the sites of misaligned π bonds, or usually on both, get oxidized giving COOH hydrophilic groups [63, 70]. The process involves using concentrated nitric acid, sulfuric acid, or a mixture of both to reflux CNTs for a period of time defined according to the reaction conditions [63, 70]. Then the functionalized CNTs are washed several times until they are neutralized at pH 7. They are then washed with drying agents such as acetone and THF to remove as much water as possible. Finally, they are dried under vacuum to be ready to use [71]. Figure 3.10 shows how the CNTs look like after oxidation.

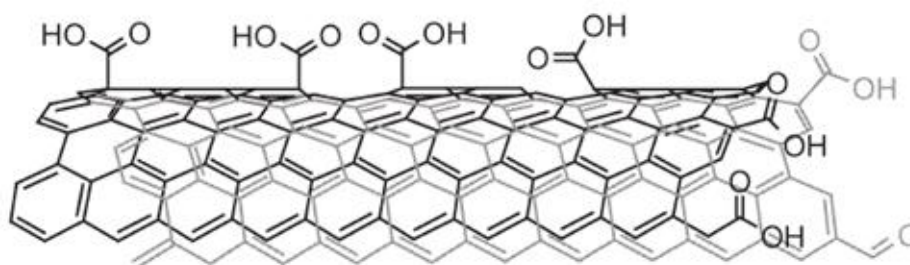


Figure 3.10 Section of an oxidized CNT reflecting terminal and wall oxidation [71]

3.4.3 CNTs in Water Desalination and Treatment

In water treatment and desalination, CNTs continue to surprise scientists, where a nanocomposite filled with open ended CNTs was found to pass water at flux rates significantly higher than using the same matrix without the nanofiller. Additionally, CNTs-polymer nanocomposites can stand high transmembrane pressures up to 1 atm, indicating that the membranes don't easily crush due to macrovoids or surface flaws under the effect of applied pressures [16, 38, 41, 72]. As for salt rejection rates, they could be improved as well [16]. CNTs were also found to exhibit cytotoxic properties for bacteria, which could be used as a resort for RO membrane biofouling problems [72].

A major drawback in using CNTs for water desalination is the fear of environmental contamination with CNTs waste disposed from production plants, which would eventually enter into the human food chain. This raises many questions since studies on CNTs' effects on mammalian cells include pulmonary inflammation (inflammation of lung tissues), cellular proliferation (multiplication of cell numbers by division), heart growth inhibition, and toxicity [72]. CNTs are also classified as '*hard*' biopersistent, hence, they are not cleared from the human body through excretion [73]. However, having strictly controlled disposable management system would reduce their release in nature. Moreover, studies showed that if CNTs are homogeneously dispersed within membranes, they are more likely to have minimal toxic effect on humans, since toxicity is achieved by agglomerated CNTs more than by the dispersed. So it all pours into proper functionalization of CNTs to prevent their agglomeration with the membrane matrix in which they are impeded [72].

Though water transport through hydrophobic channels is still not well understood, the experimental results were conclusive: water pass at exceptional high rates through CNTs. Attempting to clarify the transport mechanism, scientists resorted to molecular dynamics simulations and compared them to the experimental results.

3.5 Inside CNTs Molecular Dynamics (MD)

MD are computer simulations methods that study molecular transport mechanisms, since short time scale and small particle sizes (nanoscale or smaller) obstruct real time experimental measures. Using Newton's laws of motion, initial molecular configurations, and Lennard-Jones potential energy functions (functions that calculate intermolecular potential energies and forces), molecules' location and momentum trajectories in space could be estimated [74]. In other words, MD could be used to predict how water molecules would behave inside a nanotube in terms of position, arrangement, bonding properties, and interaction with the hydrophobic CNTs walls, and how these behaviors compare to entering a wider diameter microscale or even larger tubes.

MD simulations estimate that the smallest possible CNT for water molecules to enter into is the (5, 5) with $d = 6.78 \text{ \AA}$, and any smaller nanotubes, like the (7, 1) and the (5, 4) with $d = 5.91$ and 6.12 \AA respectively don't allow water passage [68]. On filling CNTs, water molecules are accommodated in one of three ways, either wire mode, layered mode, or bulk

mode. The type of mode is determined by the diameter of the nanotube, since molecular conformation transition takes place from bulky-like to layered-like when water molecules are squeezed in a solid structure of approximately 1 nm or less [68, 74]. As for water density, it changes significantly according to the size of the nanotube, but it is independent of the CNTs' chirality. For example, a nanotube with diameter of 7.8 Å is expected to affect water density to become as small as 0.2 g/cm³ compared to the bulk water density of 1 g/cm³ [68].

Wire mode is a one dimensional ordered conformation of water molecules in which the probability of finding hydrogen and oxygen atoms in the center of the CNT is maximal, and the hydrogen-bonded molecules rearrange to form a water wire along the nanotube axis (Figure 3.11), hence the name [64, 68].

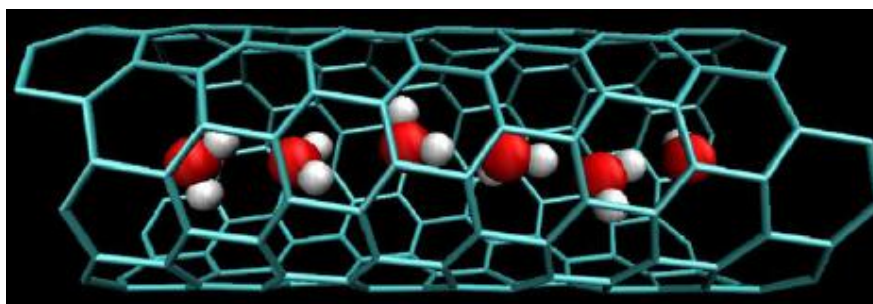


Figure 3.11 1D wired mode of water molecules inside (8, 2) CNT [68]

What happens is when the tetrahedral hydrogen bonded molecules approach the nanotube, two of the hydrogen bonds are broken, while the remaining two rearrange in a highly oriented linear chain like. The average lifetime of those H-bonds is estimated to be 5.6 ps, which is five times longer than the lifetime of H-bonds in bulky water conformations. The OH groups engaged in the H-bonds are estimated to be nearly in the center of the nanotube, and they flip directions approximately every 2-3 ns [75-77].

Despite the fact that losing two hydrogen bonds is energetically unfavorable (~10 kcal/mol), some of this energy is retained by the van der Waal's interaction between the water molecules and the carbons of the nanotube wall (~4 kcal/mol). To compensate for the rest of the remaining energy, MD simulations predict that entropy plays an important role since water molecules were found to have the ability to rotate freely around the H-bonds chain, creating a “degenerate energetic ground state” that is more occupied than the higher dominant free energy state [77].

In wider CNTs, a second layer of water molecules could squeeze in (layered mode), forming helical like conformations such as in the (10, 5) CNTs. Increasing the diameter of the CNTs creates more space inside the nanotube to form a ring like layer with a wired water chain trapped in the middle of the ring [68]. Further increasing the diameter like in the (10, 10) nanotubes creates more spiral confirmations that MD suggest to be due to the presence of π electrons of the carbon-carbon bonds along the nanotube [78].

As the diameter increases, more layers are added until water molecules reach a point of not sensing the surrounding CNT walls, i.e. the bonding carbons become too far away to have

an effect on the orientations of the water molecules. At this point, water starts acting as a bulk-structure (bulk mode) [68]. Figure 3.12 shows different water orientations inside CNTs.

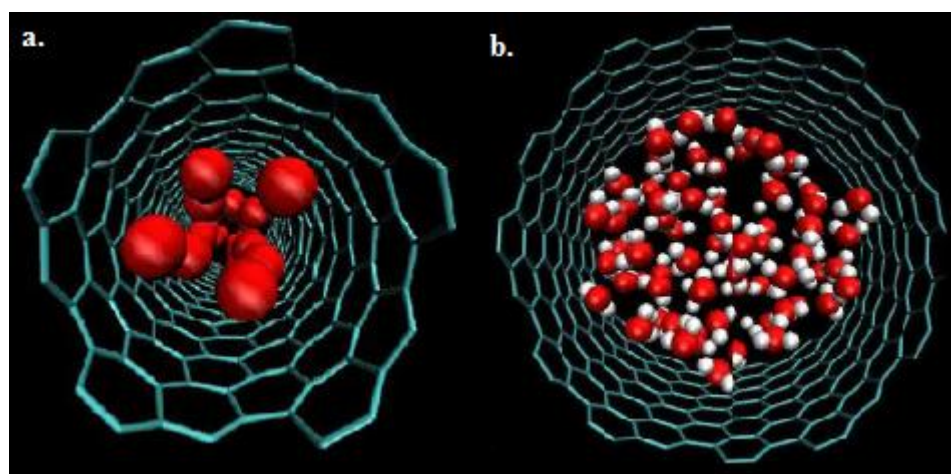


Figure 3.12 Water molecules structure inside CNTs (a) Spiral-like layered mode, (b) bulky mode [68]

Experimentally, water fluxes through CNTs were found to be exceptionally high as mentioned before. MD suggest that this is due to the significantly smooth chemically inert graphene inner walls forming the nanotubes [64, 79]. Moreover, the fact that water molecules have the capability of fluctuation inside the nanotubes results in a “drift-like motion” which highly accelerates the water flow across the nanotubes [77]. MD also suggest that the flow rates are not governed by the length of the nanotube, contrary to what classical macroscopic hydrodynamics models suggest [64, 79].

As for salt retention rates, MD simulations suggest that in order for a cation such as sodium or potassium ions, or an anion such as chlorine ions to be 100% prevented from passing into a nanotube, there is a minimal diameter required of ~ 0.4 nm, equivalent to the hydration shell around the ion. At this diameter, the ions have to lose parts of their hydration shell, which creates an energy barrier, high enough for ions not to favor passing through the nanotube (approximately ~ 120 kJ/mole) [64]. Since water cannot pass through this diameter either, MD simulations examined salts’ behavior in larger diameter nanotubes such as the (5, 5) vs. the (8, 8). MD postulates that 100% salt rejection is expected from the (5, 5) since its diameter (6.87 \AA) is narrow enough to prevent salts from passing through. However, only $\sim 60\%$ salt rejection is found for the (8, 8) due to its relatively large diameter (10.86 \AA). Any CNTs with diameters range between the (5, 5) and (8, 8) show different rejection rates. Furthermore, MD speculate that CNTs with diameters larger than the (8, 8) would allow free movement of small ions since the energy barrier is no longer there. Yet, there aren’t enough studies or experimental data to support these claims. There is one, however, that opposes them using (10, 10) CNTs with $d = 13.57 \text{ \AA}$, which postulates that there exist an energy barrier for Na^+ ions trying to pass through these CNTs [16, 64, 68].

3.6 Membrane Characterization

In order to evaluate whether a membrane could be used in filtration applications, several techniques are used to study its performance and morphology. For membrane performance, desalination measurements using a pressurized cell are carried out, and salt content is quantified using several techniques, the simplest of which is titration. As for morphology characterization, it can be done using scanning electron microscope (SEM), and porosimetric analysis via gas sorption.

3.6.1 Scanning Electron Microscope (SEM)

SEM is a powerful technique in topography analysis on the nanoscale, which has major applications in material sciences and nanotechnology. This is due to using an electron beam, of very short wavelengths that could identify small details on a sample surface and give images of features as small as 200 nm.

Basically, the sample is subjected to a ray of electrons and an image is being created from their elastic and inelastic scattering, as well as, the electromagnetic radiations (X-rays) generated by the sample. As shown in the Figure 3.13, the electrons are ejected from an electron gun which is usually a tungsten filament to reach an anode with an acceleration energy that could reach 1-30 keV. Then the beam is focused through three lens systems, till it hits the specimen, and gets scattered [80].

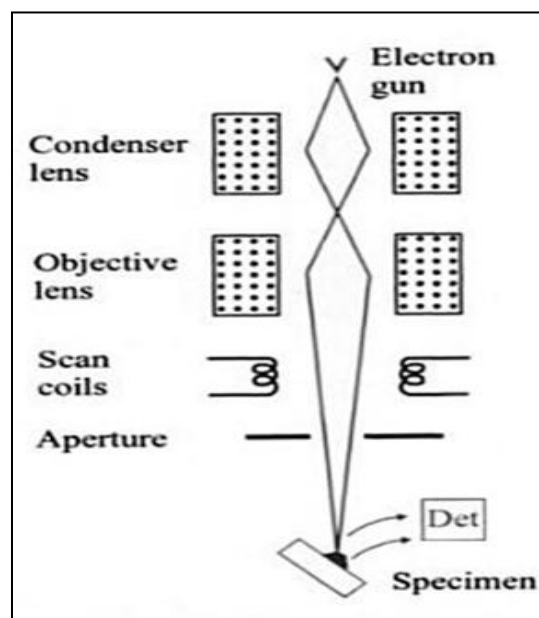


Figure 3.13 Schematic diagram showing the main components of SEM [80]

There are two different types of scattering: the back scattering, which is due to the electron beam hitting the electrons on the surface of the specimen and elastically bouncing back, with no exchange of momentum between the electrons on the sample and the electrons from the gun. Thus, the scattered electrons are reflected into discrete locations on a detector located right above the sample, and from these locations, the surface features of the specimen

could be formulated. The second type of scattering is the secondary scattering, which is due to the inelastic interaction between the electron beam and the electrons of the elements on the surface where exchange of momentum takes place, resulting in the ejection of one of the electrons of the K shell from the atoms on the surface. These secondary electrons are usually very weak (10 to 50 eV), and they are traditionally collected by Everhart-Thornley detector, where the secondary electrons hit a scintillator. The flashed light signals hit a photomultiplier which converts them into an electrical signal. This is then digitally output as a topographic image of the surface [80-82]. The third type of signal detected is the x-rays generated from the material which are collected using EDX detectors [80]. This type of signals is very useful in the qualitative analysis of elements found on the surface of a sample or within a mixture of compounds, since the generated x-rays are element specific [83].

Samples have to be conductive because, otherwise, bombarding them with electrons could result in static charges on a nonconductive surface, leading to noise in the sample image. In this respect, nonconductive materials are sprayed with a thin layer of a conductive coat, which is so thin that it takes the shape of the surface and doesn't modify its topography, hence, prevents charging. Figure 3.14 shows a single carbon nanotube with diameter ~12 nm at 400,000 X magnification.

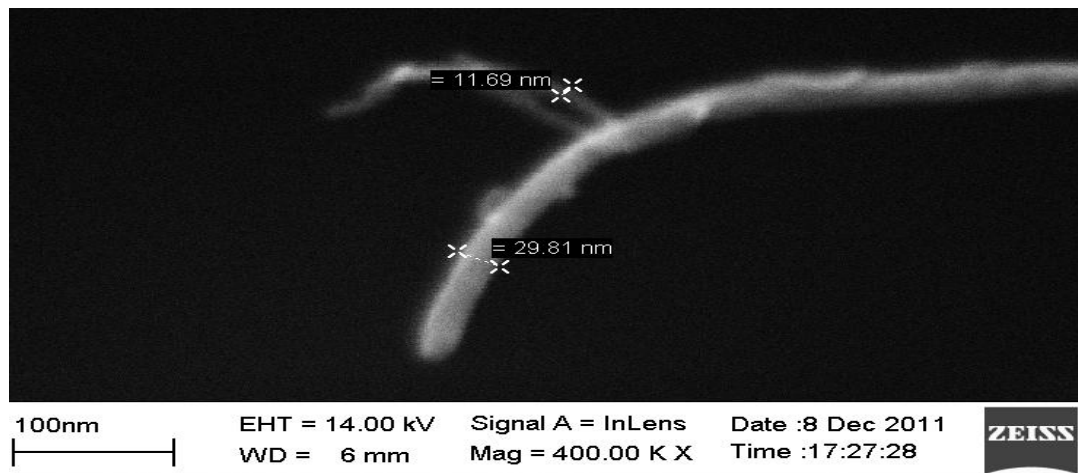


Figure 3.14 The dimension of a MWCNT

The huge magnification power of SEM makes it a very useful tool in topography analysis that allows a wide range of applications in nano-science.

3.6.2 Surface Analysis by Gas Sorption

Identifying pores sizes, quantity, and overall surface area of a porous sample is important in analyzing and interpreting its behavior, for example, in filtration applications, which depend on pore sizes to screen out dissolved particles. The most common method in porosity analysis is physisorption of a gas onto the solid surface, and by knowing the quantity adsorbed and the corresponding pressures, analysis is carried out.

Before explaining the process in details, some important terms have to be identified [84]:

- Micropores are pores smaller than 2 nm
- Mesopores are pores between 2-50 nm
- Macropores are pores larger than 50 nm
- Adsorption means the attachment of an element or a molecule, gas or liquid, onto a solid surface either physically via van der Waal forces (physisorption), or chemically via a chemical bond (chemisorption)
- Adsorbent surface is the solid substrate on which molecules adsorb or from which they desorb

The surface atoms of the solid have the ability to attract atoms or molecules from the surrounding medium via van der Waal forces [85-86]. Based on this, measuring the surface area of the solid could be carried out. The first step in the process is *emptying* the top layer on the sample surface from any adsorbate molecules, the most common of which are water vapor and carbon dioxide. This is done by a vigorous degassing process in which the sample is heated up (temperature selected depending on the sample type) under vacuum for several hours. Once the surface is free of adsorbate molecules, known increments of an inert gas, like N₂, Ar, or Kr are introduced, and the sample in contact with the gas is left to equilibrate so that some of the gas adsorbs on the sample surface. At equilibrium, the pressure in the sample vessel is measured, and from the original pressure and equilibrium pressure, the quantity of the gas adsorbed is obtained. Knowing the cross-sectional area of the gas particles allows the calculation of the sample surface area assuming monolayer formation. Figure 3.15 shows the stages of gas adsorption on the solid surface. It's important to note that this process is temperature dependent, and in this respect, the process is carried out at constant temperature [85-86].

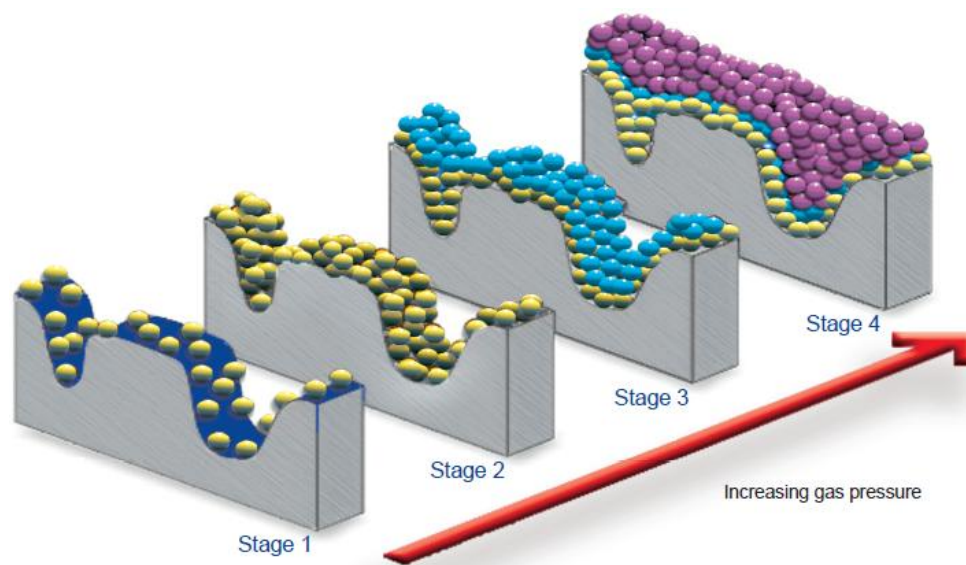


Figure 3.15 Different stages of gas physisorption on sample surface with pressure increase [85]

Translating the process into usable data, the first chart produced is called the isotherm, which represents the quantity adsorbed as a function of the measured pressure [87]. Yet, the pressure value is represented in the form of relative pressure P/P_0 , where P_0 is the saturation

pressure at which the gas and liquid phases of the adsorbate molecules can coexist together, at a specific temperature. There are 6 types of isotherms as shown in Figure 3.16.

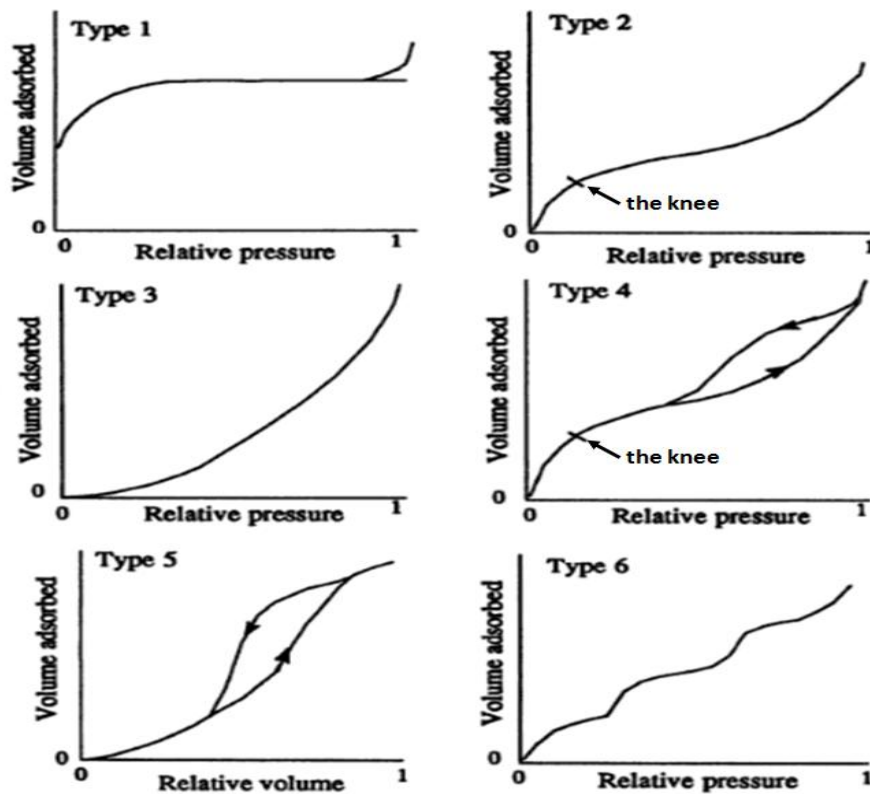


Figure 3.16 Different types of isotherm linear plots [84]

Type I, also known as “pseudo-Langmuir”, can be seen in chemisorption since the adsorbent surface becomes completely covered with only few molecules thick monolayer that formed a chemical bond with the surface, thus saturating the possible adsorption sites on the surface. As for physisorption, type I isotherms are common for porous solids with micropores. It is worth mentioning that the reason why it is also called pseudo-Langmuir is because Langmuir built his theory about sorbing gases while assuming that solid surfaces are covered with a monolayer of the adsorbate molecules. This is close to the truth for micropores since they are too narrow to be filled with multilayers, while it is pretty much the case in chemisorption, where type I isotherms have wider applications and used in more calculations [84, 87-89].

Type II isotherms represent adsorption on nonporous surfaces, or solids with macropores. The most important feature they have is the *knee*, which is assumed to be the point at which a total formation of a monolayer is complete, and the rest of the curve represents the different multilayers adsorbing [84, 87-89].

Type III isotherms represent a weak interaction between the adsorbate molecules and the adsorbent surface, which is clearly reflected by the disappearance of the knee. This takes place when the adsorbent surface has a weak potential to attract surrounding molecules to adsorb. In this case, the adsorbate molecules prefer to adsorb over one another in the form of

multilayers rather than adsorbing over the adsorbent surface. Example of such surfaces includes organic polymers [84, 87-89].

Type IV isotherms represent porous solids usually with mesopores. The plot has two characteristic features: the first is the presence of the knee as in type II isotherms, which serves the same purpose of identifying the starting point of multilayers development. The second feature is the presence of hysteresis which represents a desorption deviation from the adsorption curve. This was suggested to be due to the change in the mechanism of mesopores emptying from the adsorbate molecules as compared to the mechanism of their filling up [84, 87-89].

Type V isotherms represent porous solids also with mesopores which accounts for the hysteresis on the curve. However, the shape of the curve is very similar to type III isotherms because of the type of the adsorbent surface which also happen to have weak affinity towards the surrounding molecules. Thus, the development of a monolayer is not detectable since multilayers tend to develop at very low relative pressures [84, 87-89].

Type VI isotherms are very rare ones that represent adsorption on highly uniform homogenous nonporous surfaces. The characteristic feature on the plot is the presence of steps. Each step is thought to represent a new developing monolayer, and the height of the step is used to calculate the capacity of the developing monolayer (i.e. the quantity of adsorbate molecules forming the new layer). A very popular example of such isotherms is the one for the adsorption of argon on pyrolytic graphite [84, 87-89].

The data of isotherms are used to deduce surface areas, and pore size analysis is carried out by different models based on the type of the isotherm and the types of pores present. For this current research: the BET theory was used for adsorption isotherms interpretation and sample surface determination; the density functional theory (DFT) was used to profile the pore volumes and areas and develop pore size distribution; and the de Boer t-plot method was used to calculate the micropores volume and external surface areas (i.e. areas which micropores do not contribute in, like meso and macropores areas, as well as the area of the surface).

3.6.2.1 BET Method

The main contribution of BET is the idea of multiple layer adsorption. The rate of adsorption suggested to be equal to the rate of desorption was introduced by Langmuir for monolayer adsorption whereas BET made the same assumption for multilayers [87-88, 90].

The BET model succeeded in explaining isotherms II and IV that Langmuir's failed to explain. From their equation, a constant c could be derived and used mathematically in calculating the inflection point at which multilayers start forming. Furthermore, the c value was found to resemble the strength of interaction between the adsorbate molecules and the adsorbent surface, where the stronger the affinity between them, the higher the c value. The linear form of the equation is [91]:

$$\frac{P}{V(P_0-P)} = \frac{1}{V_m c} + \frac{c-1}{V_m c} \frac{P}{P_0}$$

where V is the total volume of the adsorbed molecules, V_m is the volume of the monolayer, and c is related to the adsorption energy. To calculate V_m , a plot of $P/V(P_0-P)$ vs. P/P_0 is constructed such that its slope is $(c-1)/(V_m c)$ and its intercept is $1/V_m c$ [91].

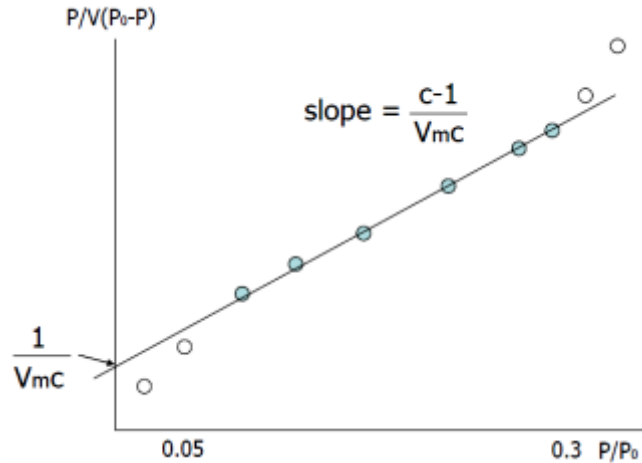


Figure 3.17 BET plot to evaluate V_m [91]

V_m is used in evaluating the monolayer's volume, the number of molecules occupying the monolayer, and multiplying this by the surface area occupied by each molecule yields the total surface area of the surface. Though the linear part of the plot is in the range of 0.05-0.30 P/P_0 , it is enough to enable V_m evaluation [87-88, 90].

It is important to note that although the BET model explained isotherms II and IV, it failed to explain isotherms I and III since there is no inflection point to linearize its range. Furthermore, the c values for both isotherms were found to be higher than normal, hence, studying such isotherms require other models [90].

3.6.2.2 de Boer t-plot Method

Interpretations of multilayers adsorbing on nonporous surfaces showed that there exists a direct relation between the thickness of the adsorbate molecules layers and their volume. This allowed thickness equations to be able to predict the adsorbate molecules volumes at different pressures. de Boer and Lippens made use of this observation and compared the isotherms of microporous materials with isotherms type II of the nonporous surfaces. By taking into account comparable c values of both the porous and nonporous surfaces, resembling similarity in the nature of the absorbent surface, the gas volume adsorbed on the porous surface is plotted against the statistical thickness of the reference nonporous material (at the same P/P_0 experimental values). This necessarily results in a deviation from linearity whenever pores are present as shown in Figure 3.18.

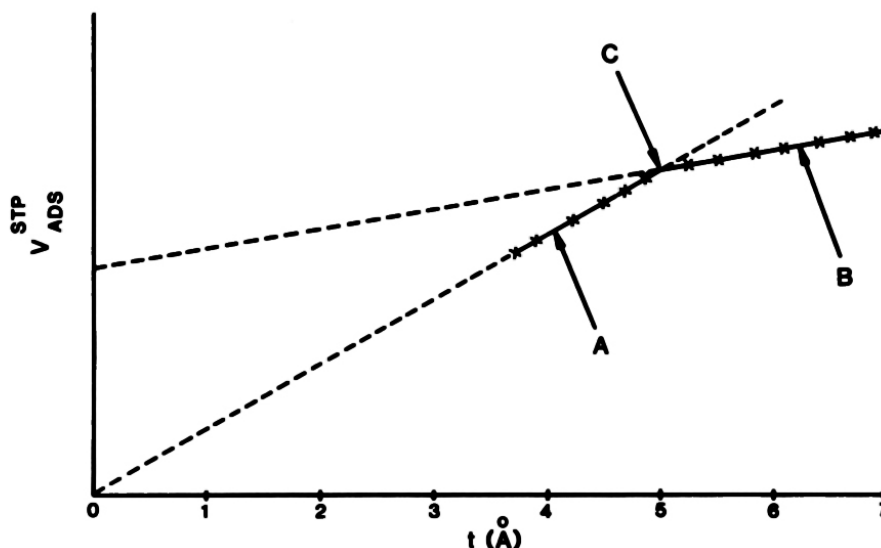


Figure 3.18 t-plot comparison between porous and nonporous surface [92]

In the absence of micropores, the extrapolation of the curve passes by the origin, yet, when micropores exist, the Y-intercept (i) of the linear parts of the curve (B) is used to calculate micropores volume (V_{MP}) by the following equation:

$$V_{MP} = i \times 0.001547 \text{ (cm}^3\text{)}$$

Furthermore, the slope of the (A) part of the t-plot could be used in calculating the external surface area (S_t) of the porous material, excluding the micropores surface areas, by the following equation¹:

$$S_t(\text{m}^2/\text{g}) = s \times 15.47$$

As for the slope of the (B) part of the t-plot, it could be used in calculating the surface area of the mesopores of the porous sample [92].

3.6.2.3 DFT Method

DFT method is a complex mathematical interpretation of the adsorbate-adsorbent interactions with geometrical consideration of the pores shapes and sizes. These interpretations create a real density profile of the adsorbate molecules as a function of temperature and pressure, from which the number of molecules adsorbed could be calculated. DFT method depends on several assumptions: (1) there exists attraction between the adsorbate molecules and the adsorbent surface (2) The organization of the adsorbate molecules on the surface maintains minimal overall free energy for the system, which is done by finding the molecules rearrangements with the highest probability distribution, which usually reflects minimal energy [93-94].

¹ The factors multiplied by both the intercept value and the slope value are derived from different equations.

As for the pore size distribution, the experimental isotherms are compared to hundred different isotherms, each with an individual pore dimension. In this respect, pore geometry could be analyzed, and pore size distribution compared to pore width is constructed [93-94].

There are other different interpretation models, and each can provide a piece of information about samples porosity (if any), surface areas, and can even evaluate samples adhesion property. Using this, membranes morphology and porosity can be analyzed, and their behavior in desalination and filtration applications can be interpreted.

4 Experimental

4.1 Materials Used

CA (avg. molecular weight 50,000 Da, 39.7 wt% acetyl content) purchased from Sigma-Aldrich Co. was used as a polymer matrix. Acetone (density 0.791 g/mL at 25°C, purity \geq 99.8%) purchased from Sigma-Aldrich Co. was used as a solvent. Deionized water was used as a non-solvent. Multi-walled carbon nanotubes (MWCNTs) Baytubes® C150P (C-purity \geq 95 wt%, inner diameter of \sim 4 nm, outer diameter of \sim 13 nm, and length $>$ 1 μ m) provided by Bayer Material Science AG. were used as nanofillers. H₂SO₄ (purity = 99.999%) purchased from Sigma-Aldrich Co. and HNO₃ (purity = 69%) purchased from Patel Group, India were used in oxidation purification of the CNTs. Sodium Chloride (molecular weight 58.44 g/mol, density 2.165 g/mL at 25°C, purity \geq 99.5%) purchased from Sigma-Aldrich Co. was used in desalination measurements. Sodium Hydroxide (molecular weight 40.00 g/mol, density 2.130 g/mL at 25°C, purity \geq 98%) purchased from Sigma-Aldrich Co. was used in the neutralization step of CNTs functionalization. Silver Nitrate (molecular weight 169.88 g/mol, density 4.35 g/mL at 25°C, purity \geq 99.8%) purchased from Sigma-Aldrich Co. was used in salt retention measurements.

4.2 Stock Solutions Preparation

4.2.1 CA Stock Solution

1. X grams of CA powder were dissolved in Y ml of acetone, X and Y determined according to the wt% required. A Z ml of deionized water was added for solutions containing non-solvent, Z determined according to the wt% of non-solvent required;
2. The mixture was left overnight under continuous stirring until the CA completely dissolved forming a clear homogenous solution;
3. The solution was then sonicated for 15 minutes and then left to rest so that all trapped air bubbles (resulting from sonication) are released. This typically required between 1 and 2 hours.

4.2.2 CA Stock Solution with Pristine (non-functionalized) Carbon Nanotubes (pNTs)

1. X grams of CA powder were dissolved in Y ml of acetone, X and Y determined according to the wt% required. L grams of pNTs were added, L determined according to the wt% of pristine CNTs needed. A Z ml of deionized water was added for solutions containing non-solvent, Z determined according to the wt% of non-solvent required;
2. The mixture was left overnight under continuous stirring until CA completely dissolved forming a clear homogenous solution;
3. The solution was then sonicated for 2 hours in order to ensure complete dispersion of the pNTs, then left to rest so that all trapped air bubbles (resulting from sonication) are released. This typically required between 1 and 2 hours

4.2.3 CA Stock Solution with Functionalized CNTs (fNTs)

1. 15 grams of CA powder were dissolved in Y ml of acetone determined according to the wt% required;
2. The mixture was left overnight under continuous stirring until CA completely dissolved forming a clear homogenous solution;
3. L grams of fNTs were dispersed in 20 ml deionized water (L determined according to the wt% of functionalized CNTs needed) and divided into 4 equal portions. Each portion was sonicated for 1 minute before adding it to the CA stock solution. After the addition of each portion to the stock solution, vigorous stirring of the mixture was carried out for a few seconds. The 4 portions were thus added sequentially to the CA stock. This ensured proper fNTs dispersion in the CA stock solution;
4. The mixture was then sonicated for 2 minutes, then left to rest overnight so that all trapped air bubbles (resulting from sonication) are released.

The CA and H₂O contents (15 wt% and 20 wt% respectively) were fixed in the nanocomposites preparation.

4.3 Methods and Instrumentation

4.3.1 Functionalization of Carbon Nanotubes

MWCNTs functionalization was carried out as described in the literature [71]:

1. 12 g of pristine MWNTs were added to 300 mL H₂SO₄ and 100 mL HNO₃ (3:1 by volume) in a round bottom flask.
2. The flask was immersed in an ultrasonic bath for 10 minutes to disperse the CNTs.
3. The flask was then mounted to a reflux with continuous water circulation to minimize acid evaporation. The top of the reflux was connected to a bottle filled with concentrated solution of NaOH.
4. The flask was immersed in a boiling water bath for 100 minutes, after which the flask was cooled down under tap water.
5. Filtering the CNTs was carried out using Whatman 0.2 μm pore size Teflon filter membranes placed in a microfiltration system connected to a pump.
6. The collected CNTs were washed with deionized water until the pH of the filtrate solution was neutral.
7. The collected CNTs were then washed with 50 mL of acetone to ensure the complete removal of water. Then they were placed in a desiccator under vacuum for 24 hours to complete drying.
8. The CNTs were then ground in a ceramic mortar, and the particles passed through a 180 μm pores sieve to have fine powdered CNTs.²

The functionalized CNTs were characterized by FTIR spectroscopy as well as SEM imaging.

² This step was added to the procedure obtained from the literature as it proved useful in achieving proper dispersion of the CNTs in the polymer matrix.

4.3.2 Membrane Casting

Membrane casting was carried out using an Elcometer 4040 Automatic Film Applicator using stock solutions prepared as specified in section 4.2 above, according to the following:

1. The stock CA solutions were poured into the casting equipment feed container;
2. The solution was then spread over a glass substrate by the equipment moving casting knife, adjusted in height to the needed membrane ICT;
3. The glass substrate with the cast solution was then immersed in a deionized water bath at the selected coagulation bath temperature for PI;
4. The resulting membranes were then stored in deionized water overnight to ensure complete solvent (acetone) removal.

For membranes where solvent evaporation was carried out, this took place either after solution casting and prior to PI, or post PI, as was necessary.



Figure 4.1 Elcometer 4040 Automatic Film Applicator

4.3.3 Sample Surface Area and Porosity Determination

Sample surface area and porosity determinations by nitrogen adsorption were carried out using a Micrometrics ASAP 2020 instrument. Membrane samples were prepared for analysis according to the following procedure:

1. A 5x5 cm² section of the sample membrane was dried for an hour in a furnace at 100°C, then left to cool down to room temperature in air;
2. The sample, cut into very small pieces and weighed, was inserted in the ASAP 2020 sample holder glass tube;
3. The tube was mounted in the ASAP 2020 equipment and degassed below 50 µmHg at 30°C for 30 min then heated (10 °C/min) to 80 °C for 360 min.

Adsorption/desorption isotherms were obtained by nitrogen adsorption at $-196\text{ }^{\circ}\text{C}$. Specific surface areas were calculated by the Brunauer-Emmett-Teller (BET) equation and the t-plot method which was also used to calculate micropore volumes. The pore size distribution was determined using DFT model.



Figure 4.2 Micromeritics ASAP 2020 instrument [95]

4.3.4 Infrared Analysis

Infrared spectra were obtained using a Thermo Scientific NICOLET 380 FTIR. Solid samples were prepared as KBr pellets, where 2 mg of the sample were mixed with approximately 200 mg of KBr spectroscopic grade. The mixture was then subjected to a pressure of about 1400 kPa in a hydraulic press.

4.3.5 Scanning Electron Microscopy

Sample images were obtained using a Leo Supra 55 (ZEISS) field emission electron microscope. SEM images were recorded without sample coating.

4.3.6 Liquid Test Cell

Permeation and salt retention determinations were carried out using a Sterlitech HP4750 Stirred Cell. The measurements were carried out as follows:

1. A 5 cm diameter membrane disc was placed within the test cell on a porous metal support, and the cell was filled with the feed solution;
2. Pressure was slowly increased to 24 bars using compressed nitrogen gas;

3. The sample was then given 5 to 15 minutes to have a steady liquid flow rate;
4. If after 15 minutes no liquid flow occurred, pressure was increased (with a rate of about 0.7 bars/minute) until a flow was obtained (the maximum pressure reached was 55 bars). For salt retention determinations, a 1000 ppm NaCl solution was used as feed. The amount of NaCl retained was determined by volumetric analysis determinations (titration with standardized silver nitrate) of the permeate solution.

Permeation and salt retention measurements were carried out in triplicates and the average obtained.

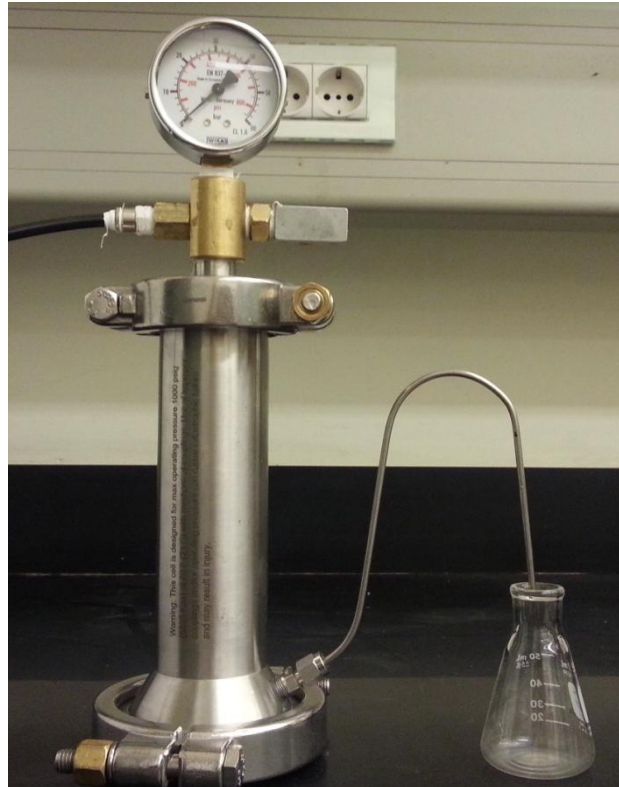


Figure 4.3 Sterlitech HP4750 Stirred Cell

4.4 Investigating Preparation Conditions

On developing CA membranes to use in filtration applications, it was important to investigate different preparation conditions on the CA membrane morphology before adding CNTs, so as to establish the best possible combinations that affect the presence/absence of macrovoids, their sizes, as well as the porosity of the surrounding matrix. This was important because macrovoids and matrix porosity play the major role in membranes' permeability and salt retention. The larger the voids, the higher the permeability; and the smaller the pores size of the surrounding matrix, the better the salt retention [51]. In this respect, a number of parameters were investigated, with the resulting membrane morphology characterized by SEM imaging. These parameters included:

- Membrane casting thickness;
- The temperature at which PI was carried out, “coagulation bath temperature”;
- CA content in the solvent;
- Time for solvent evaporation;
- Non-solvent (deionized water) content in the CA/acetone mixture;
- Content of carbon nanotubes, both pNTs and fNTs in the membrane

Once these different parameters were investigated, and a set of optimum values established, membrane morphology (surface area and porosity) and performance were established as a function of varying content of fNTs.

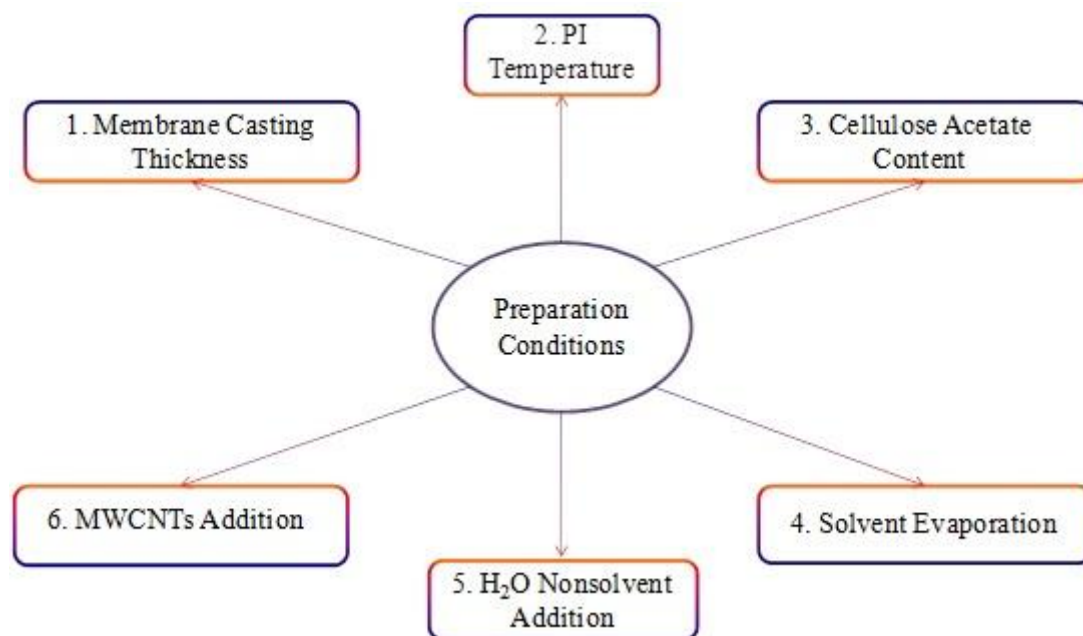


Figure 4.4 Different preparation conditions

4.4.1 Membrane Casting Thickness

Membrane casting thickness, which is the thickness of the cast solution adjusted using the casting knife, is a primary parameter in the development of membrane porosity and the formation of macrovoids [49]. Membrane casting thickness was found to change during the preparation process. ICT is the membrane thickness once it is cast prior to PI, while final casting thickness is the membrane thickness once PI and coagulation has been carried out. In this respect, the following trials were carried out:

A. *Effect of the membrane ICT on membrane morphology, using CA in acetone solvent:*

Two percentage weight values of CA in acetone were used: 15 wt% and 17 wt%. These values were chosen based on approximately similar values in the literature [28, 52]. For the 15 wt% CA in acetone the following ICT values were used:

- 600 μm

- 700 μm
 - 800 μm
- For the 17 wt% CA in acetone the following ICT values were used:
 - 500 μm
 - 600 μm
 - 800 μm

These values were selected to scan a range of thicknesses to understand their effect on morphology. PI was carried out at room temperature, and morphologies were investigated using SEM.

B. Effect of the membrane ICT on membrane morphology, using CA in acetone solvent together with a non-solvent (deionized water):

Two sets of compositions were used: 15 wt% CA in acetone with 5% non-solvent, and 17 wt% with 10% non-solvent. These values were chosen also to scan a range of thicknesses to understand their effect on morphology.

- For the 15 wt% CA in acetone with 5% non-solvent the following ICT values were used:
 - 300 μm
 - 400 μm
 - 500 μm
 - 600 μm
- For the 17 wt% CA in acetone with 10% non-solvent the following ICT values were used:
 - 700 μm
 - 800 μm

PI was carried out at room temperature, and morphologies were investigated using SEM.

C. Effect of the membrane ICT on membrane final casting thickness:

17 wt% CA in acetone were cast with a wide range of ICT values in order to check the linearity of the variation of ICT with the final membrane thickness. ICT values used were:

- 180 μm
- 500 μm
- 600 μm
- 700 μm
- 800 μm
- 1000 μm

The corresponding final thickness for each membrane after PI was measured using SEM, and a plot of ICT vs. final thickness was constructed. PI was carried out at room temperature.

4.4.2 Coagulation Bath Temperature (CBT) (PI Temperature)

CBT was investigated using two different contents of CA, 14 wt%, and 17 wt%. Membranes were prepared at the same ICT of 1000 μm , at room temperature and 40°C. SEM imaging was used to compare the final thicknesses and macrovoids sizes for the resulting membranes.

4.4.3 CA Content

Different CA contents of 13, 15, and 17 wt% in acetone were investigated for effect on membrane morphology and reproducibility:

- 13 wt% CA was cast at 1000 μm and 1200 μm ;
- 15 wt% CA was cast at 800 μm ;
- 17 wt% CA was cast at 800 μm .

These values are chosen based on similar values in the literature [21, 25, 28]. PI was carried out at room temperature, and morphologies were investigated using SEM.

4.4.4 Solvent Evaporation

Solvent evaporation is exposing the cast solution to air for some time, resulting in some of its solvent evaporating, and is used for decreasing pore sizes throughout the membranes. Two different sets of trials were carried out for investigating the effect of time of solvent evaporation on membrane morphology:

A. Incomplete PI with post-PI solvent evaporation:

Incomplete PI with post-PI solvent evaporation for different timings were carried out. 17 wt% CA in acetone was used as in the literature [25]. Typically, PI takes 7.5 minutes to complete. In this respect, two membranes were prepared as follows:

- PI for 5.5 minutes, followed by solvent evaporation for 3.5 minutes;
- PI for 2.5 minutes, followed by solvent evaporation for 3.5 minutes.

ICT was 1000 μm for both membranes and PI was carried out at room temperature. Morphologies were investigated using SEM.

B. Initial Solvent Evaporation (ISE):

ISE entails allowing the acetone solvent to evaporate after the membrane is cast and prior to coagulation by PI. In this respect, membranes were prepared as follows:

- 17 wt% CA in acetone was used for a membrane for which PI was carried out at room temperature for 7.5 minutes;
- 17 wt% CA in acetone was used for a second membrane which was subjected to ISE 60 seconds, followed by PI at room temperature for 7.5 minutes;
- 13 wt% CA in acetone was used for a membrane which was subjected to ISE for 30 seconds, followed by PI at room temperature for 7.5 minutes;
- 13 wt% CA in acetone was used for another membrane which was subjected to ISE for 60 seconds, followed by PI at room temperature for 7.5 minutes.

ICT was 1000 μm for both membranes, and morphologies were investigated using SEM. CA, as well as ISE values were used similar to the values used in the literature [25].

4.4.5 Addition of H₂O (Non-Solvent)

The addition of a non-solvent (deionized water) to the CA/acetone solution used for membrane casting affects membrane final thickness and morphology [52]. In this respect, the following membranes were prepared:

- 17 wt% CA in acetone was used for a set of membranes of ICT of 700 μm , and the following contents of deionized water as non-solvent:
 - 0 wt%
 - 10 wt%
 - 15 wt%
 - 20 wt%
 - 25 wt%
- 15 wt% CA in acetone was used for a set of membranes of ICT of 300 μm , and the following contents of deionized water as non-solvent:
 - 5 wt%
 - 20 wt%
- 14 wt% CA in acetone was used for a set of membranes of ICT of 1000 μm , and the following contents of deionized water as non-solvent:
 - 0 wt%
 - 5 wt%
 - 20 wt%

These different values of CA content, ICT, and non-solvent content were selected so as to develop a clear idea on the effect of non-solvent addition on macrovoids formation regardless of the CA content used. For all membranes, PI was carried out at room temperature, and morphologies investigated using SEM.

4.4.6 Addition of CNTs

The effect of the addition of pristine (non-functionalized) CNTs on the morphology of the membranes was investigated in terms of membrane compaction, and pNTs dispersion within the polymer matrix. In this regard, the following trials were carried out:

A. *Effect of presence of pNTs on membrane morphology:*

Two values of CA wt% in acetone were used, with membrane ICT of 1000 μm and different contents of pNTs, as follows:

- 17 wt% CA in acetone with:
 - 0 wt% pNTs
 - 0.5wt% pNTs
 - 1 wt% pNTs

- 13wt% CA in acetone with:
 - 0 wt% pNTs
 - 0.5wt% pNTs

These values are based on similar CNTs contents used with other polymer matrices in the literature [39]. PI was carried out at room temperature and morphologies were investigated using SEM.

B. *Effect of the content of fNTs on their dispersion within the CA membranes:*

The effect of the addition of fNTs on the morphology of membranes was investigated in terms of membrane compaction, and fNTs dispersion within the polymer matrix. In this respect, 15 wt% CA in acetone was used with 20 wt% water (non-solvent) and a membrane ICT of 400 μm with different contents of fNTs as follows:

- 0 wt% fNTs
- 0.0005 wt% fNTs
- 0.005 wt% fNTs
- 0.01 wt% fNTs

Significantly low fNTs content values were selected in order to minimize CNT agglomeration within the membrane matrix, and to ensure optimal dispersion. PI was carried out at room temperature, and morphologies were investigated using SEM.

4.5 Optimal Preparation Conditions Samples

Based on the findings of the variation of the six parameters membrane samples were prepared according to the following:

- Final membrane thickness = $100 \pm 10 \mu\text{m}$
- Coagulation Bath Temperature = room temperature
- 15% CA content in acetone
- No solvent evaporation
- 20% water (non-solvent) content
- 0, 0.0005, 0.005, 0.01 %wt fNTs
- For the 0 %wt fNTs, two samples were prepared: one with an ICT of $400 \mu\text{m}$, and a final thickness of $120 \pm 10 \mu\text{m}$; and a second with an ICT of $350 \mu\text{m}$ and a final thickness of $100 \pm 10 \mu\text{m}$. Each of these samples represented a “blank”.

These samples' morphologies were characterized by SEM, as well as nitrogen adsorption for surface area and porosity determination, together with solution permeation and salt retention performance. All measurements and determinations were carried out in triplicates and the averages obtained.

5 Results and Discussion

5.1 Effect of Preparation Conditions on Membranes Morphology

Different preparation conditions have different effects on membrane morphology. Yet, for filtration applications, the asymmetric membrane needs to have a dense top layer to screen out salts, macrovoids to enhance permeation rate, and a porous structure throughout the rest of the membrane [23, 26, 28, 30, 38, 51]. An illustrative figure for such morphology is displayed in Figure 5.1.

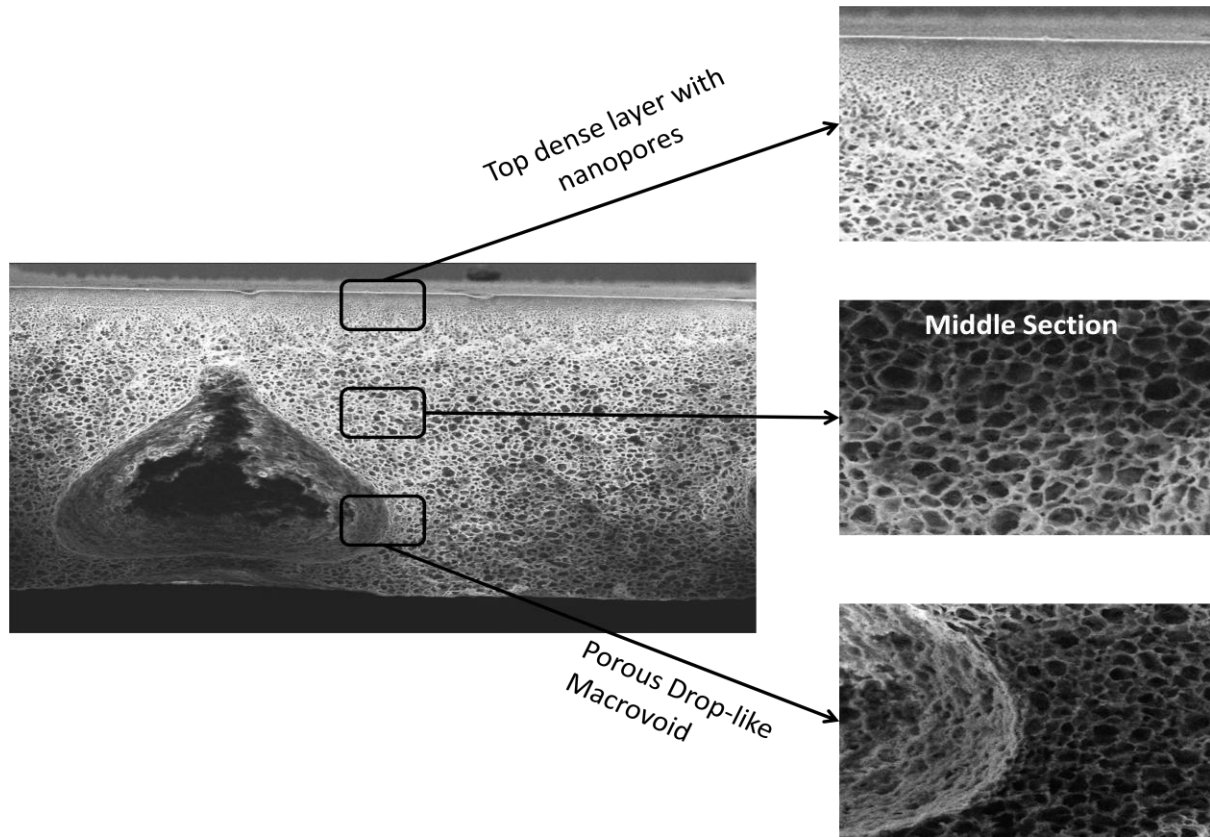


Figure 5.1 SEM of an asymmetric membrane

In this chapter, the results of different preparation conditions and their combinations on membrane morphology and performance are first reported followed by results and interpretation for membrane characterization and performance for those membranes prepared based on the optimal preparation conditions results. The conditions investigated were:

- Membrane Casting thickness
- Coagulation Bath Temperature
- CA content
- Solvent Evaporation
- Addition of H₂O (additive) in the CA/Acetone Stock Solution
- Addition of MWCNTs

5.1.1 Membrane Casting Thickness

A. Effect of the membrane ICT on membrane morphology, using CA in acetone solvent:

Membrane thickness variation was found to have an effect on membrane morphology: thicker membranes exhibit larger well-developed macrovoids. It was also found that below a certain critical thickness (whose values depends on the CA and non-solvent content), macrovoids didn't develop. Figure 5.2, 5.3, 5.4, and 5.5 show the effect of casting thickness on macrovoid development. In Figures 5.2 and 5.3, membranes were prepared with 17 wt% CA and 15wt% respectively. PI was carried out for both experiments at room temperature. The Figures show that the decrease in membrane final thickness reduced the size and numbers of macrovoids. Figure 5.2 (a) shows a membrane thickness small enough to be devoid of macrovoids.

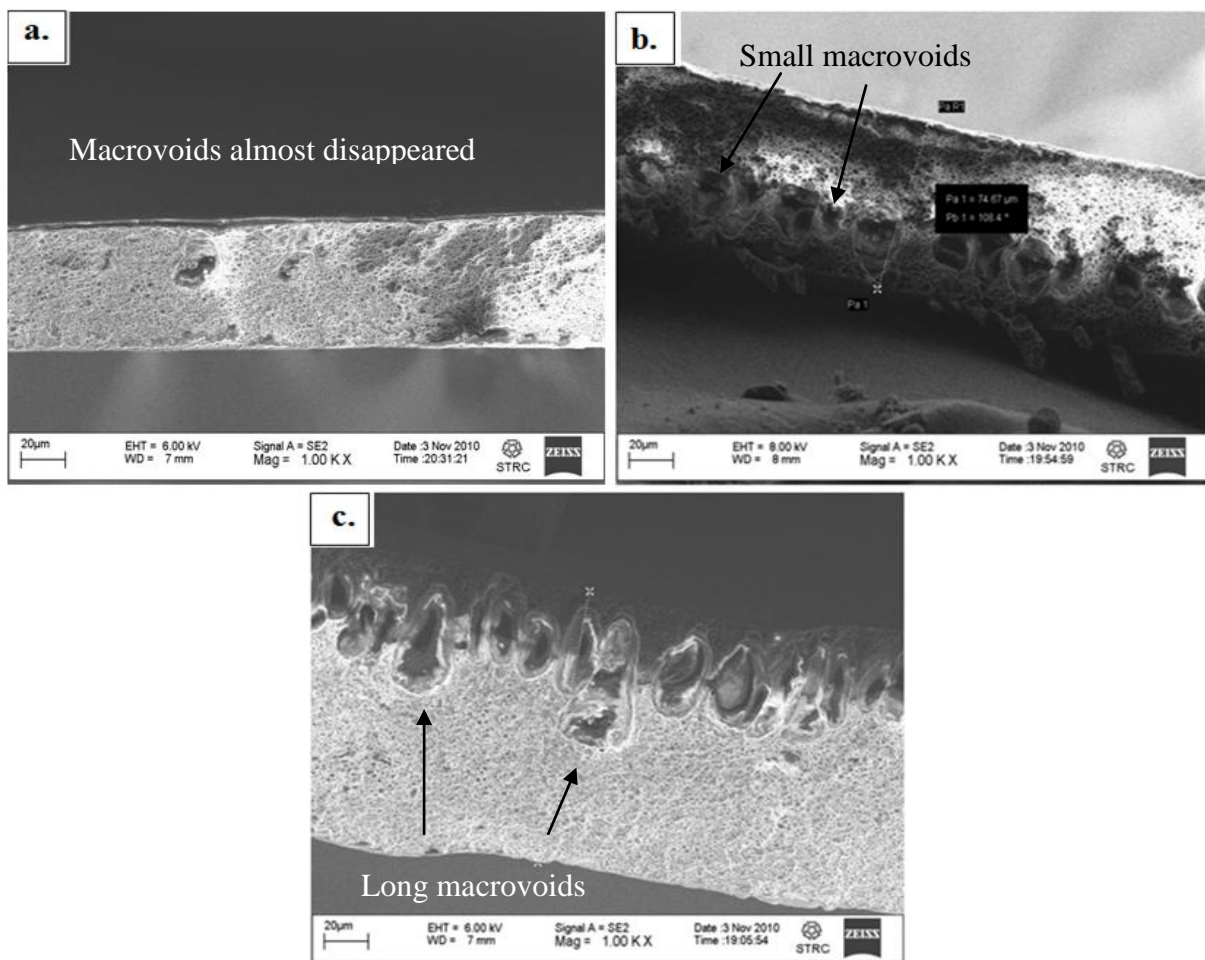


Figure 5.2 SEM of 17 wt% CA membranes, PI carried out at room temperature: (a) ICT = 500 μm, final thickness = ~55 μm, (b) ICT = 600 μm, final thickness = ~75 μm, (c) ICT = 800 μm, final thickness = ~122 μm

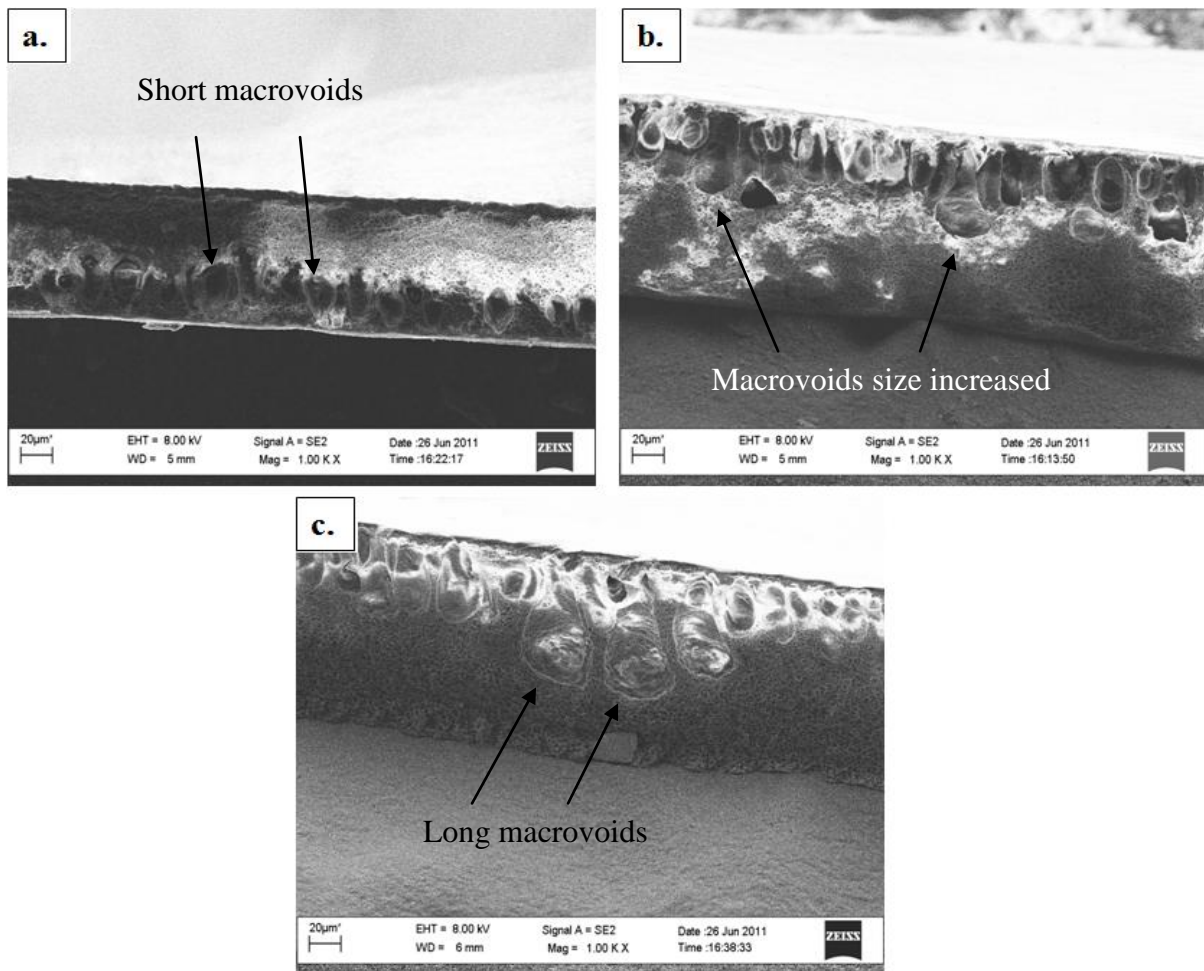


Figure 5.3 SEM of 15 wt% CA membranes, PI carried out at room temperature: (a) ICT = 600 μm , final thickness = $\sim 79 \mu\text{m}$, (b) ICT = 700 μm , final thickness = $\sim 114 \mu\text{m}$, (c) ICT = 800 μm , final thickness = $\sim 122 \mu\text{m}$

B. Effect of the membrane ICT on membrane morphology, using CA in acetone solvent together with a non-solvent (deionized water):

In Figure 5.4 and 5.5, membranes were prepared with the addition of water as non-solvent content expected to enhance macrovoids development³. The effect of casting thickness was investigated on the macrovoids formation and membrane shrinkage. Figure 5.4 shows typical membrane morphology for a sample with 17 wt% CA content, 10 wt% non-solvent, and PI carried out at room temperature. Figure 5.5 shows typical membrane morphology for a sample with 15 wt% CA content, 5 wt% addition of non-solvent, and PI was carried out room temperature. Both Figures 5.4 and 5.5 show the significance of casting thickness on macrovoids formation. In Figure 5.4 (a) the macrovoids shape, size, and depth within the membrane cross section changed when the membrane casting thickness was increased by $\sim 100 \mu\text{m}$ only as compared to Figure 5.4 (b). In Figure 5.5 (a) and (b), membrane thickness

³ The addition of water as non-solvent on membrane morphology will be discussed in details in section 5.1.5, while here, the ICT effect on the final thickness is the main focus

was not enough to allow the development of macrovoids. As for Figure 5.5 (c) and (d), the increase in casting thickness allowed macrovoids formation.

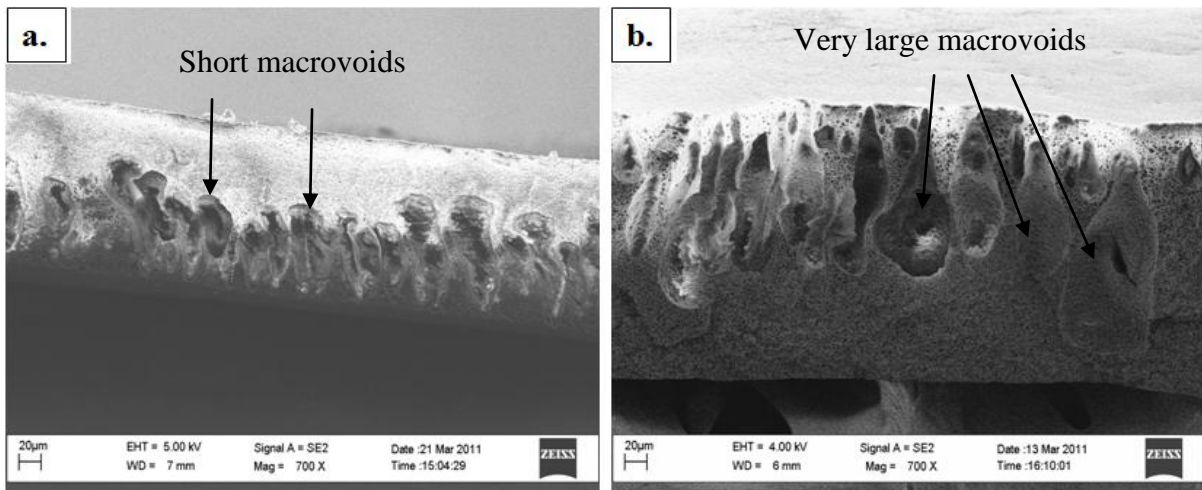


Figure 5.4 SEM of 17 wt% CA + 10 wt% H₂O membranes, PI at room temperature: (a) ICT = 700 μm, final thickness = ~137 μm, (b) ICT = 800 μm, final thickness = ~226 μm

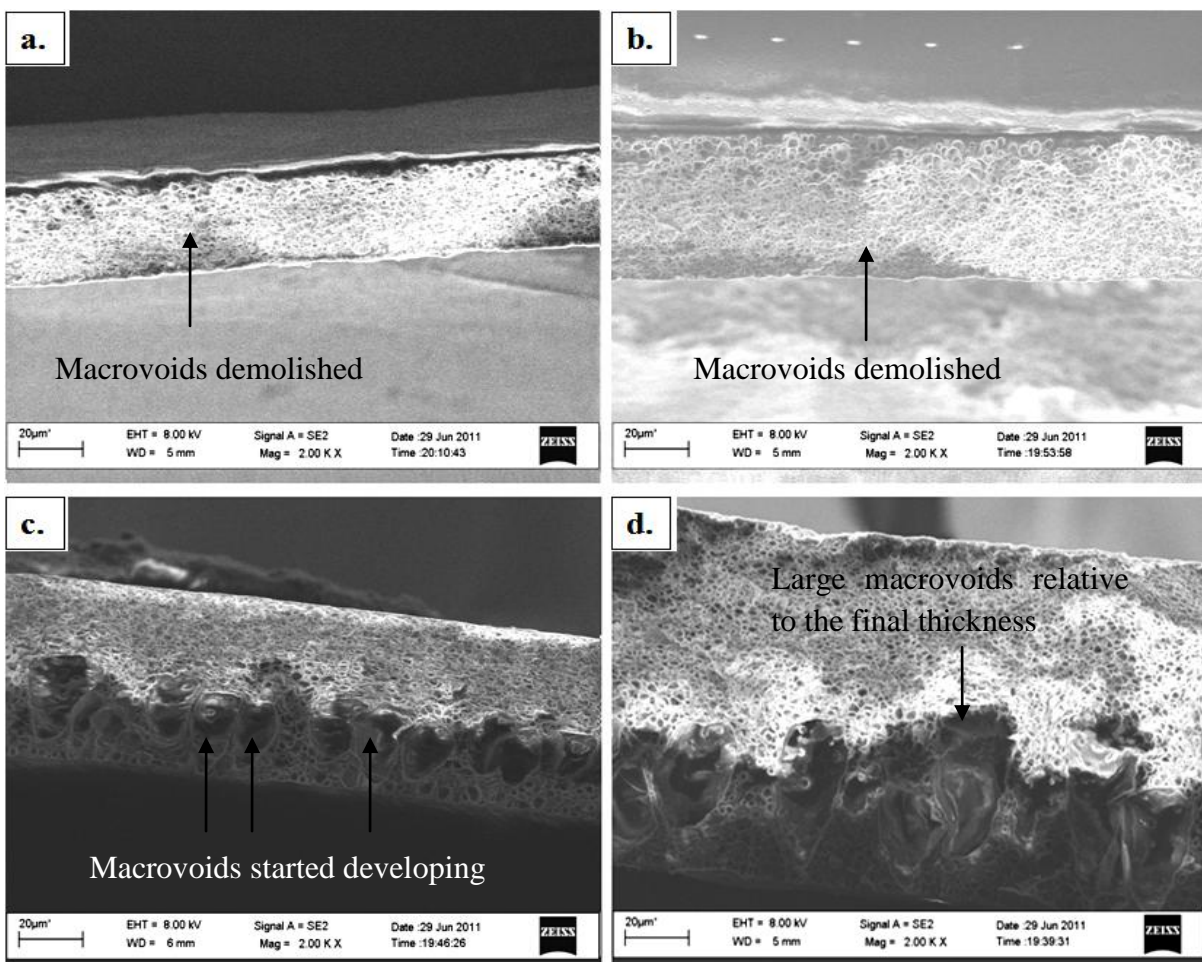


Figure 5.5 SEM of 15 wt% CA + 5 wt% H₂O membranes, PI at room temperature: (a) ICT = 300 μm, final thickness = ~30 μm, (b) ICT = 400 μm, final thickness = ~44 μm, (c) ICT = 500 μm, final thickness = ~55.4 μm, (d) ICT = 600 μm, final thickness = ~110 μm

From these data, the following general trend could be established:

- CA content variation did not lead to a significant variation in membrane final thickness relative to ICT for the 15 wt% and 17 wt% CA membranes.
- The presence of non-solvent did reduce the decrease in the membrane thickness as a result of PI with a noticeable enhancement effect on macrovoid formation.
- The maximum critical thickness for macrovoids development seemed to be about 50 μm , and was dependent on CA and nonsolvent contents as supported in the literature [49, 52].

Table 5.1 Macrovoids numbers and dimensions relative to CA content, non-solvent content, and membrane thickness

17 wt% CA membrane							
0 wt% H ₂ O				10 wt% H ₂ O			
ICT (μm)	FT (μm)	Macrovoids number	Macrovoids dimensions (length (μm) X width (μm))	ICT (μm)	FT (μm)	Macrovoids number	Macrovoids dimensions (length (μm) X width (μm))
500	~55	1	28 X 20	700	~137	15	50 X 30
600	~75	6	19 X 18	800	~226	10	140 X 68
		6	24 X 20			7	30 X 20
800	~122	2	52 X 30				
		12	28 X 18				

15 wt% CA membrane							
0 wt% H ₂ O				5 wt% H ₂ O			
ICT (μm)	FT (μm)	Macrovoids number	Macrovoids dimensions (length (μm) X width (μm))	ICT (μm)	FT (μm)	Macrovoids number	Macrovoids dimensions (length (μm) X width (μm))
600	~79	12	32 X 20	300	~30	0	0
700	~114	3	52 X 24	400	~44	0	0
		16	34 X 18	500	~55.4	12	30 X 16
800	~122	3	80 X 40	600	~110	8	48 X 20
		14	36 X 20				

This behavior can be explained from understanding the demixing process occurring for the thick and thin membranes. Typically when the combination of preparation conditions are selected to form instantaneous demixing with macrovoids formation, as elaborated in section 3.3.2, the polymer rich phase gives up its solvent into the polymer lean phase, resulting in nucleation that continues to grow as demixing continues (instantaneous demixing). On the other hand, a delayed demixing occurs at the interface of the nuclei since the non-solvent becomes filled with the solvent. This expands the non-solvent droplets size concurrently with

the solidification of the polymer rich phase because the polymer is being depleted from its solvent. For lower ICT, the solvent that typically increases voids sizes wouldn't have enough time to expand the size of the non-solvent droplets by delaying the demixing process at the nucleus borders. This would consequently affect the macrovoids size in relation to the ICT. Below the critical thickness, the membrane is thin enough for instantaneous demixing to prevail throughout the membrane.

C. Effect of the membrane ICT on membrane final casting thickness:

Investigating the linearity between ICT and the corresponding final thickness (FT) was done for the 17 wt% CA membrane with ICT range of 180-1000 μm . The relation between the ICT and the FT is presented in Figure 5.6. It was non-linear showing a rising increase in FT with ICT increase.

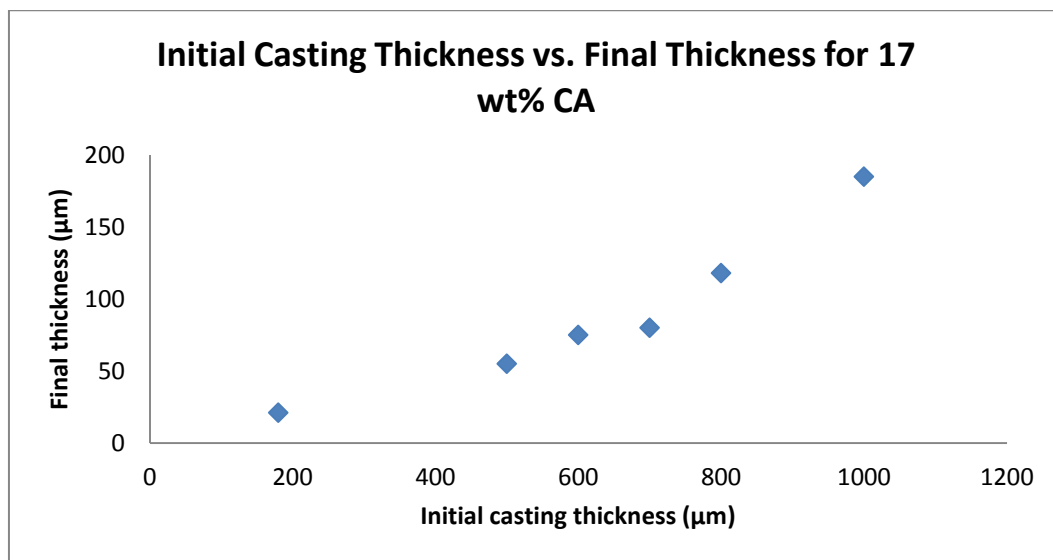


Figure 5.6 A plot showing the non-linear change in final thickness of 17 wt% CA membranes with the increase in ICT. PI was done at room temperature

The change in the final thickness as ICT changes is expected since during PI, the cast CA/acetone solution exchanges the acetone with water as non-solvent, and the CA starts shrinking until the polymer rich layer is depleted from the solvent and CA precipitates. The variation between ICT and FT was found to be non-linear as displayed in the representation in Figure 5.6. This could be explained by the fact that as the membrane final thickness increase, the macrovoids formation is enhanced, and their shape changes, where the thicker the membrane, the longer drop-like the macrovoids become. Thus, it is fair to assume that macrovoids formation affects the final thickness of the membrane in such way that it takes smaller than predicted ICTs to reach a desired final thickness.

5.1.2 Coagulation Bath Temperature (CBT)

The results of CBT effect on membrane morphology using 17 wt% and 14 wt% CA contents are displayed in Figures 5.7 and 5.8 respectively. In Figure 5.7, two 17 wt% CA

membranes were cast at the same ICT (1000 μm), and at two different CBT temperatures (room temperature and 40°C). Figure 5.7 (a) shows the overall membrane morphology with different macrovoid sizes that ranged from small to large. The large ones are distributed away from one another, separated by the small ones. Figure 5.7 (b) shows the top layer (high magnification) with the macrovoids necks developed at about 10 μm from membrane surface. Figure 5.7 (c) shows the 17 wt% membrane prepared using PI at 40°C, where the macrovoid sizes changed, producing medium size macrovoids more closely packed together. Figure 5.7 (d) shows the macrovoids necks developed at a much smaller distance (<1 μm) from the membrane surface.

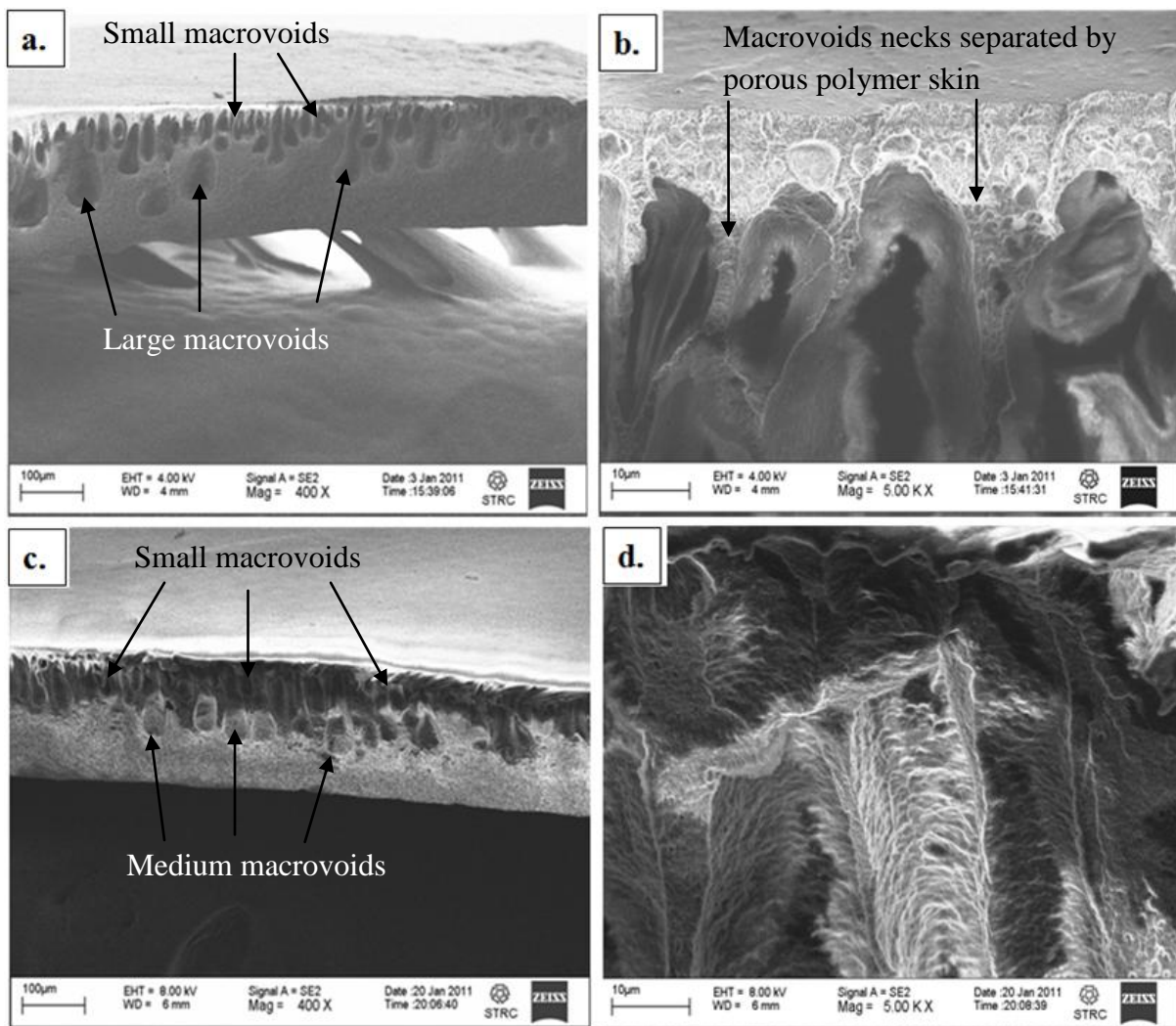


Figure 5.7 SEM of 17% CA content, ICT = 1000 μm : (a) FT = ~180 μm , PI at room temperature, (b) Voids necks at high magnification for PI at room temperature (c) FT = ~172 μm , PI at 40°C, (d) Voids necks at high magnification for PI at 40°C

Membranes obtained from 14 wt% CA, cast at the same ICT (1000 μm), and at the same CBT temperatures (room temperature and 40°C) showed a different trend for the sizes and shapes of the macrovoids. Figure 5.8 (a) shows large macrovoids separated from each other by smaller macrovoids (similar to Figure 5.7 (a)), yet, the voids necks (Figure 5.8 (b)) are at a shorter distance (about 3 μm) from the membrane surface. For PI at 40°C, mostly medium

macrovoids developed, with occasional large ones (Figure 5.8 (c)). The macrovoids necks were approximately located close to the membrane surface (about 3 μm) as in the room temperature PI 14 wt% CA samples (Figure 5.8 (d)).

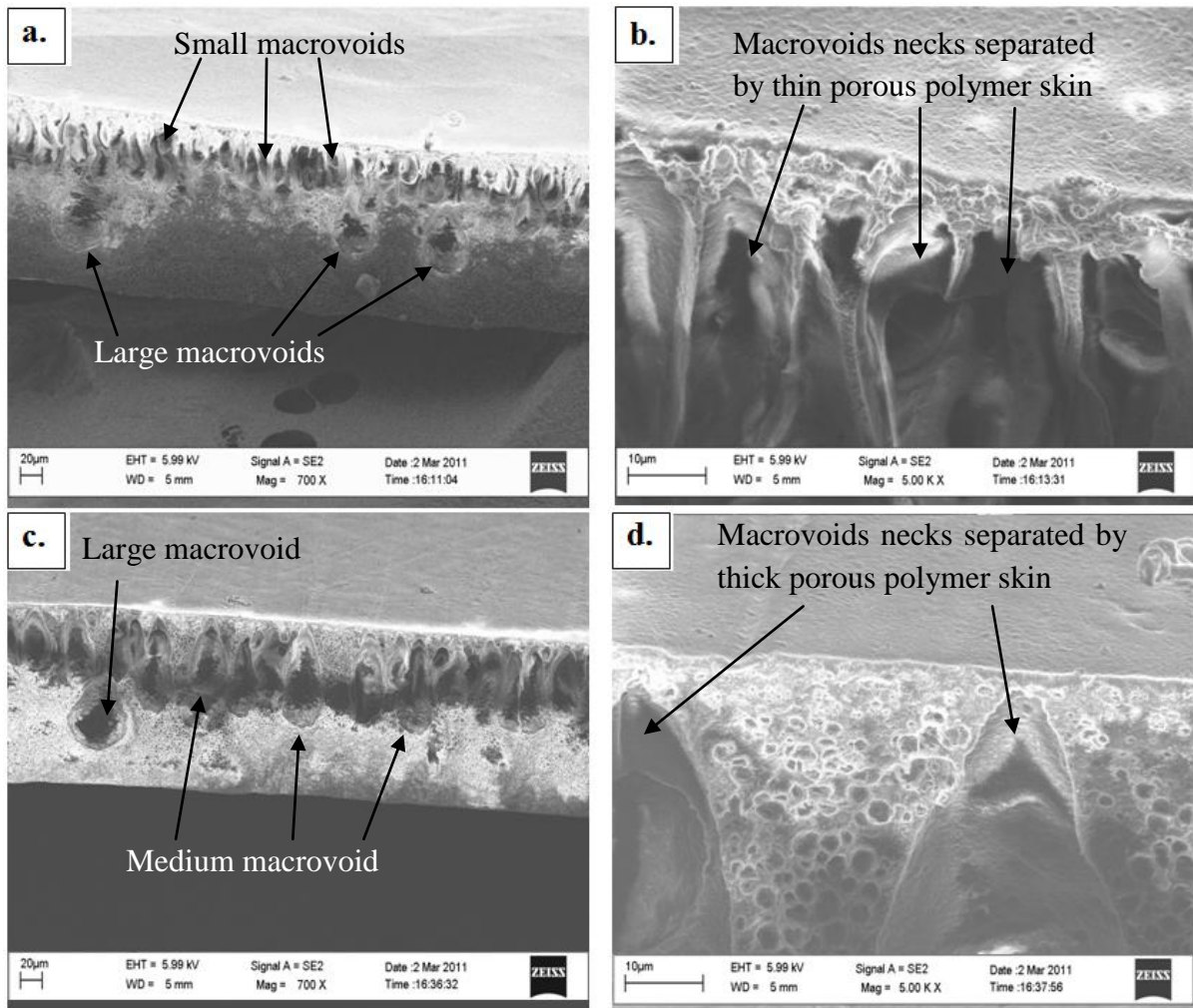


Figure 5.8 SEM of 14% CA content, ICT = 1000 μm : (a) FT = $\sim 138 \mu\text{m}$, PI at room temperature, (b) Voids necks at a high magnification, PI at room temperature, (c) FT = $\sim 138 \mu\text{m}$, PI at 40°C, (d) Voids necks at a high magnification, PI at 40°C

Table 5.2 Macrovoids numbers and dimensions relative to CA content and PI temperature

17 wt% CA membrane							
PI at room temperature				PI at 40°C			
ICT (μm)	FT (μm)	Macrovoids number	Macrovoids dimensions (length (μm) X width (μm))	ICT (μm)	FT (μm)	Macrovoids number	Macrovoids dimensions (length (μm) X width (μm))
1000	~180	7	140 X 100	1000	~172	8	120 X 40
		23	76 X 40			24	100 X 40

14 wt% CA membrane							
PI at room temperature				PI at 40°C			
ICT (μm)	FT (μm)	Macrovoids number	Macrovoids dimensions (length (μm) X width (μm))	ICT (μm)	FT (μm)	Macrovoids number	Macrovoids dimensions (length (μm) X width (μm))
1000	~138	3	60 X 40	1000	~138	1	55 X 50
		22	40 X 20			14	80 X 25

The results indicate that generally, higher PI temperature reduced the size distribution of macrovoids, allowing them to form close to the membrane surface, and increased the sizes of the small macrovoids formed. This latter effect seems to be somewhat impacted by the CA content, with the higher CA content membranes showing a more pronounced effect. Increasing the temperature leads to enhancing the demixing process, which would lead to rapid membrane shrinking and solidification, promoting the formation of macrovoids [28, 30]. For the higher CA content of 17 wt%, an increased coagulation temperature resulted in a decrease of the size of larger macrovoids. This decrease was compensated by an increase in the size of smaller macrovoids as displayed in Table 5.2. For the lower CA content of 14 wt%, the increase in the size of the smaller macrovoids at high coagulation temperature was more obvious. Though the overall number of the macrovoids (both small and large) for 14 wt% membranes prepared at 40°C is smaller than those prepared at room temperature, calculating their overall dimensions roughly (length X width X macrovoids number) shows that membranes prepared at 40°C have an overall macrovoids dimension of 30,750 μm² vs. only 24,800 μm² for macrovoids of membranes prepared at room temperature.

5.1.3 CA Content

Results of the 13 wt% CA membranes showed that reproducibility was found to be a major problem for these membranes where the same ICT at the same PI temperature produced different final thicknesses. Figures 5.9 and 5.10 show two samples prepared at the same temperature, one with ICT of 1200 μm, and the second with ICT of 1000 μm respectively. Figure 5.9 shows three different locations on the 1200 μm membrane with three

different final thicknesses, $\sim 173 \mu\text{m}$, $\sim 186 \mu\text{m}$, and $\sim 217 \mu\text{m}$. Figure 5.10 shows two different locations on the $1000 \mu\text{m}$ membrane with two different final thicknesses, $155 \mu\text{m}$ and $185 \mu\text{m}$. This is believed to be due to the low viscosity of the cast solution. When this is immersed in the coagulation bath, the lower viscosity leads to more intensive demixing process, probably due to the presence of high solvent content. This is believed to have led to a rippling effect during the formation of the macrovoids, leading to the variation in the thickness. Although this has not been reported in the literature, it seems to be an experimental artifact.

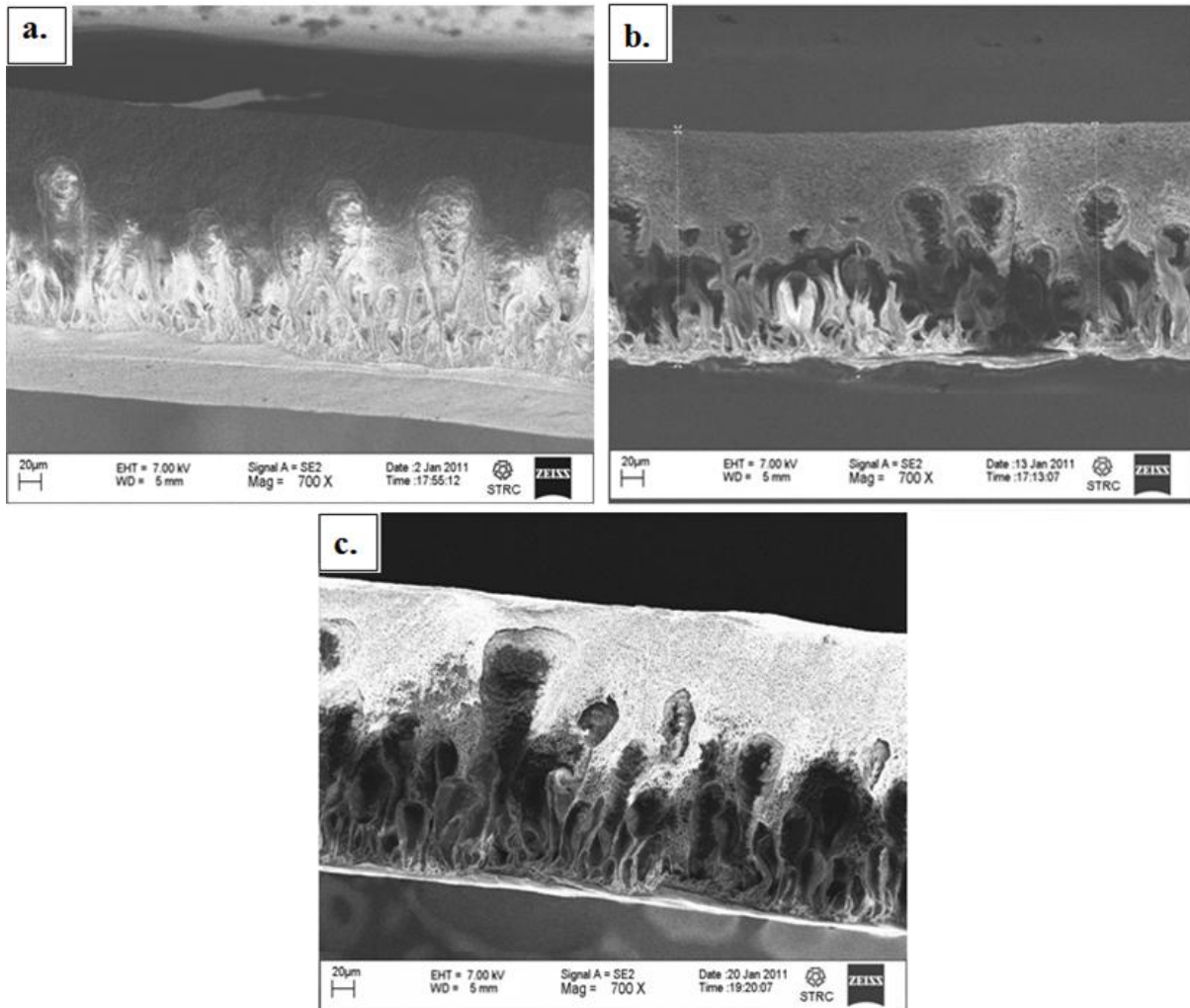


Figure 5.9 SEM of three 13 wt% CA membranes prepared with $ICT = 1200 \mu\text{m}$: (a) final thickness = $\sim 173 \mu\text{m}$, (b) final thickness = $\sim 186 \mu\text{m}$, (c) final thickness = $\sim 217 \mu\text{m}$

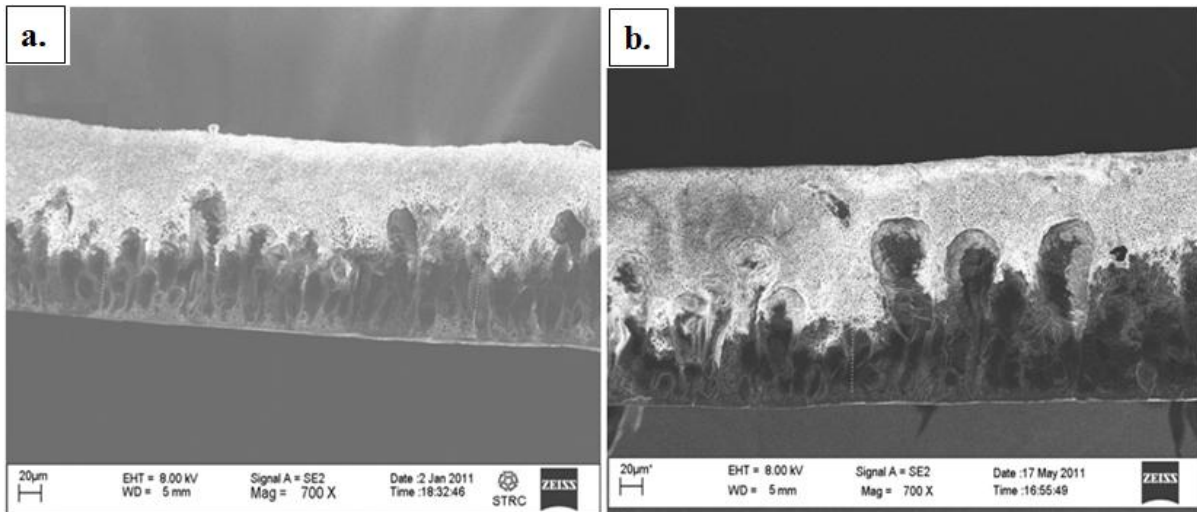


Figure 5.10 SEM of 13 wt% CA membranes, ICT = 1000 μm : (a) final thickness= \sim 155 μm , (b) final thickness= \sim 185 μm

17 wt% and 15 wt% CA content gave reproducible final thicknesses. Using the same ICT of 800 μm , the two membranes gave comparable final thicknesses of approximately 80 μm . Figure 5.11 shows the morphology of both. The change in size of the macrovoids could be easily spotted where the 17 wt% CA membrane (Figure 5.11 (a)) has smaller macrovoids than the 15 wt% CA membrane (Figure 5.11 (b))

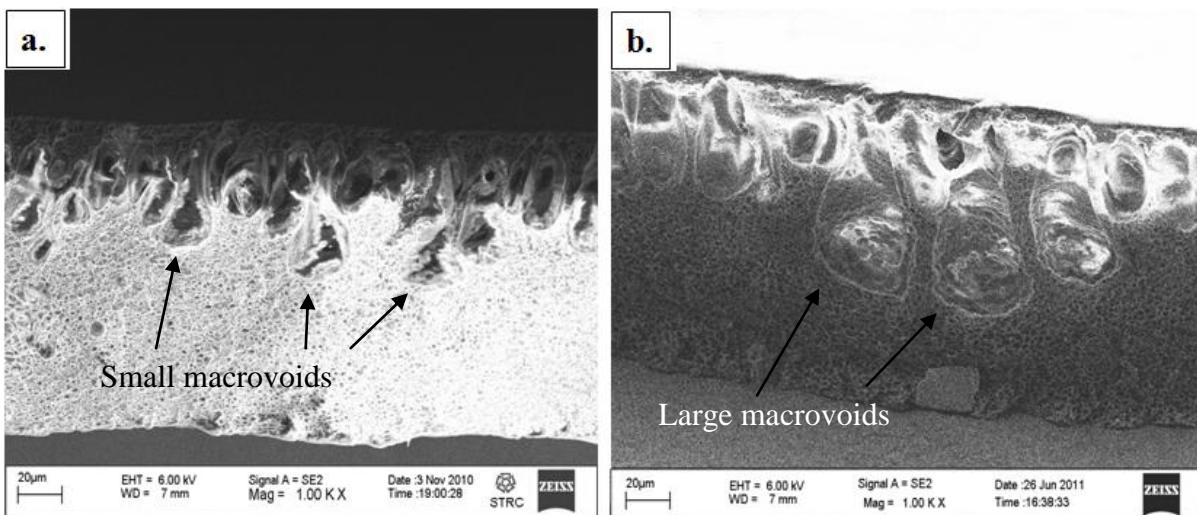


Figure 5.11 SEM of membranes prepared with PI at room temperature, ICT = 800 μm , final thickness of \sim 122 μm : (a) 17 wt% CA, (b) 15 wt% CA

Table 5.3 Macrovoids numbers and dimensions relative to CA content

Cellulose Acetate Content							
17 wt% CA				15 wt% CA			
ICT (µm)	FT (µm)	Macrovoids number	Macrovoids dimensions (length (µm) X width (µm))	ICT (µm)	FT (µm)	Macrovoids number	Macrovoids dimensions (length (µm) X width (µm))
800	~122	2	52 X 30	800	~122	3	80 X 40
		12	28 X 18			14	36 X 20

From Figure 5.11 and Table 5.3, it is clear that at the same final thickness, the smaller the CA content, the larger the size of the macrovoids. This is expected and matches the observations in the literature [51-52, 54]. At the same ICT, the low CA content is compensated by high solvent volume, and as earlier explained, the higher the solvent content, the more delayed the demixing process on the borders of the growing pores until they become macrovoids. This takes place at the same time as the rest of the membrane is shrinking and solidifying, thus creating macrovoids, as explained in details in section 3.3.2.

5.1.4 Solvent Evaporation

A. Incomplete PI with post-PI solvent evaporation:

Solvent evaporation prior to complete PI is not a usual method. Figure 5.12 clearly shows its effect on membranes morphologies and final thicknesses, for membranes with 17 wt% CA membranes, ICT = 1000 µm and PI at room temperature. A membrane prepared with complete PI for 7.5 min had a final thickness = ~180 µm, with the typical drop-like large macrovoids (Figure 5.12 (a)). Figure 5.12 (b) shows a membrane prepared with PI for 5.5 min, followed by solvent evaporation for 3.5 min. The final thickness of the membrane was reduced to be ~138 µm, while the shape of the macrovoids wasn't affected much in light of the final thickness of the membrane. Figure 5.12 (c) shows a membrane prepared with PI for 2.5 min, followed by solvent evaporation for 3.5 min. The final thickness was reduced to ~135 µm (which is very close to that of Figure 5.12 (b)), however, the shape and size of the macrovoids had a significant change: they shrunk into small macrovoids, with a disappearance of the large macrovoids.

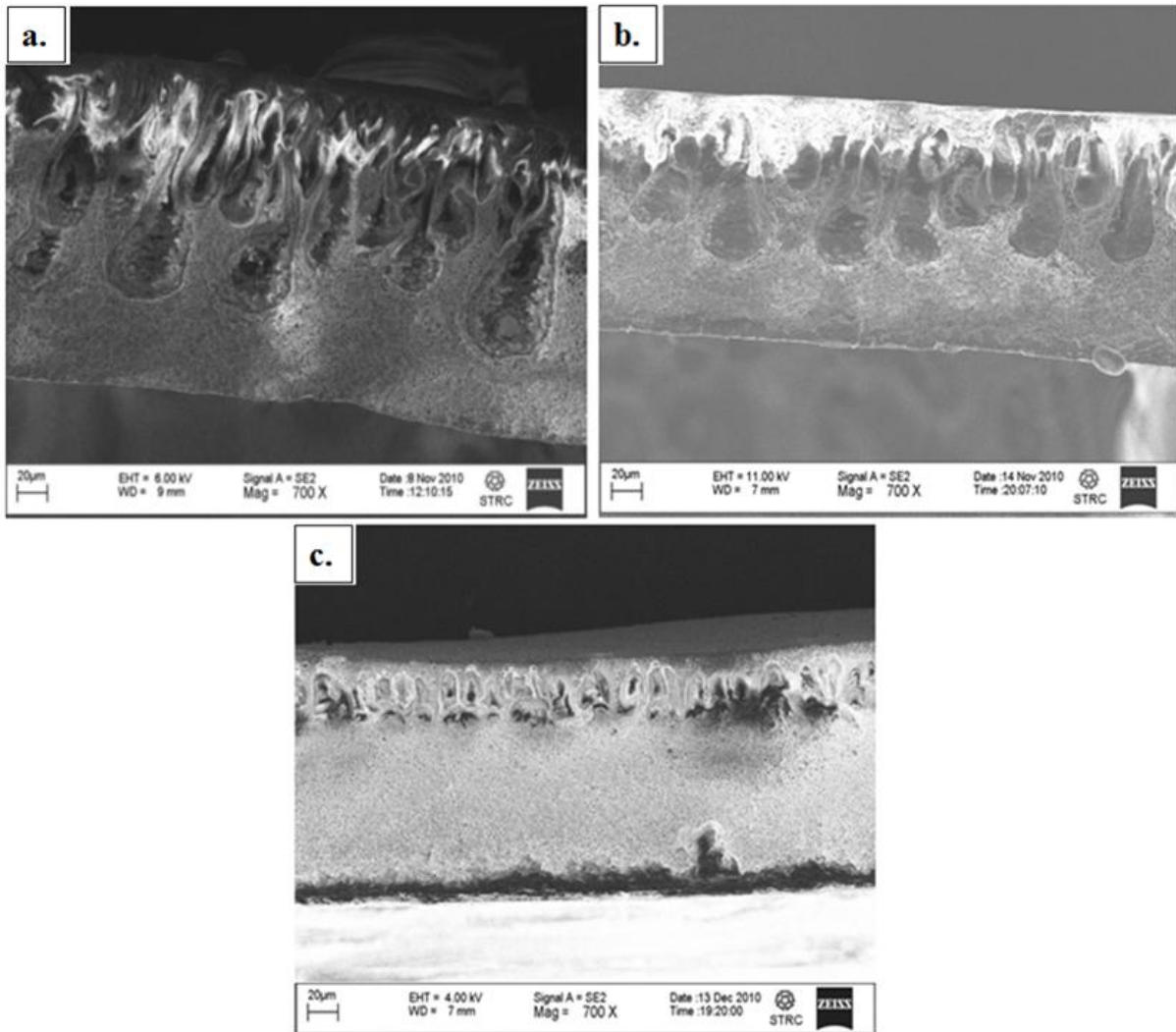


Figure 5.12 SEM of 17 wt% CA membranes: (a) complete PI for 7.5 min, final thickness = ~180 μm , (b) PI for 5.5 min, followed by solvent evaporation for 3.5 min, final thickness = ~138 μm , (c) PI for 2.5 min followed by solvent evaporation for 3.5 min, final thickness = ~135 μm

B. Initial Solvent Evaporation (ISE):

Figure 5.13 shows a comparison between two 17 wt% CA membranes, prepared with ICT of 1000 μm , and complete PI at room temperature for 7.5 minutes. The first membrane was prepared without ISE, while the second was subjected to 60 seconds ISE prior to PI. From the figure, the thickness of the latter membrane final thickness was half that of the former (180 μm vs. 77 μm) (Figure 5.13 (a) vs. Figure 5.13 (b)). At the same time, the macrovoid sizes changed significantly, where those subjected to ISE for 60 seconds were much smaller than the normally prepared (Figure 5.13 (b)).

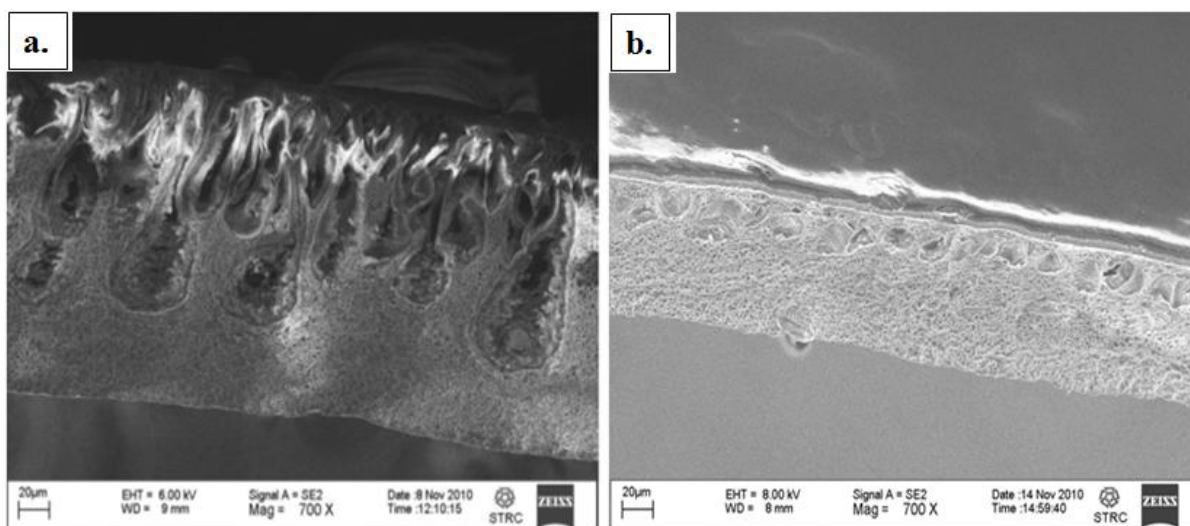


Figure 5.13 SEM of 17 wt% CA membranes, PI at room temperature for 7.5 minutes: (a) ISE = 0 sec, final thickness = ~180 µm, (b) ISE = 60 sec, final thickness = ~77 µm

Table 5.4 Macrovoids numbers and dimensions relative to solvent evaporation

17 wt% CA membrane				
post-PI solvent evaporation	ICT (µm)	FT (µm)	Macrovoids number	Macrovoids dimensions (length (µm) X width (µm))
after zero minutes	1000	~180	4	104 X 50
			10	40 X 26
after 3.5 minutes	1000	~138	5	98 X 42
			10	34 X 20
after 2.5 minutes	1000	~135	20	30 X 16

17 wt% CA membrane				
ISE	ICT (µm)	FT (µm)	Macrovoids number	Macrovoids dimensions (length (µm) X width (µm))
Zero seconds	1000	~180	4	104 X 50
			10	40 X 26
60 seconds	1000	~77	14	26 X 20

Figures 5.12 and 5.13, and Table 5.4 show that solvent evaporation, whether done before PI or after incomplete PI had a significant effect on macrovoids development and size, as well as on membrane final thickness. Solvent evaporation after incomplete PI was not recorded in the literature, while ISE is commonly used to condense the nascent top layer to enhance the membranes' retention ability [24, 32, 36]. However, none of the reported work in the literature had such a dramatic shrinkage in macrovoids. Going back to the solvent types used in the reported work, DMF, acetone mixed with dioxane, and acetone mixed with acetic acid were used, which are all less volatile than acetone alone. Moreover, different additives

were used to enhance pore formation and inorganic particles to produce the desired membrane morphology, leading to different results.

As for why macrovoid size was reduced because of solvent evaporation, as mentioned before, macrovoid formation requires enough solvent to fill in the developing nuclei filled with the non-solvent in the polymer lean phase, thus expanding the nuclei sizes and creating macrovoids. For solvent evaporation prior to complete PI, the solvent has not been completely exchanged with the non-solvent, and the polymer rich phase has not completely solidified. Thus, instead of filling in the non-solvent droplets, the solvent evaporates since the developing membrane has been removed from the coagulation bath, and PI process is interrupted, leading to smaller macrovoids for shorter PI times. For ISE for 60 seconds, acetone, being highly volatile solvent is thought to have evaporated with a quantity large enough that what was left in the cast solution wasn't enough to expand the macrovoids.

In an attempt to produce uniform membranes using 13 wt% CA content, ISE was carried out for such membrane. Figure 5.14 shows the morphology of two 13 wt% CA membranes prepared with ISE 30, and 60 seconds, ICT of 1000 μm , and PI at room temperature. Figure 5.14 (a) and (b) are for the same membrane at two different locations that still showed non uniform final thickness after ISE for 30 seconds. Figure 5.14 (c) shows a uniform membrane after ISE for 60 seconds, however, the ISE reduced the macrovoids sizes significantly, as well as the overall membrane final thickness to reach $\sim 123.5 \mu\text{m}$. In this respect, it seems that 30 seconds ISE was not enough to solidify the membrane (increasing its viscosity) so that the "rippling" effect doesn't result in varying the membrane thickness. On the other hand, the 60 seconds of ISE seemed to lead to an increase in membrane viscosity significant enough to overcome this effect. However, this came at the cost of a small volume of the solvent remaining leading to the reduction of the macrovoids.

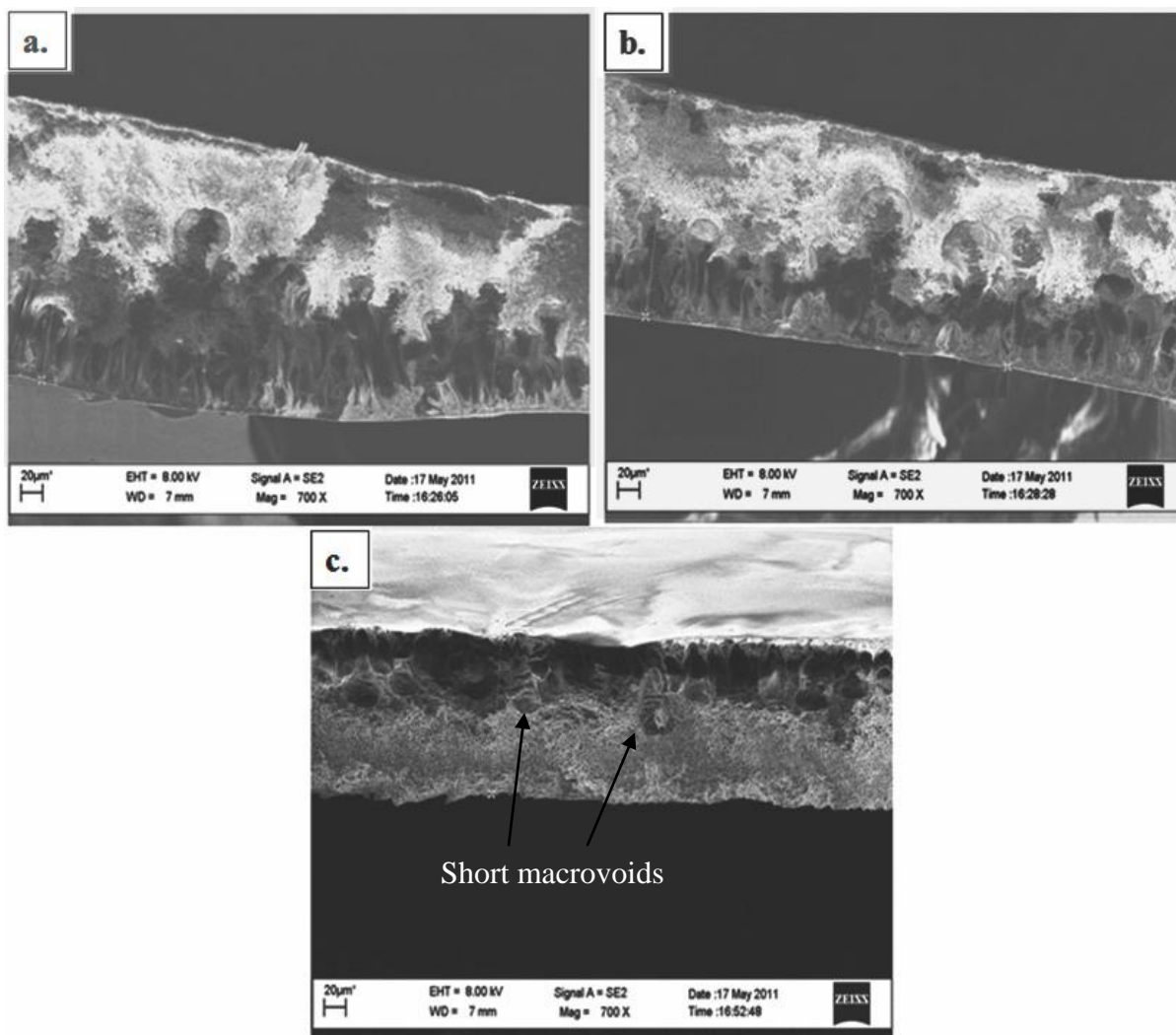


Figure 5.14 SEM of 13 wt% CA membranes, ICT = 1000 μm , and PI at room temperature: (a) and (b) are two different locations on the same sample with ISE = 30 sec, final thickness range = 217-161 μm , (c) uniform sample prepared with ISE = 60 sec., final thickness = 123.5 μm

5.1.5 Addition of H₂O (Non-Solvent)

The results of the effect of added H₂O as non-solvent on membrane morphology are displayed in Figures 5.15, 5.16, and 5.17. In Figure 5.15, 17 wt% CA membranes prepared with ICT of 700 μm , PI carried out at room temperature, and different H₂O non-solvent contents: 0 wt%, 10 wt%, 15 wt%, and 20 wt% (Figures 5.15 (a), (b), (c), and (d) respectively) showed a clear change in membrane final thickness and macrovoids shapes and sizes. In Figure 5.15 (a), the macrovoids sizes were small and the membrane final thickness was ~ 80 μm . As water % increased by 5 wt%, the membrane final thickness increased to ~ 137 μm and medium size macrovoids started developing with a finger like shape as shown in Figure 5.15 (b). Further increase in water content to 15 wt% increased the final thickness further to reach ~ 153 μm and large drop-like macrovoids developed as shown in Figure 5.15 (c). With 20 wt% water addition, the membrane final thickness increased to reach ~ 246 μm and the shape of the macrovoids differed, where some had the typical drop-like shape, while others had a spherical like shape as shown in Figure 5.15 (d).

It is noteworthy that the further increase in the water content to 25 wt% failed to give a homogenous CA stock solution since the CA wasn't able to dissolve in the presence of such high percentage of non-solvent additive to CA-acetone solution.

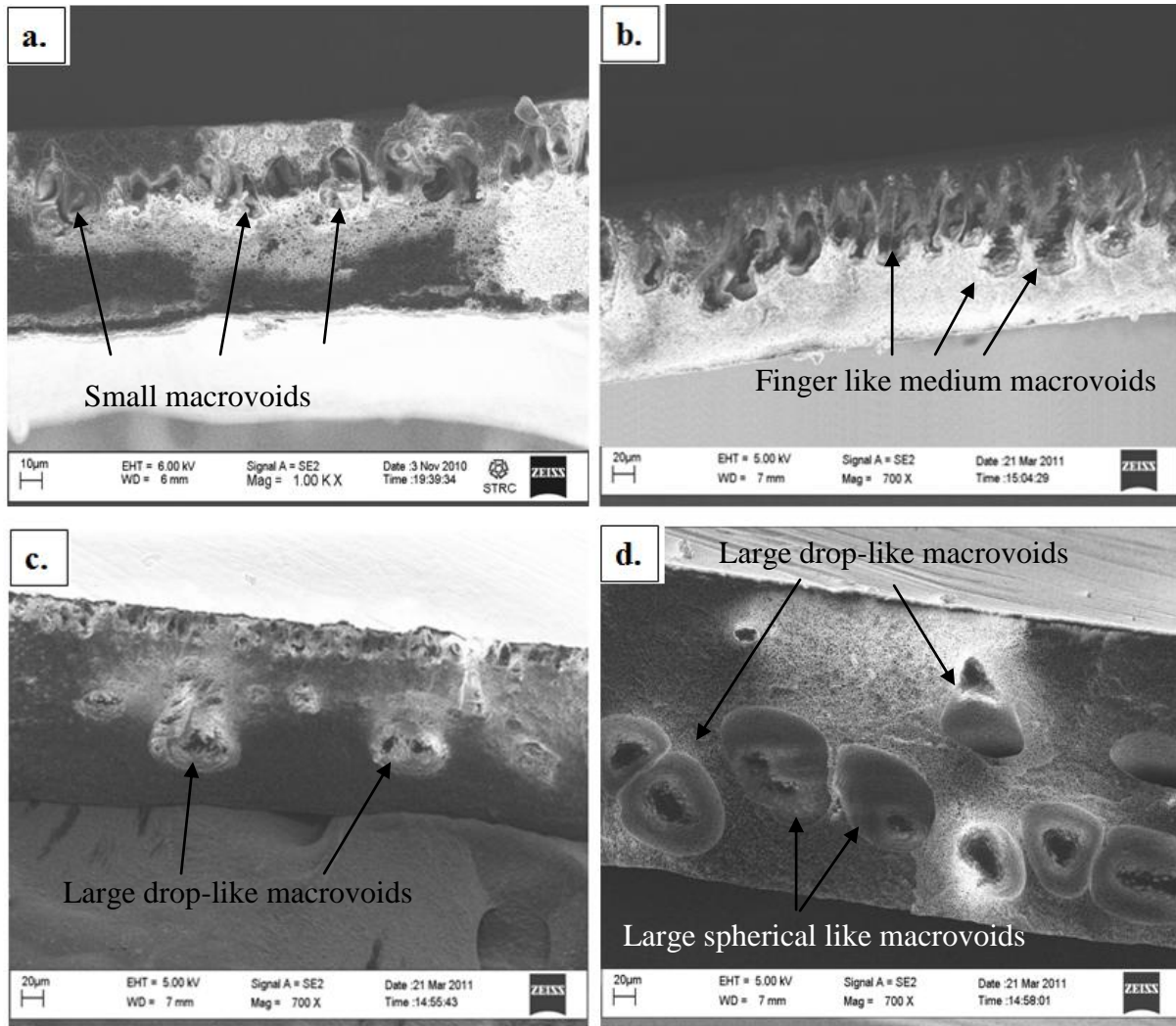


Figure 5.15 SEM of 17 wt% CA, PI at room temperature, ICT = 700 μm : (a) 0 wt% H_2O , final thickness = $\sim 80 \mu\text{m}$, (b) 10 wt% H_2O , final thickness = $\sim 137 \mu\text{m}$, (c) 15 wt% H_2O , final thickness = $\sim 153 \mu\text{m}$, (d) 20 wt% H_2O , final thickness = $\sim 246 \mu\text{m}$

The results of the second set entailing 15 wt% CA membranes, ICT of 300 μm , PI at room temperature, and H_2O contents of 5 wt%, and 20 wt% showed a similar trend. The increase in water content generally enhanced macrovoids formation. Figure 5.16 (a) shows that though 5 wt% H_2O wasn't able to promote macrovoids formation in the small final thickness of the membrane ($\sim 30 \mu\text{m}$). The increase in water content to 20 wt% resulted in the development of large macrovoids drop-like in shape, and a membrane final thickness increase to $\sim 80 \mu\text{m}$ (Figure 5.16 (b)).

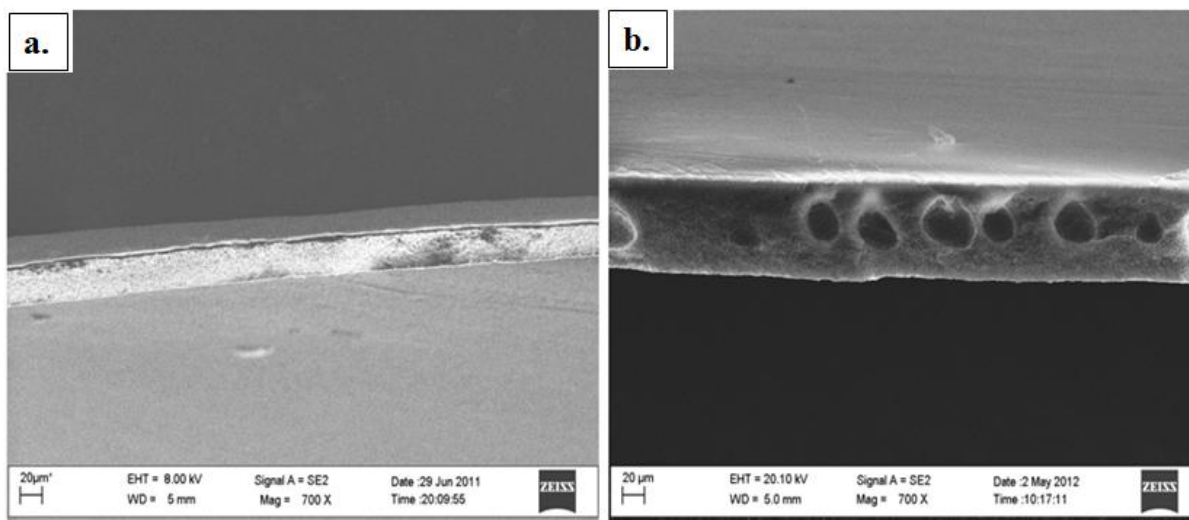


Figure 5.16 SEM of 15 wt% CA, PI at room temperature, ICT = 300 μm : (a) 5 wt% H_2O , final thickness = $\sim 30 \mu\text{m}$, (b) 20 wt% H_2O , final thickness = $\sim 80 \mu\text{m}$

The results of the third set entailing 14 wt% CA content, ICT of 1000 μm , PI at room temperature, and H_2O water contents of 0 wt%, 5 wt%, and 20 wt% are displayed in Figure 5.17 (a), (b), and (c) respectively. In Figure 5.17 (a), the final thickness of the membrane was $\sim 138 \mu\text{m}$ with large drop-like macrovoids, as well as small ones. When 5 w% water was added, the final thickness of the membrane increased to be $\sim 199 \mu\text{m}$ and the size and number of the large macrovoids increased as well as shown in Figure 5.17 (b). With the further increase in water content to 10 wt%, the final thickness of the membrane increased more to $\sim 264 \mu\text{m}$, associated with the increase in macrovoids size as shown in Figure 5.17 (c).

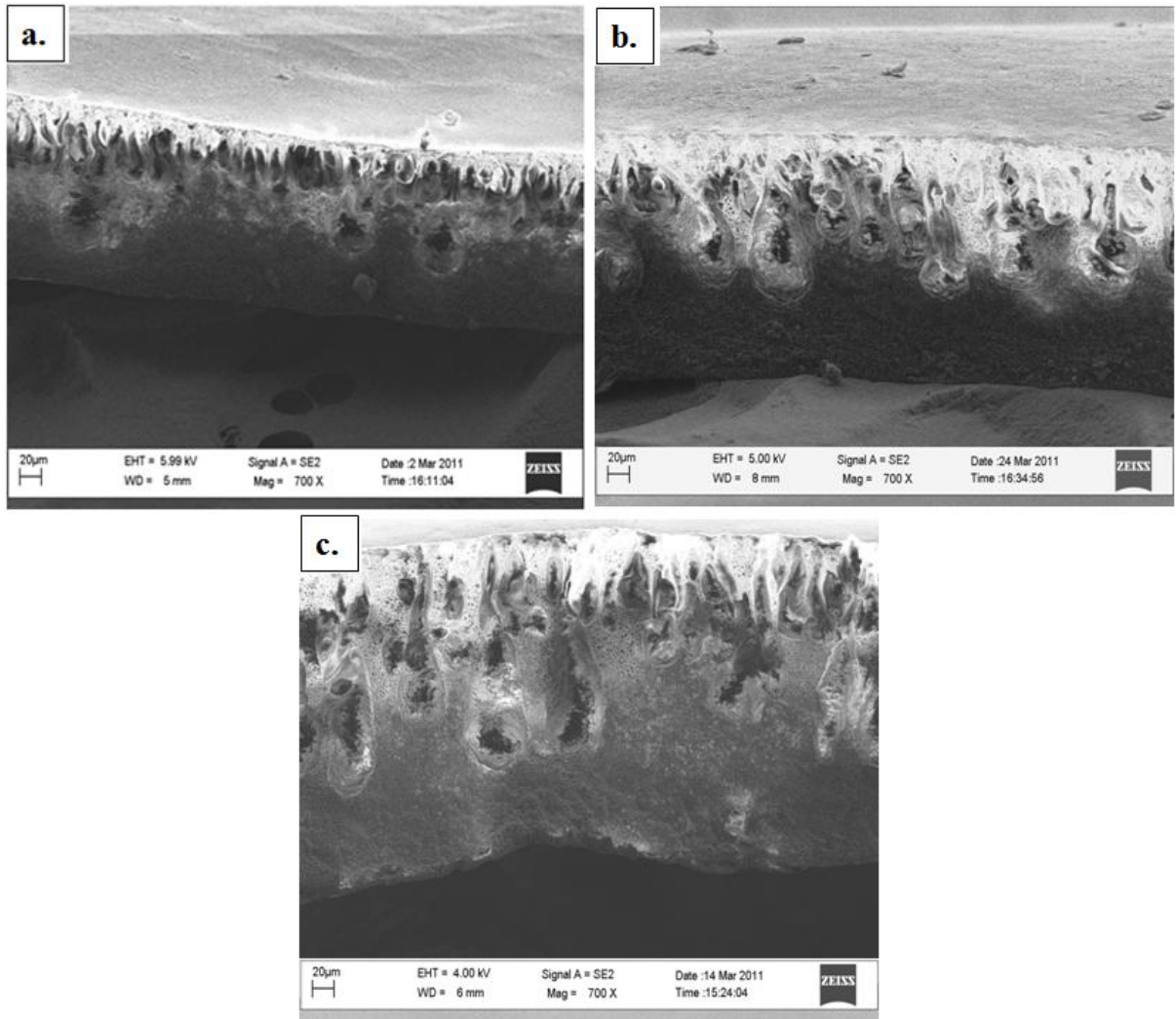


Figure 5.17 SEM of 14 wt% CA, PI at room temperature, ICT = 1000 μm : (a) 0 wt% H_2O , final thickness = $\sim 138 \mu\text{m}$, (b) 5 wt% H_2O , final thickness = $\sim 199 \mu\text{m}$, (c) 10 wt% H_2O , final thickness = $\sim 264 \mu\text{m}$ (non-uniform)

Table 5.5 summarizes the macrovoids dimensions of Figures 5.15, 5.16, and 5.17. The results indicate a general increase in macrovoids formation with increased water content (as non-solvent) in membrane solution. This is also shown to lead to increase in membranes final thickness.

Table 5.5 Macrovoids numbers and dimensions relative to non-solvent addition

17 wt% CA membrane				
Non-solvent addition (H₂O)	ICT (μm)	FT (μm)	Macrovoids number	Macrovoids dimensions (length (μm) X width (μm))
0 wt%	700	~80	15	20 X 15
10 wt%	700	~137	15	60 X 26
15 wt%	700	~153	2	74 X 70
			28	24 X 20
20 wt%	700	~256	8	100 X 96

15 wt% CA membrane				
Non-solvent addition (H₂O)	ICT (μm)	FT (μm)	Macrovoids number	Macrovoids dimensions (length (μm) X width (μm))
5 wt%	300	~30	0	0
20 wt%	300	~80	7	44 X 38

14 wt% CA membrane				
Non-solvent addition (H₂O)	ICT (μm)	FT (μm)	Macrovoids number	Macrovoids dimensions (length (μm) X width (μm))
0 wt%	1000	~138	3	60 X 40
			22	40 X 20
5 wt%	1000	~199	5	98 X 36
			14	60 X 32
10 wt%	1000	~264	6	120 X 56
			16	50 X 30

The increase in macrovoids size due to the addition of a non-solvent to the casting solution had been reported in the literature [21, 23, 25, 52]. Macrovoids size increase with the content of non-solvent added to the casting solution was explained by Smolders et al. [52]. It is believed that this is the result of a local induced nucleation under the dense layer once the cast solution is immersed in the non-solvent bath. This is due to the presence of the solvent in high contents in this area, thus delaying the liquid-liquid demixing, and expanding the nuclei sizes. In other words, when the cast solution is immersed in the non-solvent bath, instantaneous demixing happens and the solvent heads upwards into the non-solvent bath. This increases, the solvent's, concentration under the nascent dense skin. At the same time, there exists a quantity of non-solvent in the cast solution that started nucleation without waiting for the non-solvent of the coagulation bath to enter and replace the solvent present. At that point, a local induced nucleation takes place, which is accompanied by delayed demixing at the borders of the nuclei under the effect of the increased solvent concentration below the top layer. This would give enough time for the solvent to enter into the non-solvent

droplets, and expand their size, and this time would be longer than the usual time taken for this process to complete without the presence of the non-solvent in the cast solution.

5.1.6 Addition of CNTs

A. Effect of presence of pNTs on membrane morphology:

Pristine CNTs had a compacting effect on CA membranes. Figure 5.18 and 5.19 show the effect of compaction on the middle sections⁴ of membranes prepared with 13 wt% CA content in acetone. Figure 5.18 shows the morphological difference between 0 wt% pNT membrane (Figures 5.18 (a) and (b) at two different magnifications), as compared to a 0.5 wt% pNT membrane (Figures 5.18 (c) and (d)). The 0.5 wt% pNT was found to have denser polymer areas between pores and smaller pore sizes.

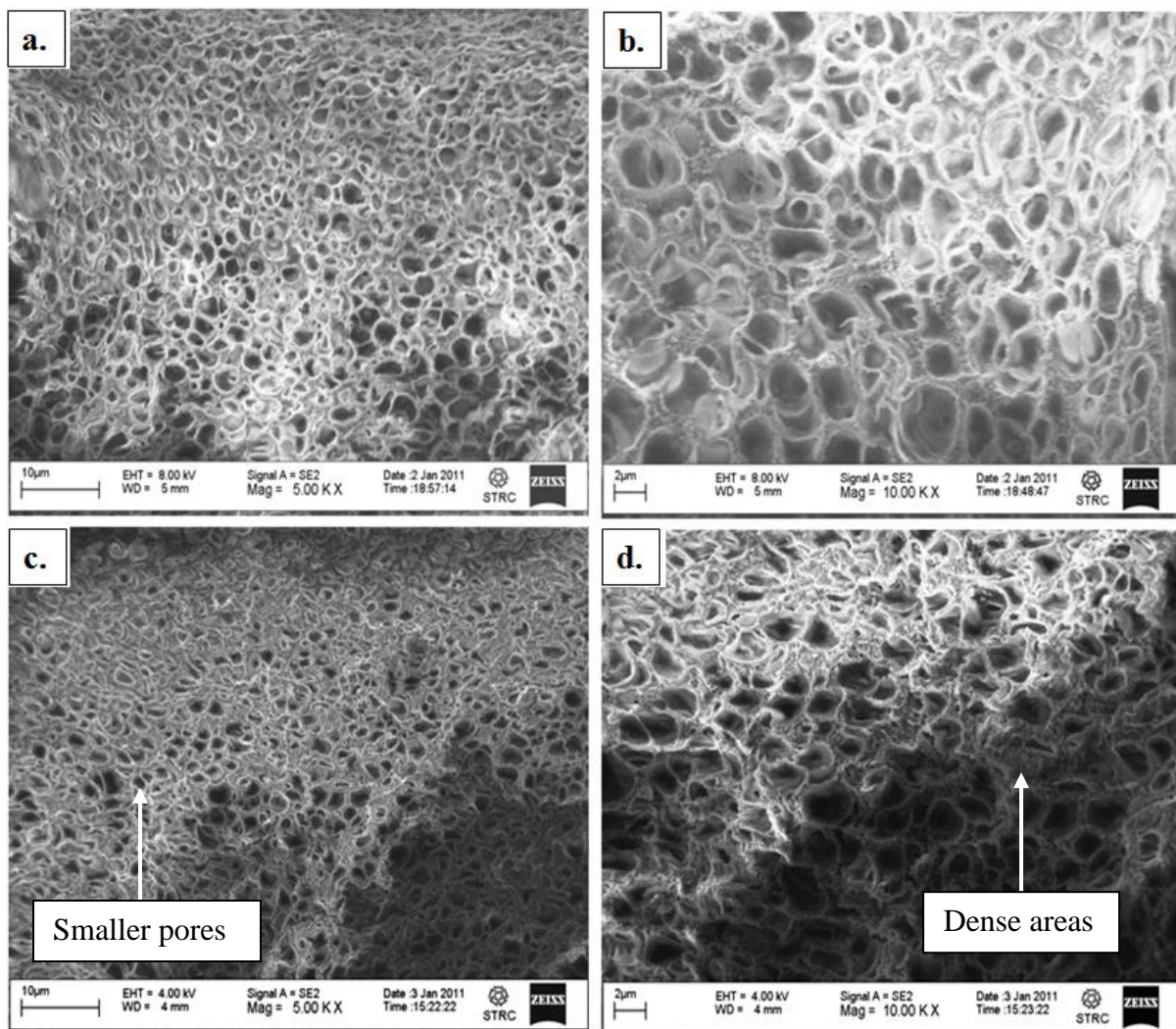


Figure 5.18 SEM displaying compaction difference in the middle sections of 13 wt% CA membranes, PI at room temperature: (a) 0 wt% pNTs at 5KX, (b) 0 wt% pNTs at 10KX, (c) 0.5 wt% pNTs at 5KX, (d) 0.5 wt% pNTs at 10KX

⁴ The location of the middle section of a membrane was illustrated in Figure 5.1.

Further investigation was carried out using 17 wt% CA content, which showed the same effect. A 0.5 wt% pNTs lead to a denser membrane with smaller pore sizes (Figure 5.19).

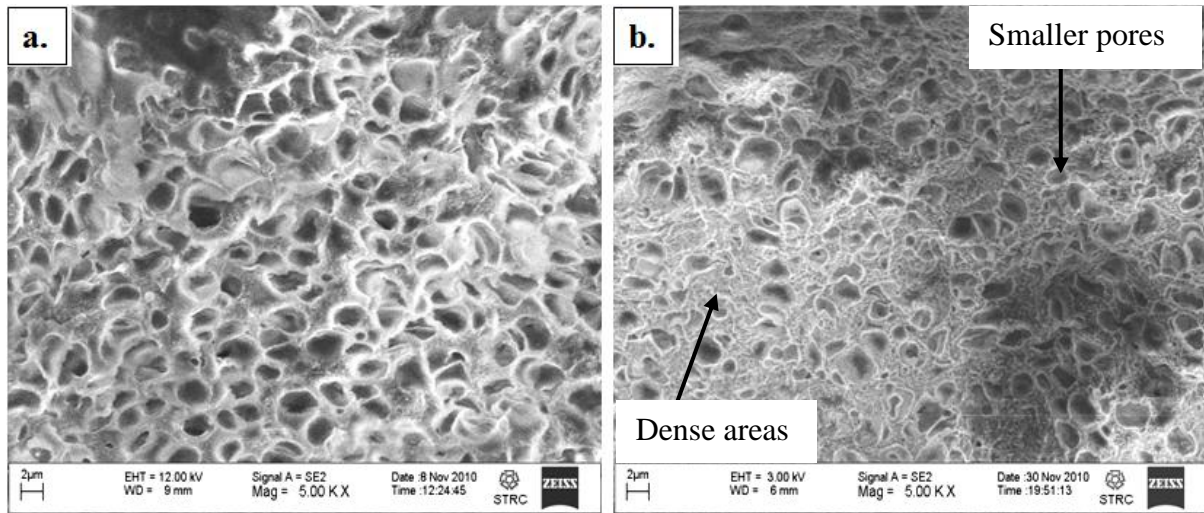


Figure 5.19 SEM displaying compaction difference in the middle sections of 17 wt% CA membranes, PI at room temperature: (a) 0 wt% pNTs at 5KX, (b) 0.5 wt% pNTs at 5KX

As for the effect of pNTs content, as expected, lower pNT content lead to better dispersion as seen in Figure 5.20, where larger pNT agglomerates were clear for the higher, 1wt% content (1 agglomerate of about 9 μm width) when compared to 0.5 wt% pNT content (3 agglomerates of about 2 μm width). When comparing the middle sections of these membranes together with 0 wt% pNTs, there were areas in the middle sections with no significant difference between all three membranes, which is indicative that the pNTs were not properly dispersed within the whole membrane structure (Figure 5.21).

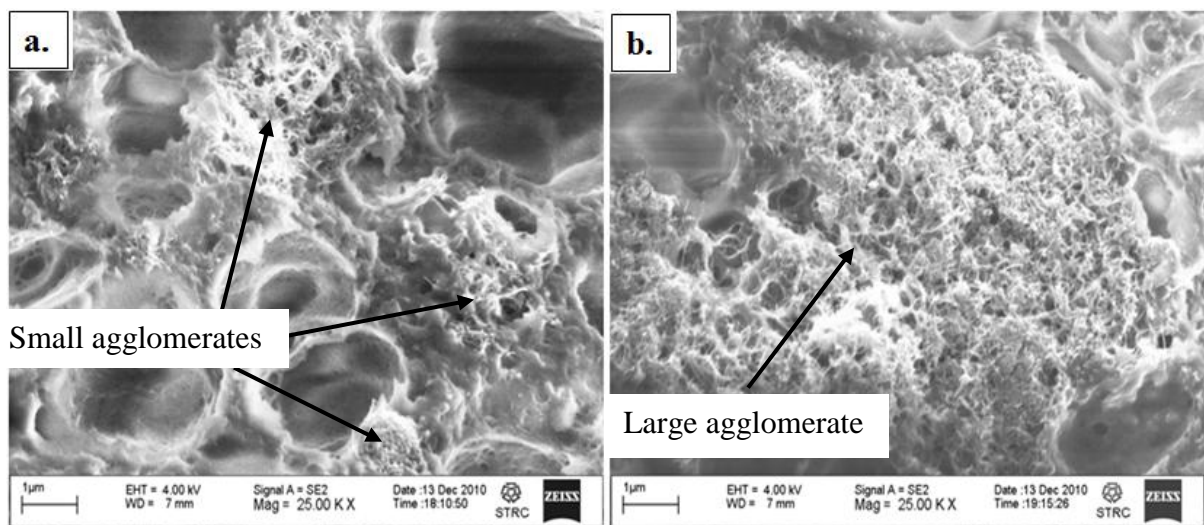


Figure 5.20 SEM of agglomerates of pNTs in 17 wt% CA membranes at 25KX in the middle section of the membranes: (a) 0.5 wt% pNTs at 25KX, (b) 1 wt% pNTs at 25KX

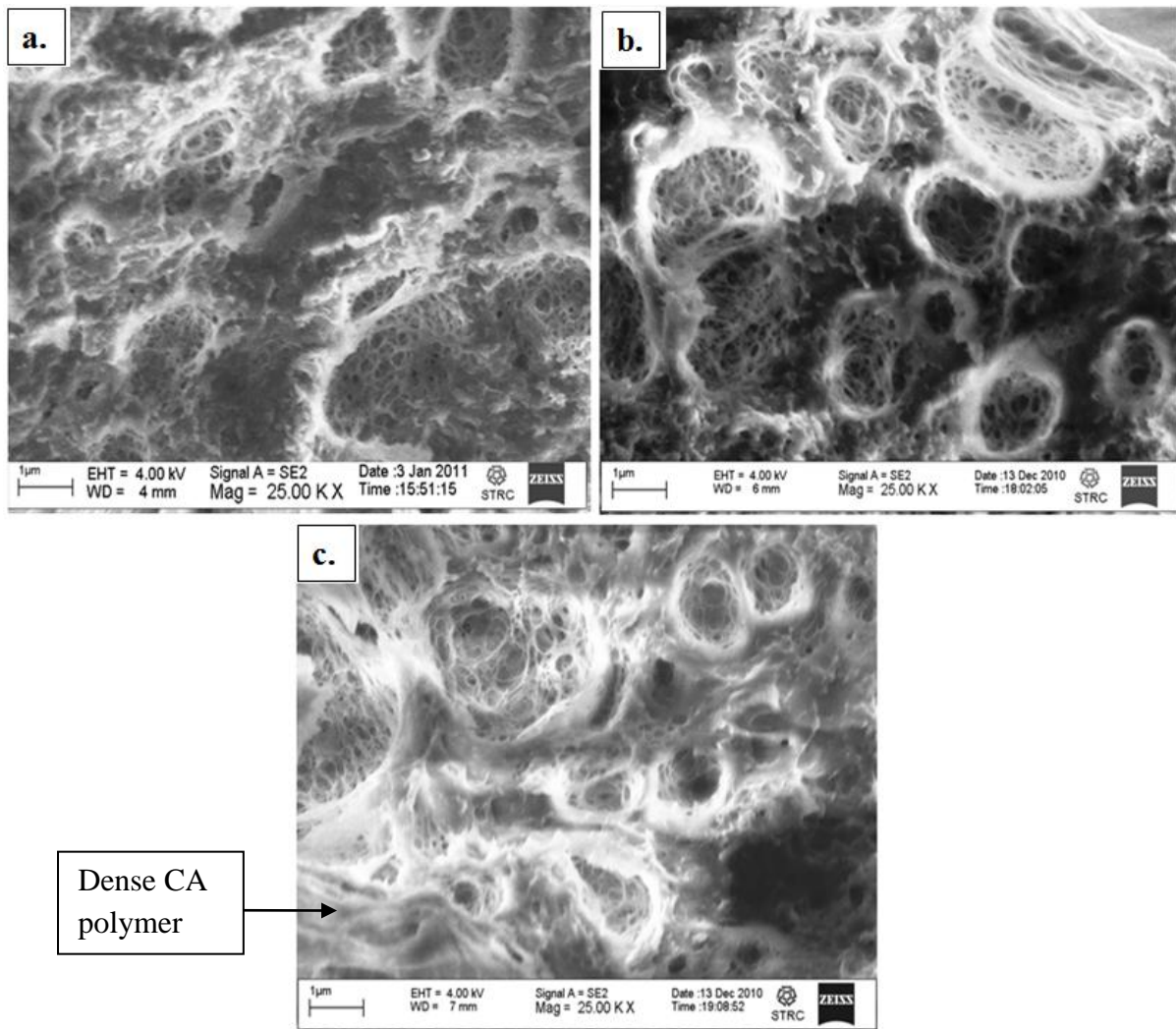


Figure 5.21 SEM of the pores structures in the middle section of 17 wt% CA membranes at 25KX: (a) 0 wt% pNTs membrane, (b) 0.5 wt% pNTs membrane, (c) 1 wt% pNTs membrane

These results show that it was very challenging to disperse pNTs within CA membranes due to the pNTs highly hydrophobic nature [62]. The denser pNTs membrane structure is due to the space occupied by the pNTs that resulted in high compactness of the membrane as explained in the literature [40]. Furthermore, the quantity of the nanotubes that were able to disperse within the CA solution could lead to delayed demixing process. This is because the cast solution would have a hydrophobic source, the pNTs, which would slow down the penetration of the polar non-solvent (water) from the coagulation bath to start nucleation and formation of the polymer lean phase, thus, slowing down the process and reducing the pore sizes.

B. Functionalization of CNTs:

In order to enhance the dispersion of CNTs within the CA matrix, functionalization via oxidation purification in acidic medium was carried out. SEM, as well as FTIR were used to verify the success of functionalization. Below are the comparative SEM images for both pNTs and fNTs.

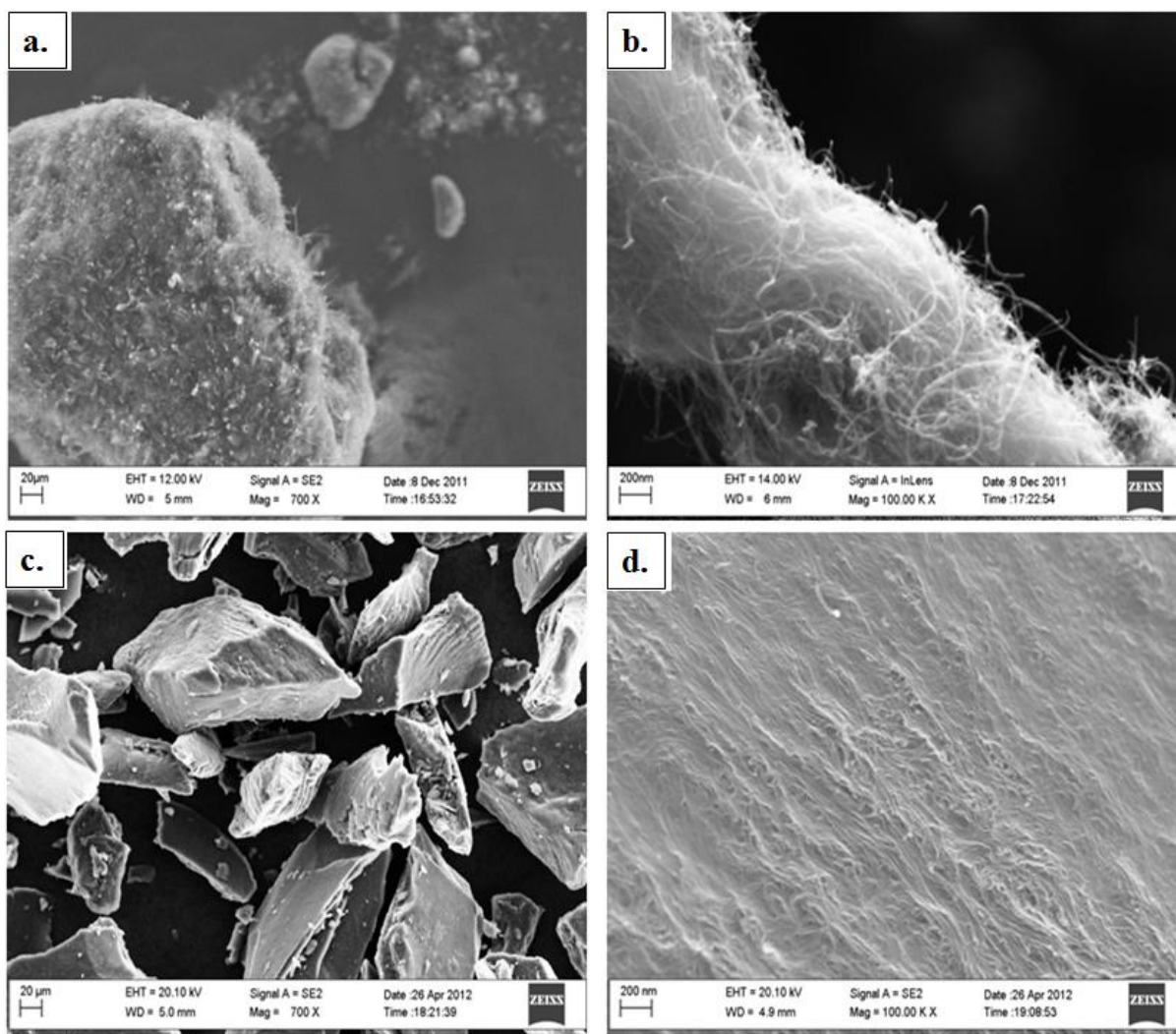


Figure 5.22 SEM image of both pNTs and fNTs: (a) an agglomerate of pNTs at 700X, (b) a bundle of pNTs at 100 KX, (c) agglomerates of fNTs at a small magnification (700X), (d) arrays of fNTs at 100 KX

The SEM images show a significant change in the shape of the agglomerates where the pNT agglomerates appear as a “thread bundles” with individual CNTs clearly discernable (Figure 5.22 (a), and (b)). On the other hand, fNTs agglomerates are particle like with the CNTs more orderly aligned (Figure 5.22 (c) and (d)). This is due to the strong interaction between the COOH groups attached to the CNTs as a result of functionalization.

The FTIR spectra of both CNTs are presented in Figures 5.23 and 5.24, with noticeable differences.

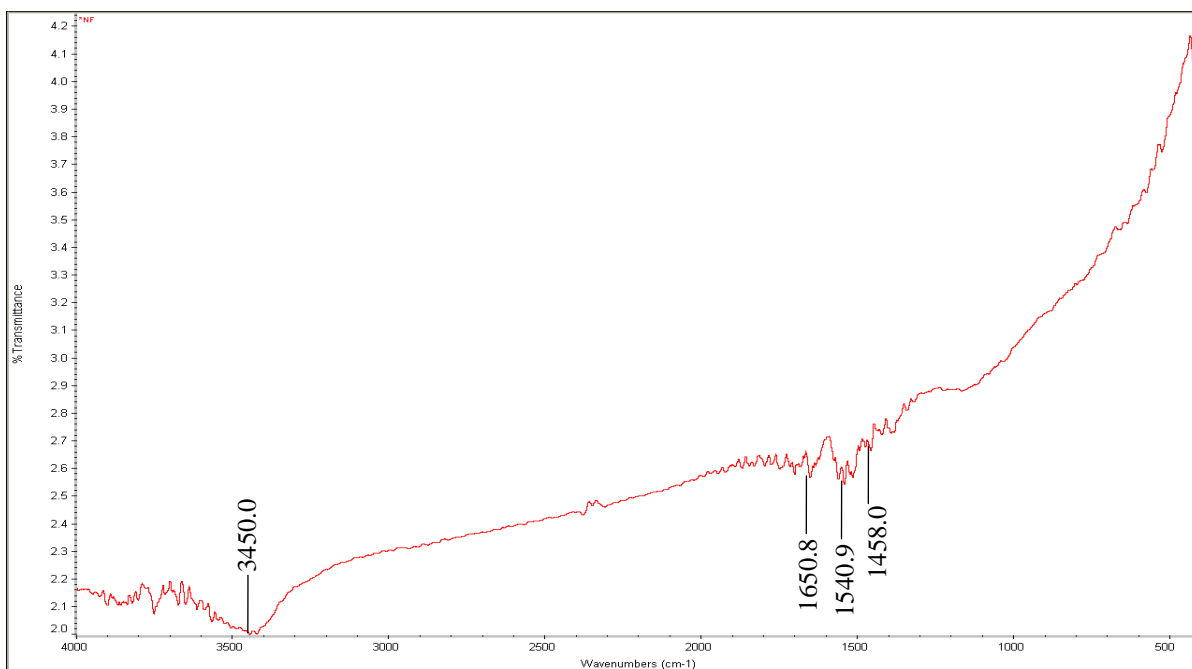


Figure 5.23 FTIR spectrum of non-functionalized MWCNTs

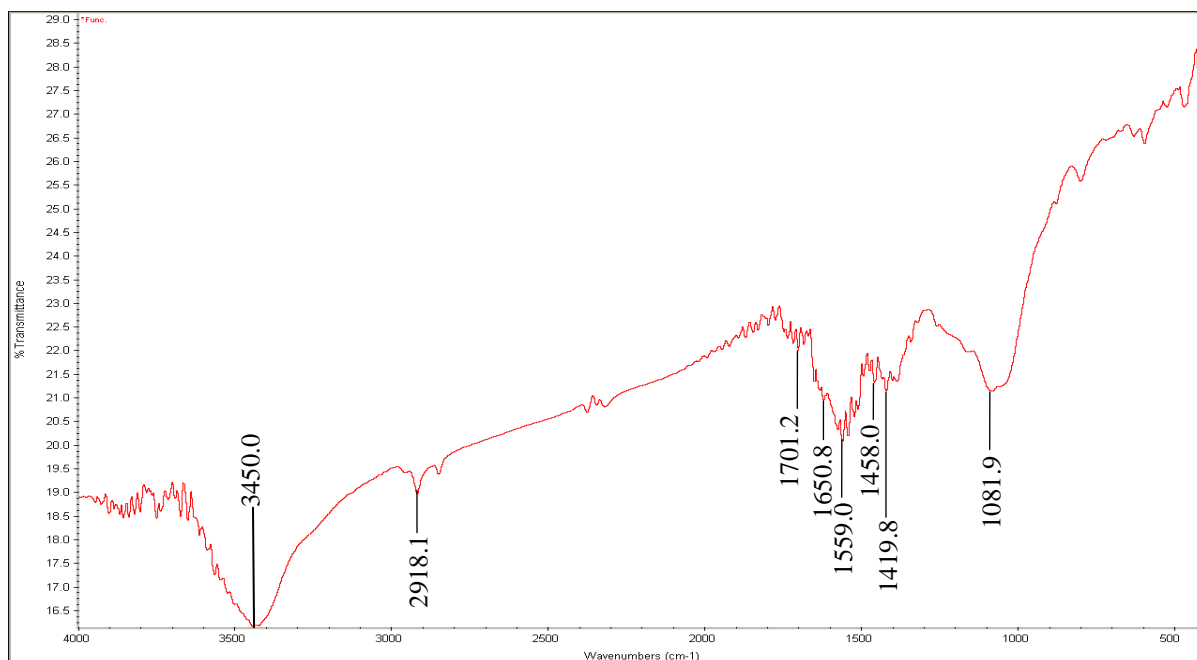


Figure 5.24 FTIR spectrum of functionalized MWCNTs

Functionalization of CNTs showed a strong absorption band at 3450 cm⁻¹ associated with the presence of OH groups (stretching mode) on the surface of the nanotubes from two sources, the COOH group, as well as adsorbing humidity. The appearance of an absorption peak at 2918.1 cm⁻¹ that didn't show for the pNT reflects the single bonds of the OH groups (stretching mode) of the COOH groups. The peak at 1701 cm⁻¹ is probably due to C=O groups (stretching mode) of COOH, or CO of ketones/quinines if present. Strong absorption peaks from 1650 cm⁻¹ to 1450 cm⁻¹ are usually characteristic for C=C of aromatic rings (stretching mode), or in this case, aromatic like structure. These peaks appeared for both pNT

and fNTs, reflecting the C-C bonding structure of the nanotubes. The absorption peak at 1419 cm^{-1} is for single bond of C-O of the C-OH (bending mode), associated with a strong peak at 1081 cm^{-1} corresponds to the stretching mode of the same bond. As for the broad absorption peak in Figure 5.23 of pNTs at 3450 cm^{-1} , it corresponds to the stretching modes of OH the water molecule reflecting the presence of humidity within the sample [96-97]. It is important to note that Stobinski et al. [96] reported FTIR spectra for functionalized CNTs, identical to the one reported here. Their CNTs were also functionalized using oxidation purification under similar conditions. These results show that functionalization of CNTs was successful.

Dispersion trials were carried out for both fNTs and pNTs in water. Figure 5.25 shows the difference between two dispersions of 0.1 grams of fNTs and pNTs in 20 ml water. From the figure, it is clear that the fNTs were fully dispersed in the medium (Figure 5.25 (a)), however, the pNTs failed to do so due to their highly hydrophobic nature, where agglomerates of pNTs could be seen at the bottom of the beaker (Figure 5.25 (b)).

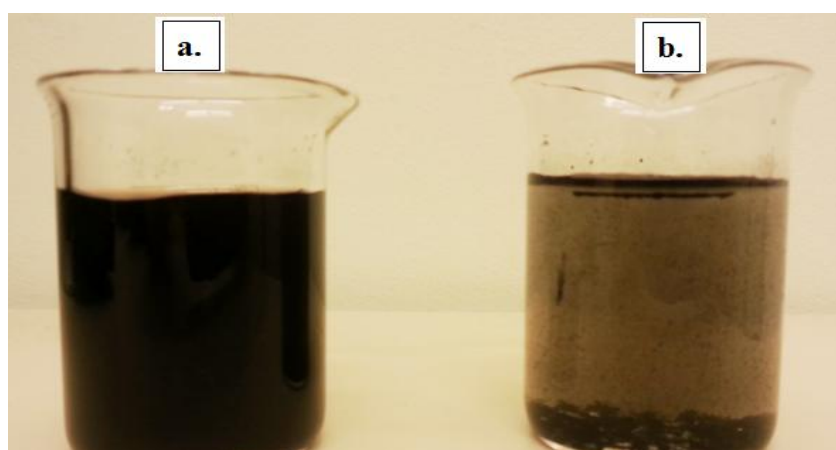


Figure 5.25 Beakers filled with 0.01 g CNTs, sonication time for 1 minute in 20 ml deionized water, (a) fNTs fully dispersed giving opaque black solution, (b) pNTs poorly dispersed forming agglomerates throughout the solution and on the bottom of the beaker

On testing fNTs dispersion in acetone vs. water, before mixing the dispersed nanotubes solution with the CA stock solution, it was found that fNTs disperse in water much more than in acetone, probably due to the high polarity nature of the latter, which is compatible with the functional groups located on the surface of the functionalized nanotubes. This lead to the usage of lower weight percentage of fNTs to develop the CA based nanocomposites, and minimal sonication time (less than 1 minute) to achieve good dispersion.

C. Effect of the content of fNTs on their dispersion within the CA membranes:

fNTs orientation inside the CA matrix was investigated using SEM. Large networks fNTs were easily spotted for the 0.005 and 0.01 wt% nanotubes contents. For the 0.0005 wt% fNTs, individual nanotubes were imaged. Figures 5.26, 5.27, and 5.28 show the random distribution and orientations of fNTs within the CA matrices of 0.0005 wt%, 0.005 wt% and 0.01 wt% fNTs respectively. The fNTs are highlighted with the red arrows.

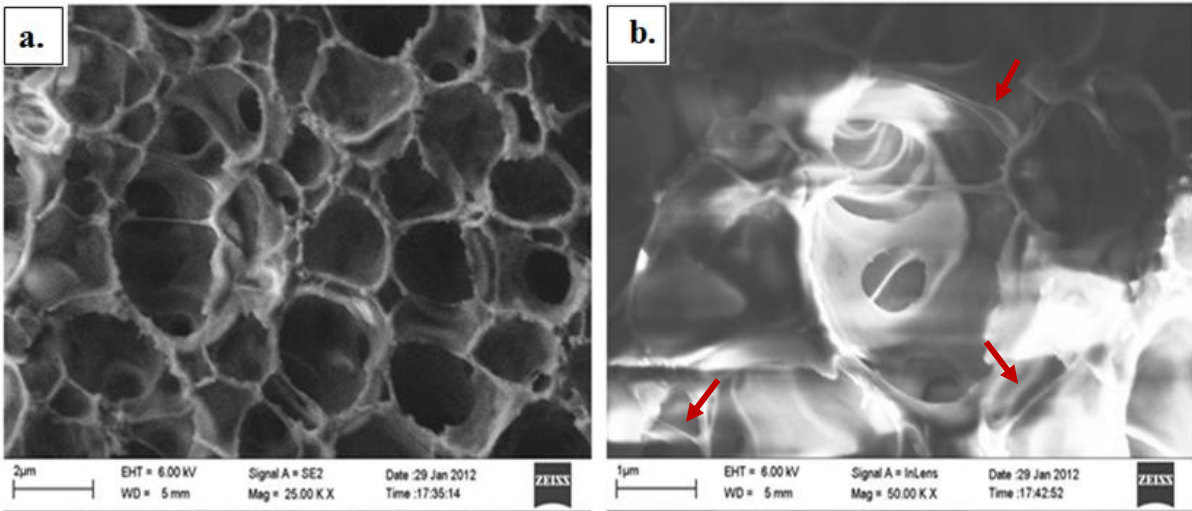


Figure 5.26 MWCNTs networks in 0.0005/15/20 wt% fNT/CA/H₂O nanocomposite at different SEM magnifications, (a) at 25KX, (b) at 50KX

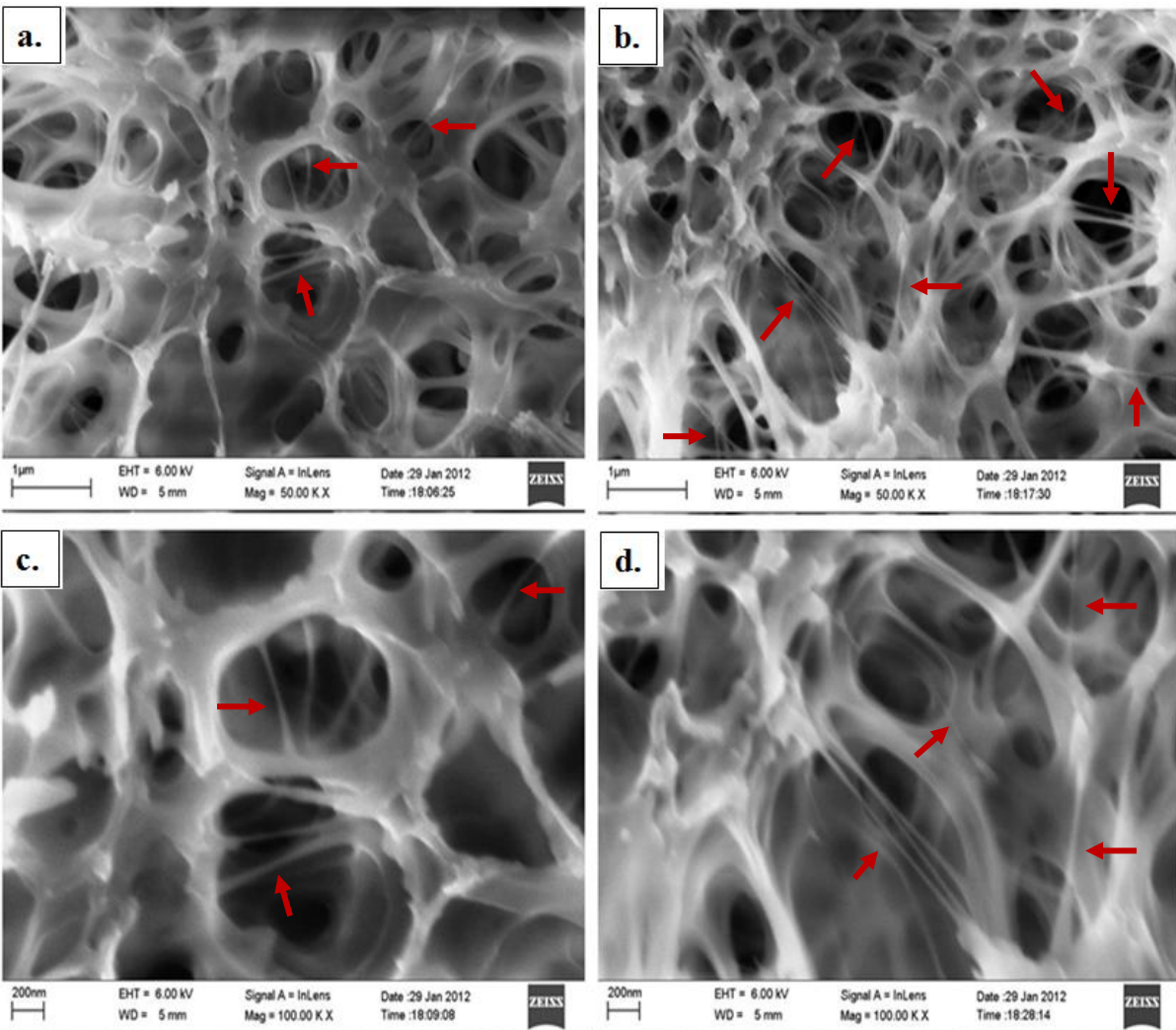


Figure 5.27 MWCNTs networks in 0.005/15/20 wt% fNT/CA/H₂O nanocomposite at different SEM magnifications, (a) at 50KX, (b) at different location at 50KX, (c) at 100KX, (d) at different location at 100KX

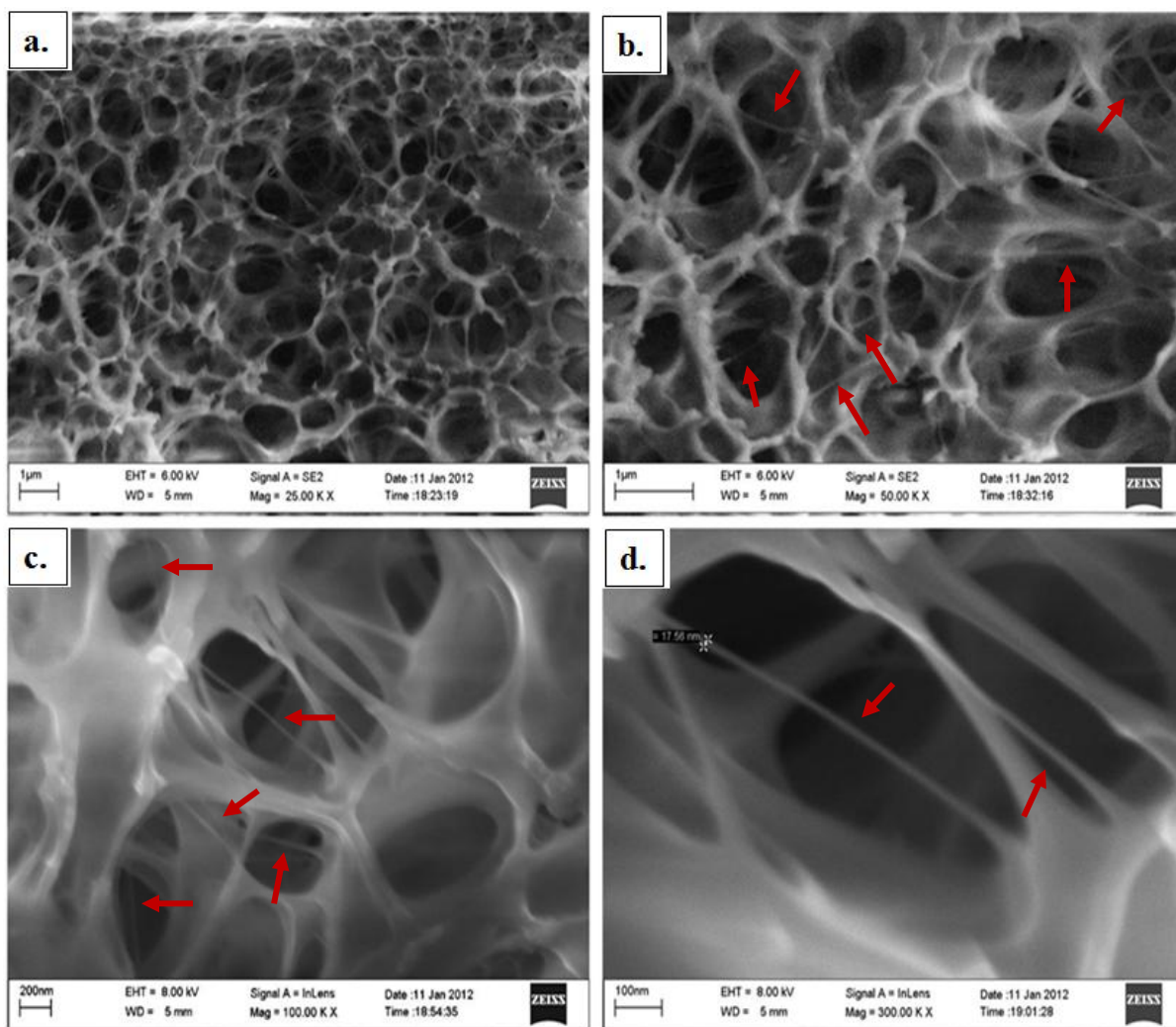


Figure 5.28 MWCNTs networks in 0.01/15/20 wt% fNT/CA/H₂O nanocomposite at different SEM magnifications, (a) at 25 KX, (b) at 50KX, (c) at 100KX, (d) at 300KX

The images show that fNTs were randomly oriented and properly dispersed within the CA membranes, creating large networks that extended across the membranes, and no agglomerates were detected.

Further investigations on the effect of fNTs on morphology included studying their effect on macrovoids formation. SEM images in Figure 5.29 showed that the addition of fNTs to the CA membranes resulted in a significant reduction in size and number of large macrovoids (for the same final membrane thicknesses) associated with the increase in fNTs contents forming 0/15/20 wt%, 0.0005/15/20 wt%, 0.005/15/20 wt%, and 0.01/15/20 wt% fNT/CA/H₂O nanocomposites (Figure 5.29 (a), (b), (c), and (d) respectively). Table 5.6 displays the macrovoids numbers and dimensions relative to the fNTs quantities used.

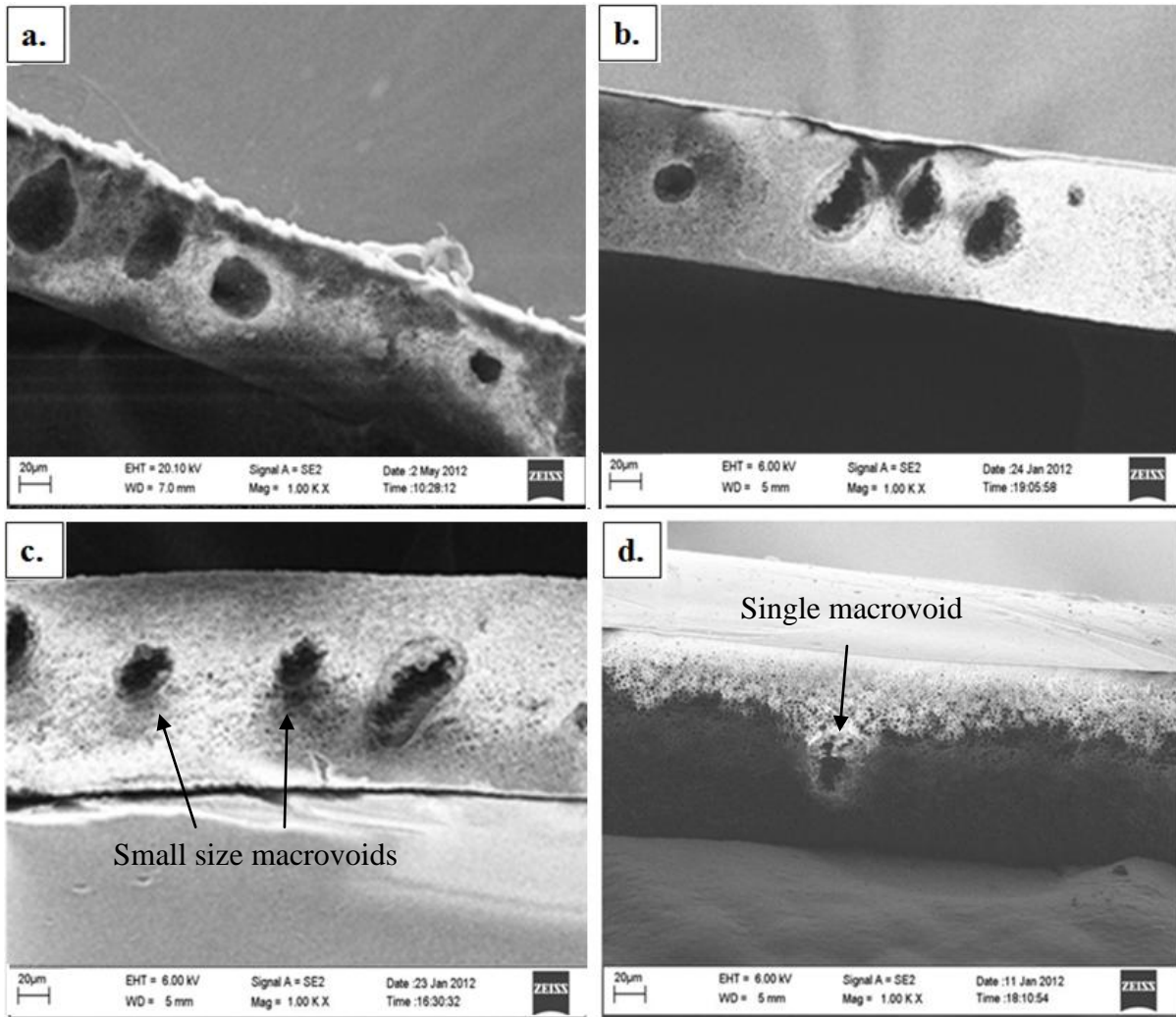


Figure 5.29 SEM of morphology at same final thickness ($100\pm 10\ \mu\text{m}$): (a) 0/15/20 wt% fNT/CA/H₂O, (b) 0.0005/15/20 wt% fNT/CA/H₂O, (c) 0.005/15/20 wt% fNT/CA/H₂O, (d) 0.01/15/20 wt% fNT/CA/H₂O

Table 5.6 Macrovoids numbers and dimensions relative to fNTs addition

15/20 wt% CA/H ₂ O membrane				
fNTs addition	ICT (μm)	FT (μm)	Macrovoids number	Macrovoids dimensions (length (μm) X width (μm))
0 wt%	350	100 \pm 10	4	46 X 38
0.0005 wt%	400	100 \pm 10	4	56 X 32
0.005 wt%	400	100 \pm 10	3	46 X 30
0.01 wt%	400	100 \pm 10	1	50 X 30

As discussed earlier, the hydrophobic nature of the pNTs decrease its interaction with the polymer matrices. This changed under the effect of functionalization. This is explained in the literature [38-41] to be due to the enhanced interfacial interaction between the functional groups on the fNTs surfaces with the polymer matrices. In the fNT-CA nanocomposite, such

interactions are strongly suggested to be between the OH of the COOH groups on the fNTs graphene sheets and the carbonyl groups on the ester linkages of the CA polymer [98]. These interactions are thought to be hydrogen bonds.

The increase in the weight percentage of the fNTs suppressed macrovoids formation. A possible explanation is thought to be related to a delay in the overall solvent-non-solvent instantaneous demixing taking place due to the interference of the fNTs in the process. Macrovoids formation in the presence of a percentage of a non-solvent in the cast solution is the result of a local induced nucleation that gets expanded by the solvent in the polymer lean phase below the nascent top layer. In the regular demixing process with the presence of a non-solvent (let's call it *NS1*) in the cast solution, *NS1* is responsible for the local induced nucleation that expands the macrovoids as explained before. The non-solvent in the coagulation bath (let's call it *NS2*) is responsible for the regular nucleation process via demixing with the solvent and the formation of the polymer rich and polymer lean phases. Now, the new intruders, the fNTs, have COOH functional groups on their walls, and they are well dispersed into the cast solution of CA-acetone-*NS1*. Such functional groups can easily develop hydrogen bonds with *NS1*, and the entering *NS2* from the coagulation bath. The hydrogen bonds that probably developed between the nanotubes and *NS1* could delay the induced local nucleation process because *NS1* remained trapped in the CA-acetone-water cast solution, and not separating as fast as it regularly would. This starts changing as *NS2* enters into the cast solution. Regularly, *NS2* forces the solvent out to develop two separate phase, a polymer lean, and polymer rich. At this point, the tendency of the *NS1* to remain mixed with the developing polymer rich phase decreases as the polymer solidifies. Thus, it gets expelled into the polymer lean developing areas. This doesn't necessarily mean that it wouldn't keep the hydrogen bonds with the functional groups on the graphene walls, yet, these bonds could be responsible for the delayed initiation of the local nucleation process. A second possibility entails a contribution of hydrogen bonds between fNTs and *NS2* to delayed demixing process, and nucleation, as the entering *NS2* becomes restrained from its regular free motion via such bonds, thus slowing down the entire process.

5.2 Optimal Preparation Conditions

Based on the above results, the optimal conditions for the preparation of samples to be fully characterized for surface area and porosity, as well as performance for solution permeation and salt retention, were identified as listed in section 4.5. The addition of fNTs to CA membranes has lead to changes in membrane morphology, observed in the number and dimensions of macrovoids, as well as membrane compaction. In addition it has lead to a change in membrane surface area, porosity and performance.

In determining the effect of functionalized CNTs addition, two blank membranes were used. The first blank entailed a membrane cast at a different ICT value, but which had the same final thickness of 100 μm as the nanocomposite membranes containing CNTs. This blank helped compare the effect of CNT addition in light of a constant final membrane thickness. The blank did however present the shortcoming of having a different absolute

amount of CA (as a result of the different ICT values). In this respect, the second blank entailed a membrane having the same ICT value of 400 μm as the nanocomposite membranes with CNTs. This however had a different final thickness value, but contained the same absolute amount of CA.

5.3 Membrane Surface Properties

The results of investigating the pore size distribution for the nanocomposites in comparison to CA membranes included differential pore volumes vs. pore width, differential pore areas vs. pore width, adsorption isotherms, t-plots, micropores volume calculations, external surface areas calculations using t-plot method and BET surface area.

5.3.1 Differential Pore Sizes

The results for fNTs nanocomposites with the same final thickness $100\pm 10\ \mu\text{m}$ in comparison to the two blanks included membranes with compositions (fNT/CA/H₂O): 0/15/20 wt% (ICT = 350 μm), 0/15/20 wt% (ICT = 400 μm), 0.0005/15/20 wt%, 0.005/15/20 wt%, and 0.01/15/20 wt% membranes. Porosity results are shown in Figures 5.30, 5.31, and 5.32.

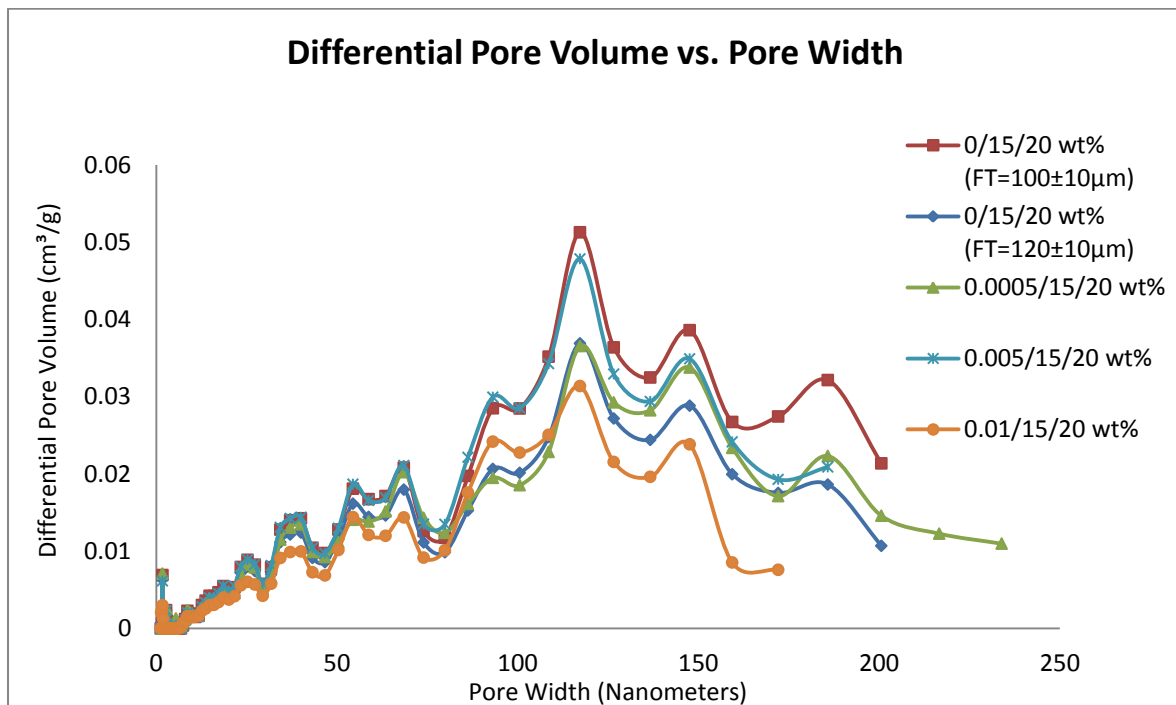


Figure 5.30 Plot of differential pore volumes

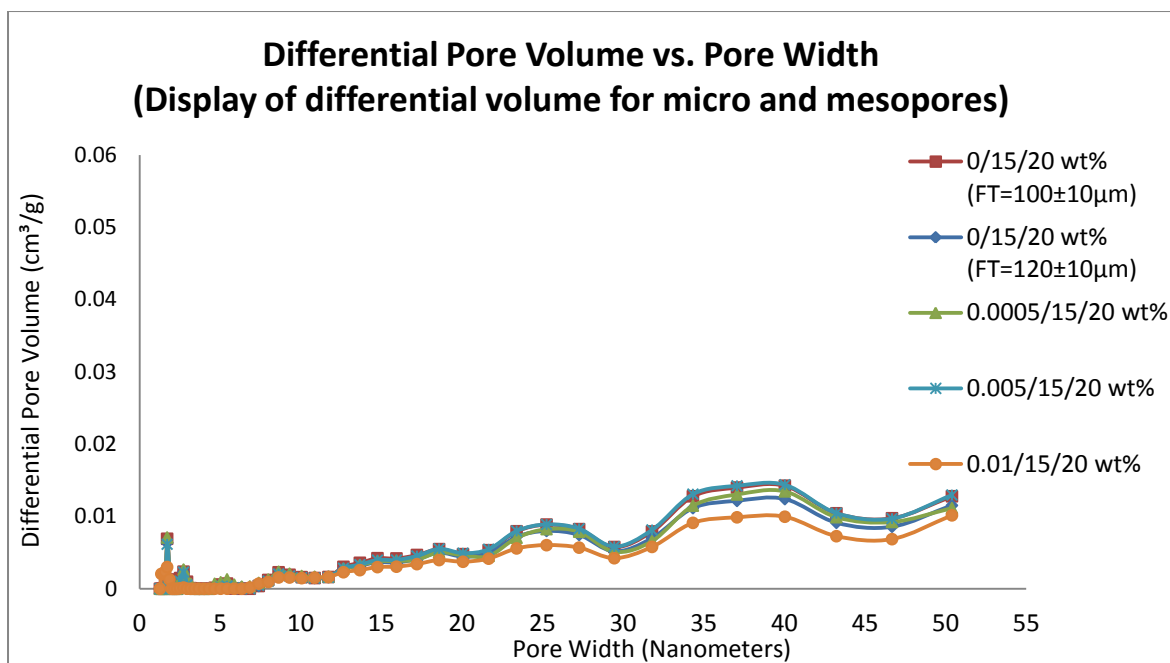


Figure 5.31 Plot of differential pore volumes for micro and mesopores

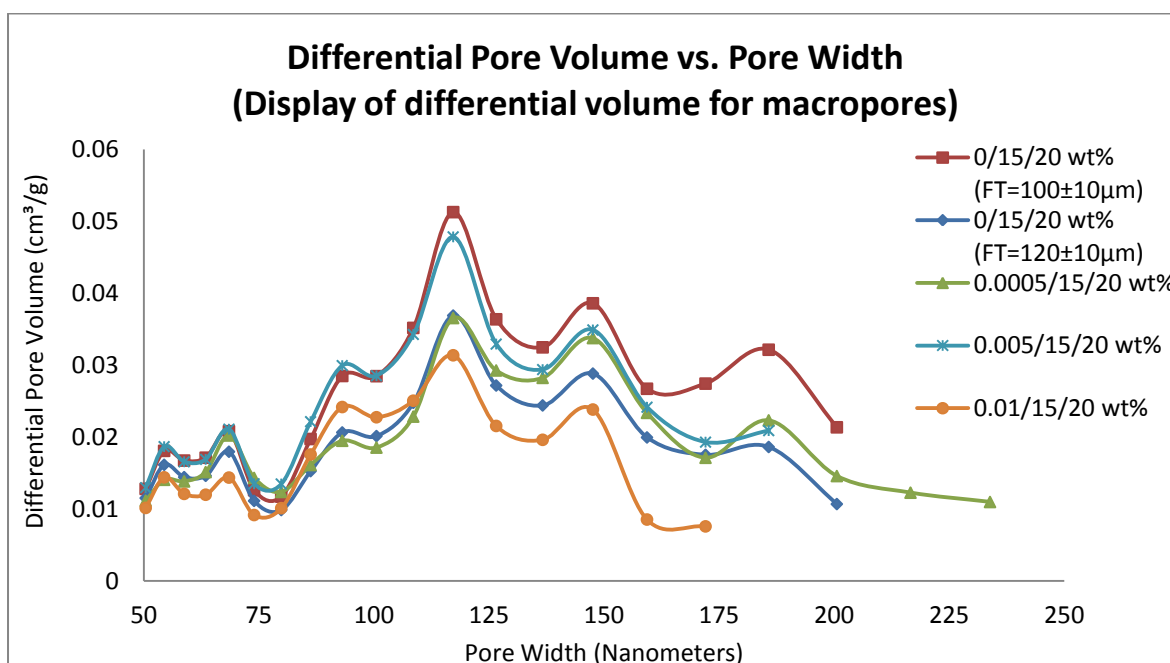


Figure 5.32 Plot of differential pore volumes for macropores

From the plots above, the largest volumes occupied by pores are for those larger than ~20 nm width. Figure 5.31 shows that only the 0/15/20 wt% and 0.0005/15/20 wt% fNT/CA/H₂O had pores of 5 nm width. The same figure shows that all membranes had micropores with width less than 2 nm, however, the amount present varied significantly from one membrane to another.

Figures 5.31 and 5.32 show that the 0.01/15/20 wt% fNT/CA/H₂O membrane had the least volume of pores which means the increase content of fNTs suppressed pores

development. The two figures also show that the pore volumes in the 0/15/20 wt%, the 0.0005/15/20 wt%, and the 0.005/15/20 wt% fNT/CA/H₂O are almost neck to neck in the range from 5nm to 70 nm. However, for pores larger than 70 nm, the 0/15/20 wt% fNT/CA/H₂O (FT = 100±10 μm) had the largest volume occupied by the 117 nm macrovoids. Finally, the plot shows that the 0.0005/15/20 wt% fNT/CA/H₂O membranes had macrovoids larger than 180 nm wide.

Figures 5.33, 5.34, and 5.35 show the corresponding pore area distribution.

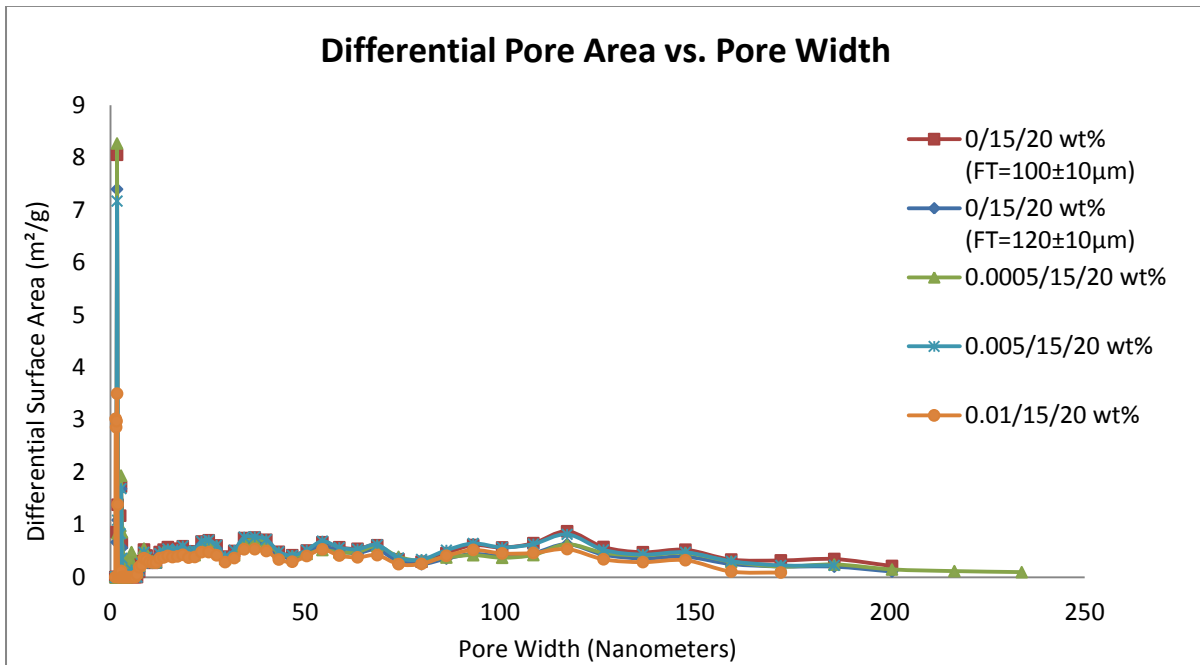


Figure 5.33 Plot of differential pore areas

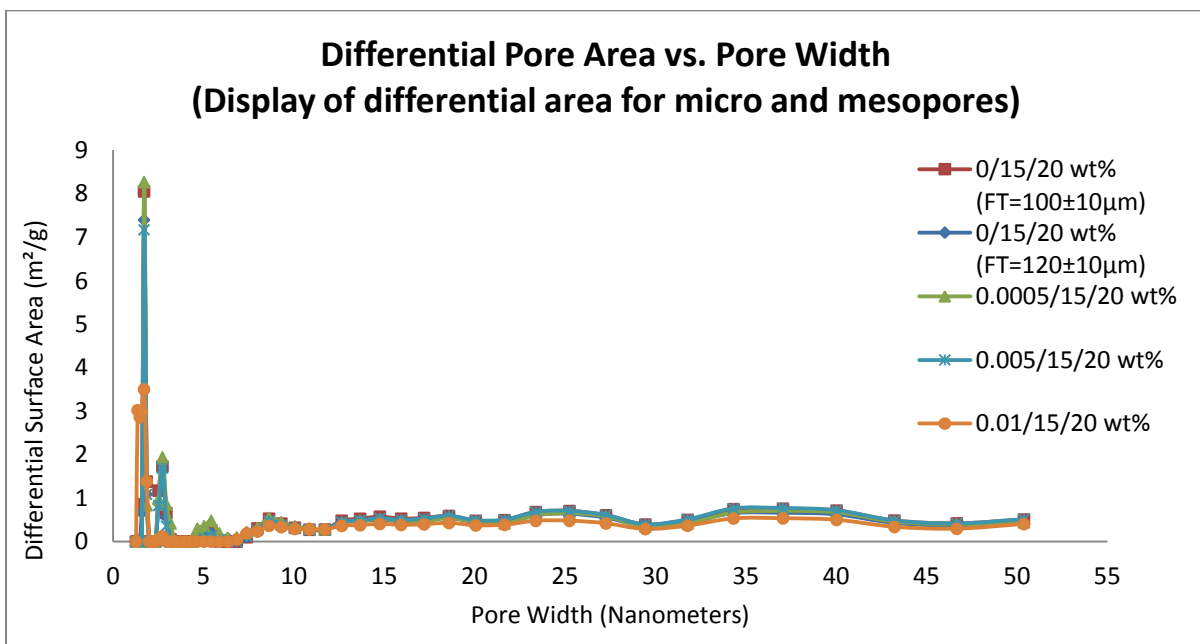


Figure 5.34 Plot of differential pore areas for micro and mesopores

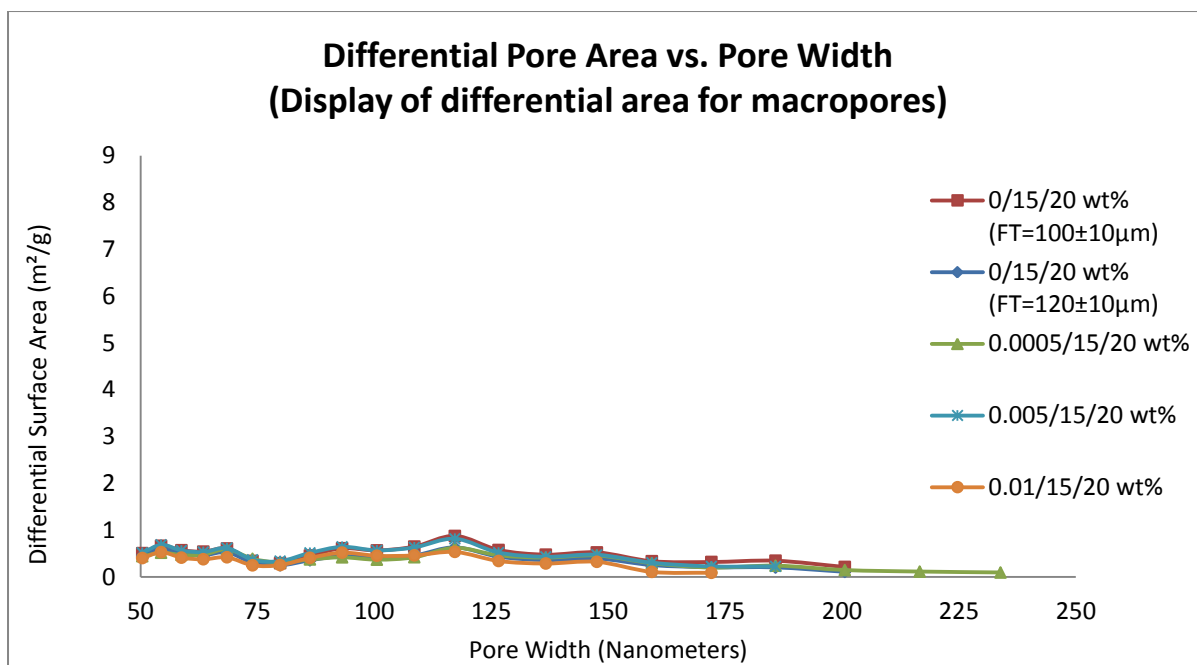


Figure 5.35 Plot of differential pore areas for macropores

On comparing the plots of pore width (pore diameter) vs. pore areas and vs. pore volumes, the results showed that the membranes featured micropores at 1.7 nm and very small mesopores at 2.7 nm. The total surface area of these pores is significant. It reached maximum values of about 8.3 m²/g and 1.7 m²/g respectively for membranes with no fNT content, as well as membranes with low fNT content (0.0005 wt%), and with the lowest values of about 3.5 m²/g and 0.12 m²/g respectively for membranes of highest fNT content (0.01 wt%). At the same time, these pores exhibited the smallest volumes (less than 0.008 cm³/g), only possible if their number was significant in comparison to larger mesopores (6-50 nm) and macropores (> 50 nm) in the membranes. On the other hand, the meso and macropores exhibited very low surface area values (less than 0.9 m²/g), with significant volumes reaching values of about 0.051 cm³/g. They generally fell with size values of about 18.5 nm, 25 nm, 40 nm, 54 nm, 68 nm, 93nm, 117 nm, 147 nm, and 185 nm with the pores of 117 nm being the most abundant.

To clarify the idea of small volume large surface area that the data showed, a calculation could be formulated for a membrane with two different sets of spherical pores with diameters of ~2 nm and ~100 nm, for example. Assuming that the volume of the ~2 nm pores was approximately half that of the ~100 nm pores, similar to the case of the 0.0005/15/20 wt% fNT/CA/H₂O membranes, a calculation of the ratio of the areas derived from the volumes for the two sets of pores would be as follows:

$$V_1 = \frac{4}{3} \pi r_1^3 n_1 \quad \forall \quad V_1 \text{ is the total volume of the } \sim 100 \text{ nm pores, } r_1 \text{ is the radius (half the given width for spherical pores), and } n_1 \text{ is the total number of the } \sim 100 \text{ nm pores}$$

$$V_2 = \frac{4}{3} \pi r_2^3 n_2 \quad \forall \quad V_2 \text{ is the total volume of the } \sim 2 \text{ nm pores, } r_2 \text{ is the radius (half the given width for spherical pores), and } n_2 \text{ is the total number of the } \sim 2 \text{ nm pores}$$

Assuming that the pore width is the diameter of the spherical pores:

$$\therefore V_1 = 2xV_2$$

$$\therefore \frac{4}{3}\pi r_1^3 n_1 = 2x \frac{4}{3}\pi r_2^3 n_2$$

$$\therefore 50^3 n_1 = 2x 1^3 n_2$$

$$\therefore \frac{n_1}{n_2} = \frac{1}{62500}$$

Now to calculate the ratio between the areas of the two sets of pores:

$$A_1 = 4\pi r_1^2 n_1 \quad \forall A_1 \text{ is the total area of the } \sim 100 \text{ nm pores}$$

$$A_2 = 4\pi r_2^2 n_2 \quad \forall A_2 \text{ is the total area of the } \sim 2 \text{ nm pores}$$

$$\therefore A_1 = XA_2$$

$$\therefore 4\pi r_1^2 n_1 = X \cdot 4\pi r_2^2 n_2$$

$$\therefore X = \frac{(r_1^2)n_1}{(r_2^2)n_2} = \frac{50^2}{62500} = \frac{1}{25}$$

$$\therefore A_1 = \frac{1}{25} A_2$$

$$\therefore A_2 = 25 A_1$$

From this calculation, the ~ 2 nm pores had ~ 25 times more area than the ~ 100 nm pores even though the latter occupied twice as much volume. However, the large numbers of the ~ 2 nm pores was reflected in the total area they possess. In reality, considering the pore volume and pore area plots of the 0.0005/15/20 wt% fNT/CA/H₂O membranes for example, the area of the ~ 2 nm pores is ~ 30 times more than that of the 100 nm pores, which was very close to the calculated values above.

From the calculation, a comparative interpretation could be done between the different nanocomposites' pores sizes and numbers. For pores smaller than 2 nm, the 0/15/20 wt%, 0.0005/15/20 wt%, and the 0.0005/15/20 wt% fNT/CA/H₂O had the largest quantity since their corresponding volumes were small but had huge areas per gram of the samples. As for the macrovoids, the areas they possessed were very small, indicating that their numbers per gram of the samples is very small. As for the 0.01/15/20 wt% fNT/CA/H₂O nanocomposite, its pores occupied the smallest areas, meaning it had the least number of pores than the rest of the samples most probably due to higher compaction.

Comparing the differential pore volumes and areas of the nanocomposite membranes with fNTs to the blank membrane of similar ICT (400 μ m), the overall pattern of variation was

found to be similar to that of the 0/15/20 wt% fNT/CA/H₂O blank membrane with FT = 100±10 μm.

5.3.2 Adsorption Isotherms

The adsorption isotherms of representative samples of the sets above were done to identify their types, and it was found that all samples could be classified as types I and IV. Figures 5.36 to 5.40 show the isotherms of the target membranes.

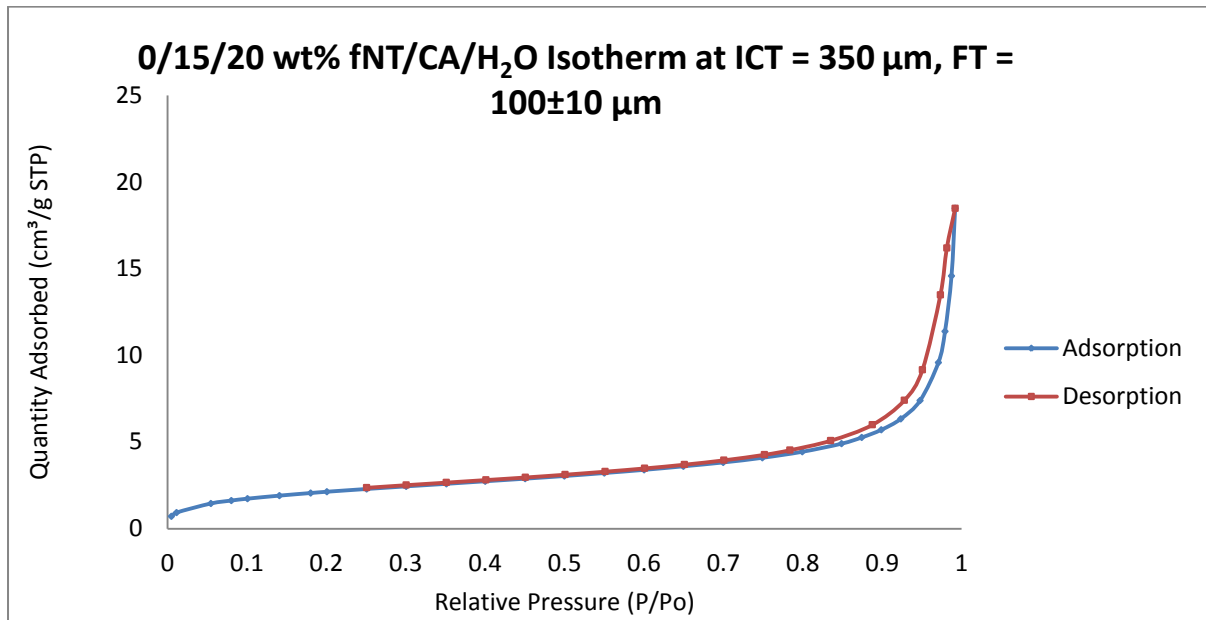


Figure 5.36 Adsorption isotherm of 0/15/20 wt% fNT/CA/H₂O at ICT = 350 μm and FT = 100±10 μm

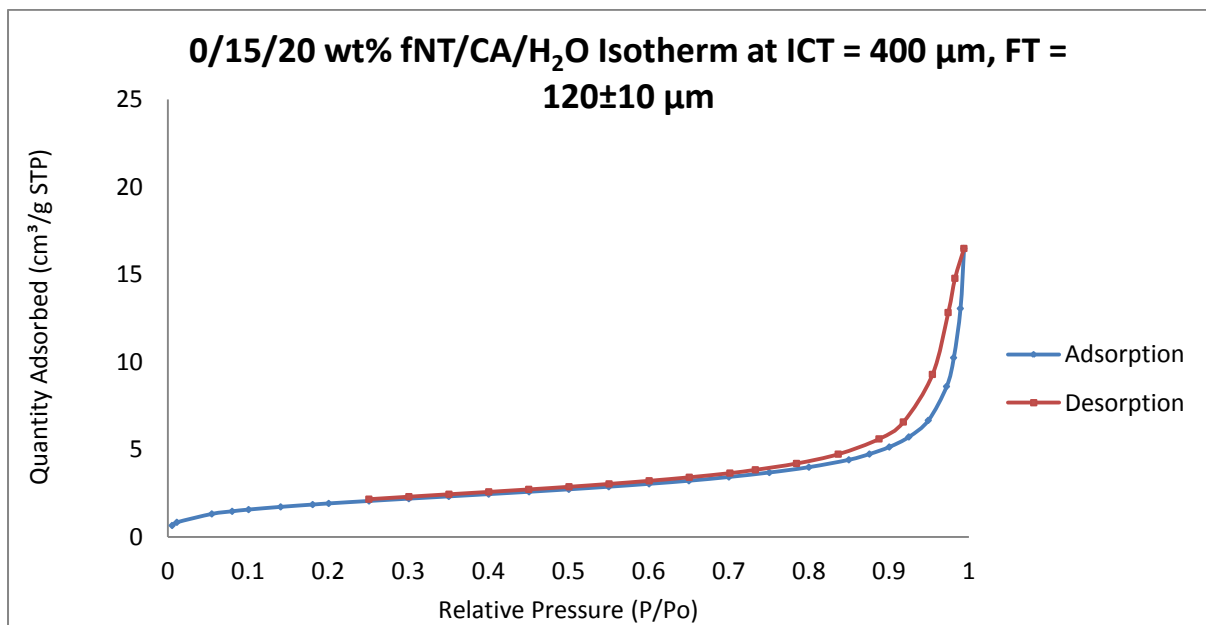


Figure 5.37 Adsorption isotherm of 0/15/20 wt% fNT/CA/H₂O at ICT = 400 μm and FT = 120±10 μm

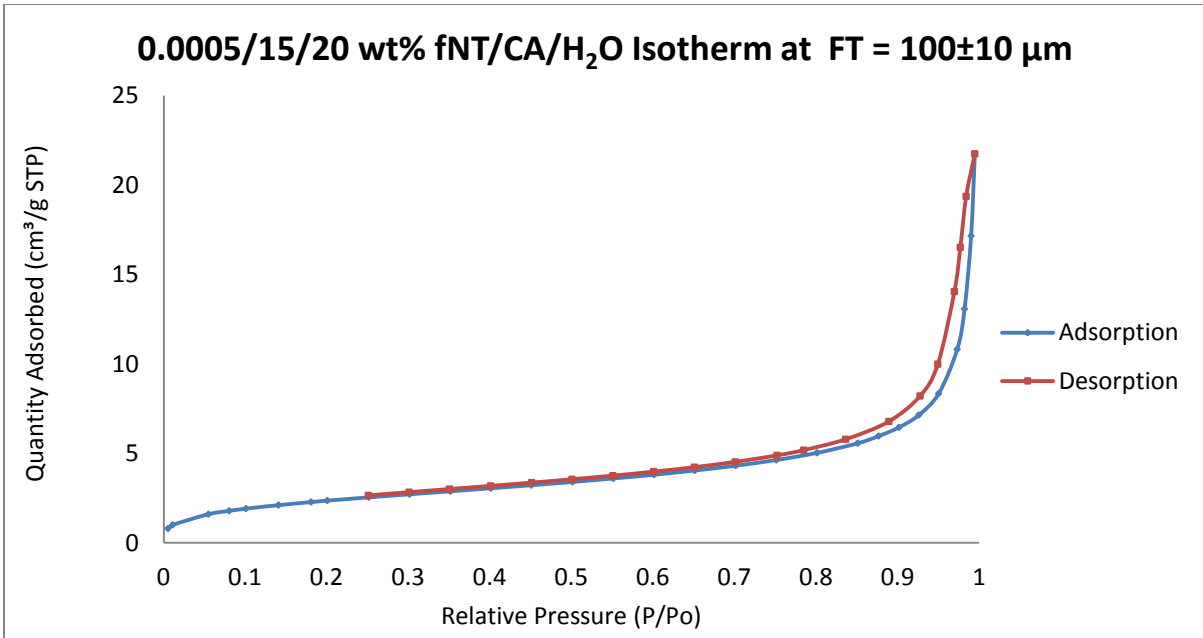


Figure 5.38 Adsorption isotherm of 0.0005/15/20 wt% fNT/CA/H₂O at ICT = 400 μm and FT = 100±10 μm

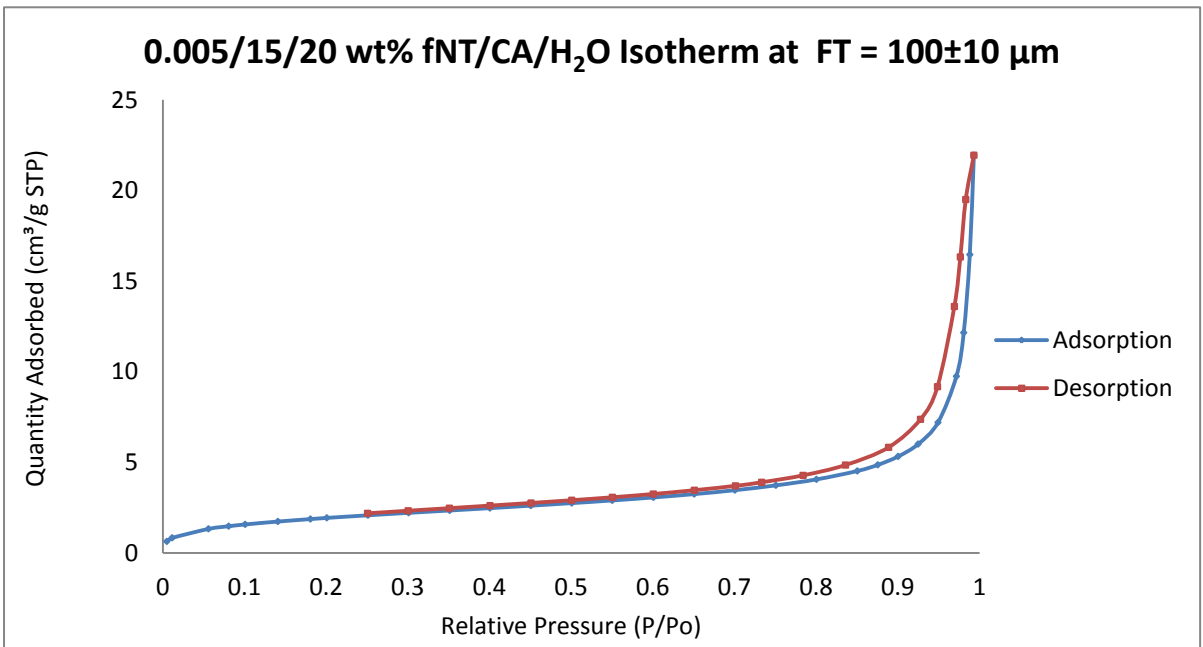


Figure 5.39 Adsorption isotherm of 0.005/15/20 wt% fNT/CA/H₂O at ICT = 400 μm and FT = 100±10 μm

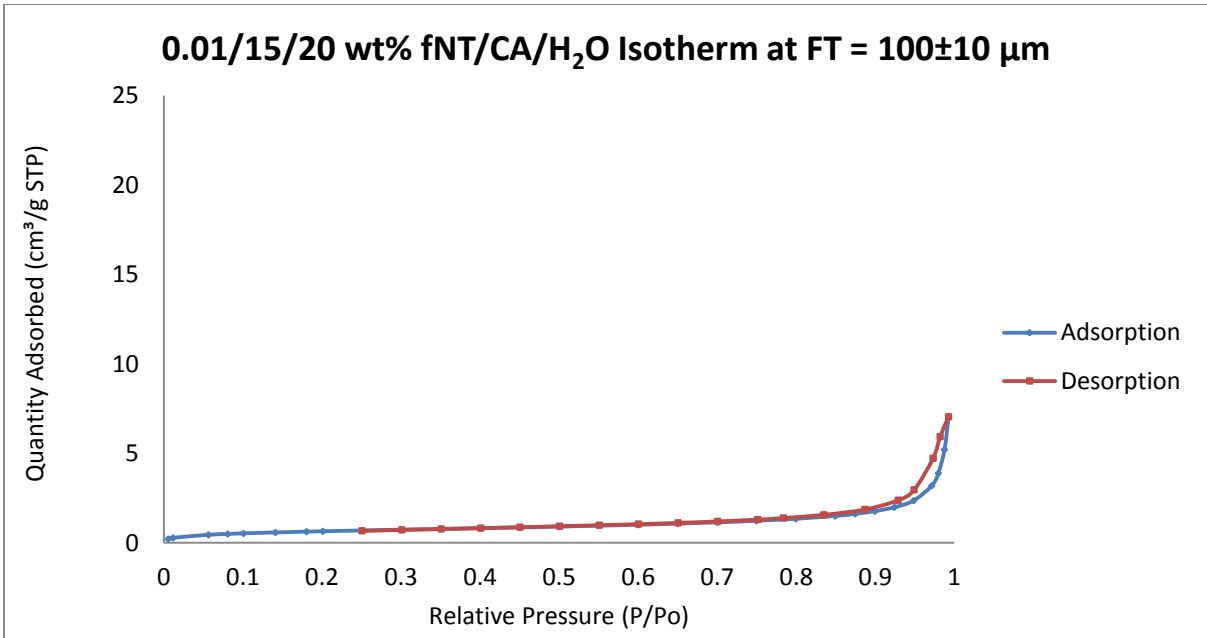


Figure 5.40 Adsorption isotherm of 0.01/15/20 wt% fNT/CA/H₂O at ICT = 400 μm and FT = 100±10 μm

5.3.3 The t-Plots

Using the t-plot method, the micropore volumes were calculated, and the external surface areas were evaluated. The idea is identifying the knee on the curve which forms a straight line that when extrapolated to the y-axis gives an intercept used in calculating the micropores volume. As for the region before the knee, it is used in calculating the total area occupied by the nitrogen monolayer adsorbed over the external surface area. Figures 5.41 to 5.45 show the t-plots of the representative samples per replica.

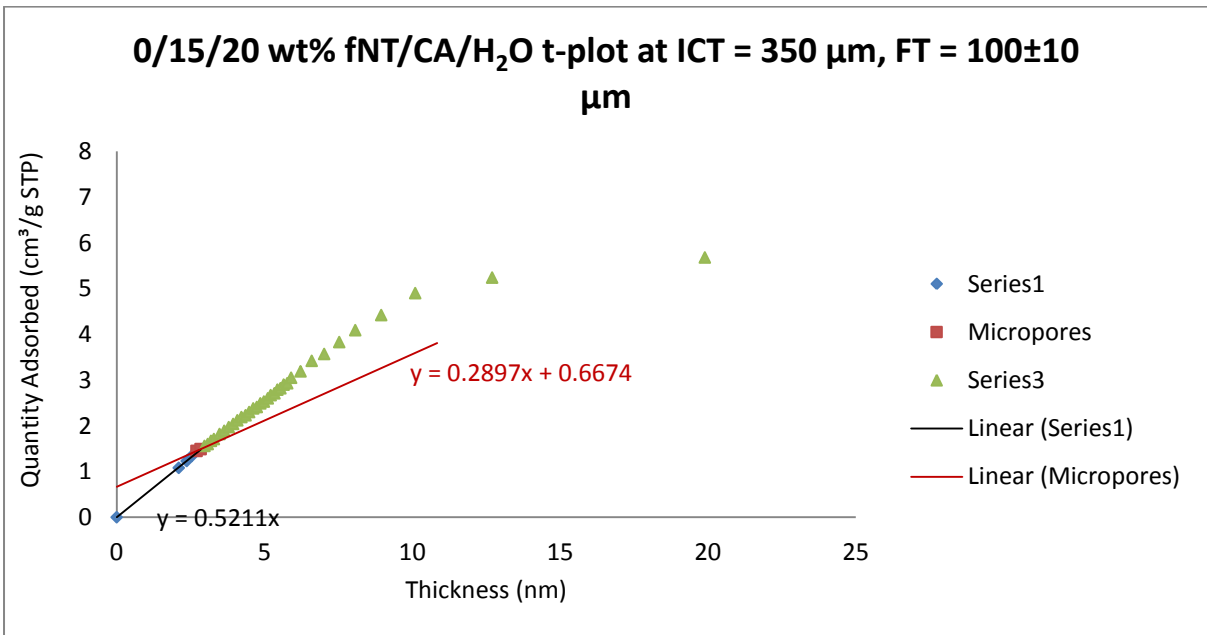


Figure 5.41 t- plot of 0/15/20 wt% fNT/CA/H₂O at ICT = 350 μm and FT = 100±10 μm

Calculated Area = 8.1 m²/g
 Micropores Volume = 1.3x10⁻³ ml/g

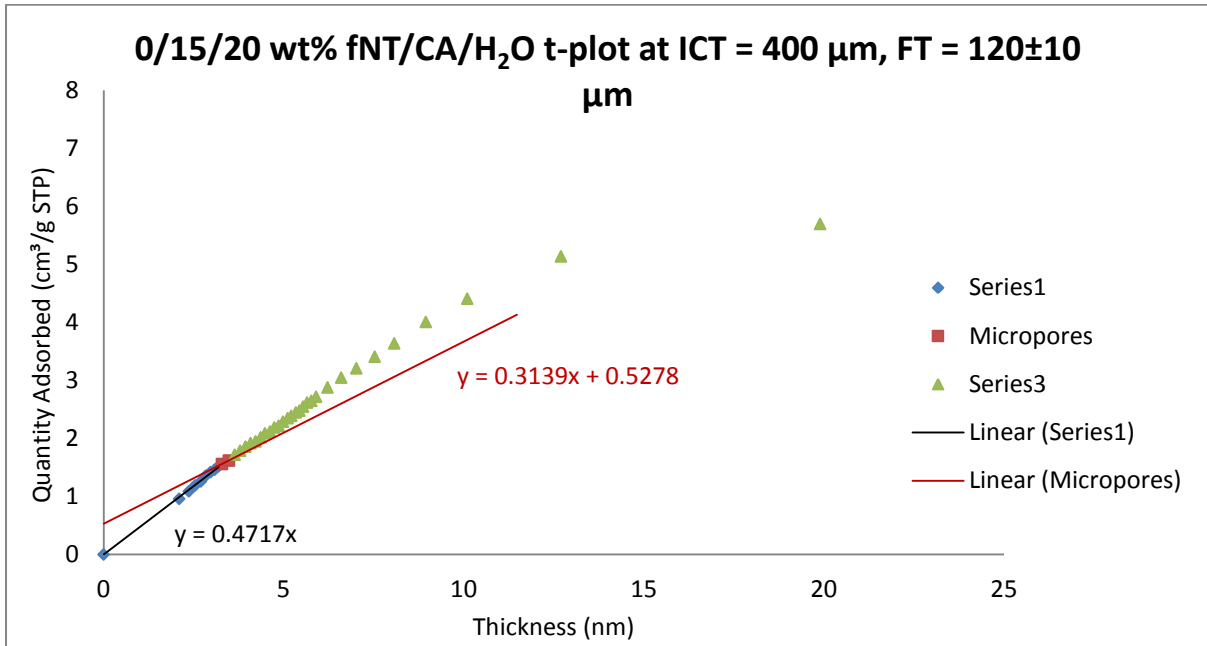


Figure 5.42 t- plot of 0/15/20 wt% fNT/CA/H₂O at ICT = 400 μm and FT = 120±10 μm

Calculated Area = 7.30 m²/g
 Micropores Volume = 8x10⁻⁴ ml/g

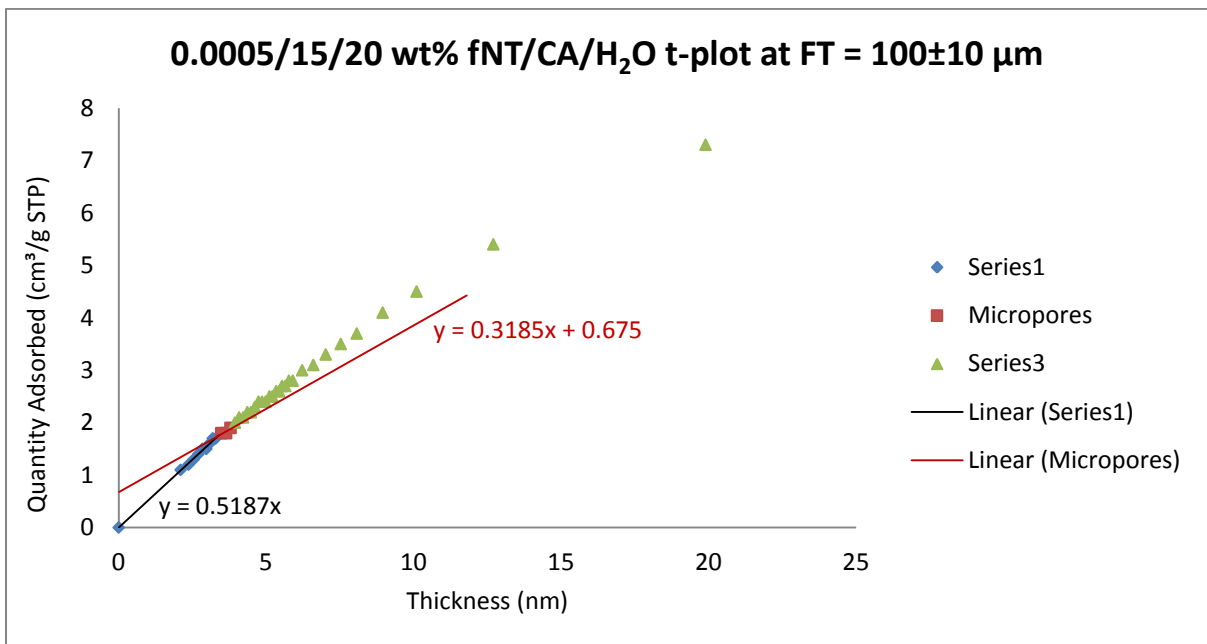


Figure 5.43 t- plot of 0.0005/15/20 wt% fNT/CA/H₂O at ICT = 400 μm and FT = 100±10 μm

Calculated Area = 8.03 m²/g
 Micropores Volume = 1.04x10⁻³ ml/g

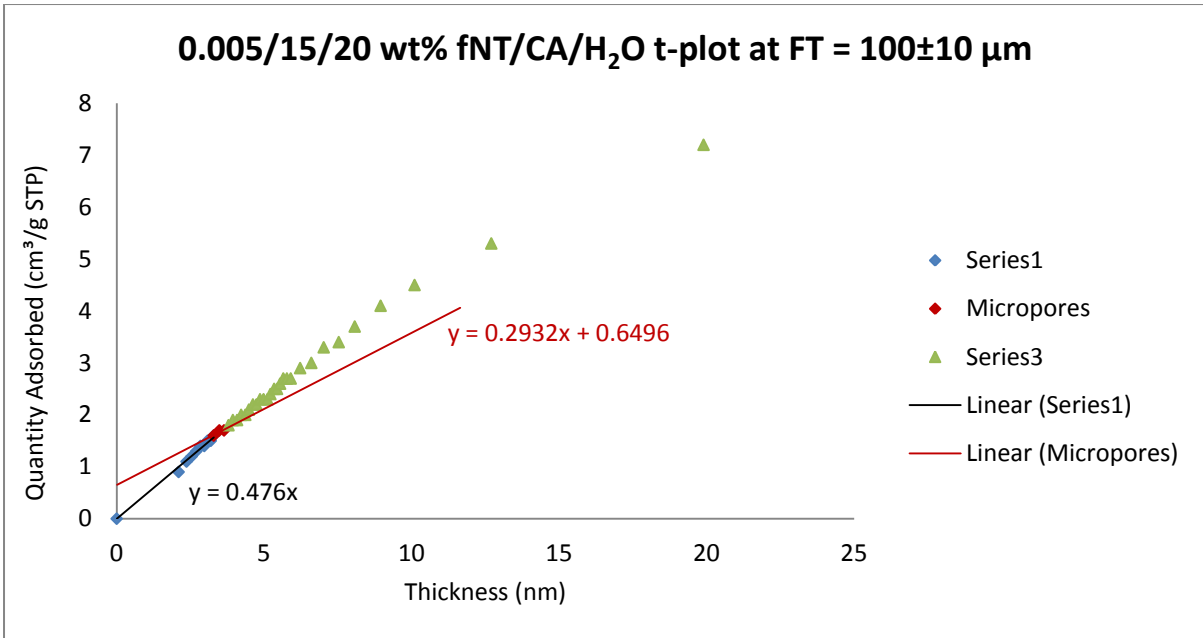


Figure 5.44 t- plot of 0.005/15/20 wt% fNT/CA/H₂O at ICT = 400 μm and FT = 100±10 μm

Calculated Area = 7.36 m²/g

Micropores Volume = 1.00x10⁻³ ml/g

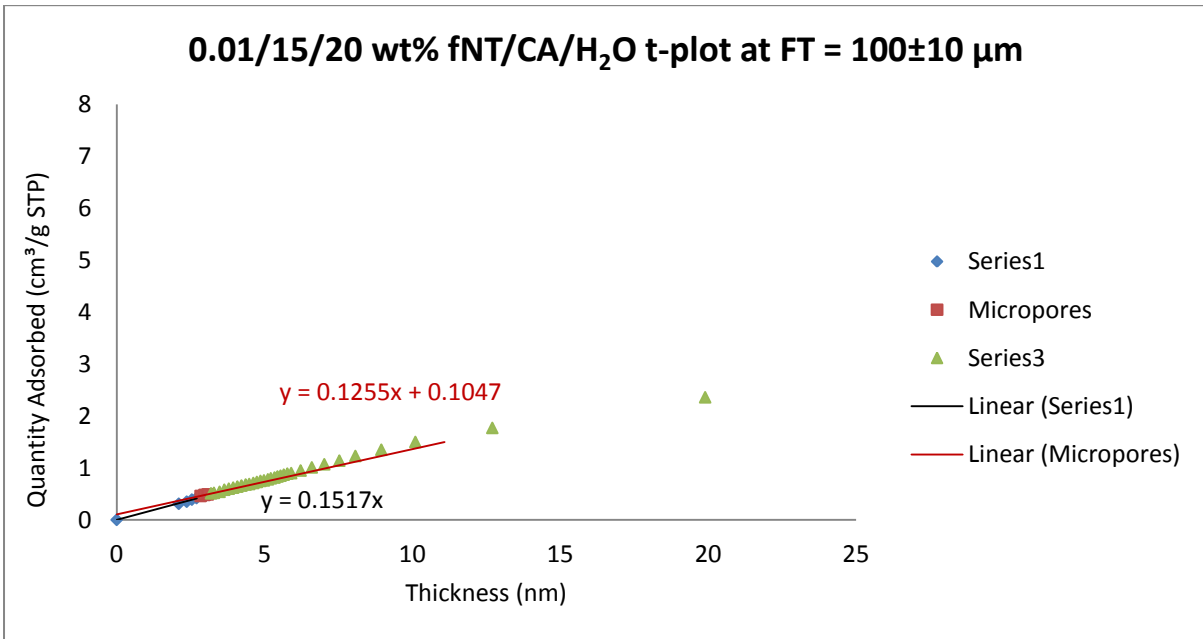


Figure 5.45 t- plot of 0.01/15/20 wt% fNT/CA/H₂O at ICT = 400 μm and FT = 100±10 μm

Calculated Area = 2.35 m²/g

Micropores Volume = 1.62x10⁻⁴ ml/g

To summarize the data above, Table 5.7 displays the external surface areas calculated using t-plot method, the volume of the micropores, as well as the BET surface area.

Table 5.7 Summary of surface area measurements, and micropores volumes

fNT/CA/H₂O wt%	0/15/20 (ICT = 350 μm)	0/15/20 (ICT = 400 μm)	0.0005/15/20	0.005/15/20	0.01/15/20
BET Area (m²/g)	7.77	7.11	8.68	7.07	2.33
t-plot Calculated Area (m²/g)	8.06	7.30	8.02	7.36	2.35
t-plot Micropores Volume (ml/g)	1.03x10 ⁻³	8.2x10 ⁻⁴	1.04x10 ⁻³	1.00x10 ⁻³	1.62x10 ⁻⁴

It is clear from the data that the addition of functionalized CNTs resulted in a general decrease in membrane surface area. This decrease became significant for CNTs content of 0.01 wt%. This is in line with the expected increased membrane compaction with CNT content and the decrease in porosity. The different absolute values of CA content in the membranes represented by the two blank samples 0/15/20 wt% ICT = 400 μm, FT = 120±10 μm, and ICT = 350 μm, FT = 100±10 μm, didn't seem to play any noticeable role in determining the surface micropore volume values of the nanocomposite membranes.

5.4 Membranes Performance

5.4.1 Permeation Rates

Permeation and salt retention rates for 15/20 wt% CA/H₂O membranes (ICT = 400 μm) having 0, 0.0005, 0.005, 0.01 wt% fNTs as nanofillers were measured using 1000 ppm NaCl solution in a pressurized water cell at 24 bars and room temperature. Figure 5.46 shows the significant increase (54.7%) in permeation rate due to the addition of only 0.0005 wt% fNTs vs. the 0/15/20 wt% fNT/CA/H₂O membrane (ICT = 350 μm). On increasing the nanotubes weight percentage to 0.005%, the rate slightly decreased compared to the 0.0005, yet, compared to the 0/15/20 wt% fNT/CA/H₂O membrane, the rate increased by 47.2%. The further increase in nanotubes weight percentage resulted in a sharp decrease in the permeation rate to become a little less than that of the 0/15/20 wt% fNT/CA/H₂O membrane (-3.8% decrease).

Figure 5.46 also shows a similar trend when comparing the nanocomposites to the blank 0/15/20 wt% fNT/CA/H₂O membranes (ICT = 400 μm), where a significant increase of 39% in permeation rate were reported for the 0.0005 wt% fNTs compared to the blank membrane. Increasing the nanotubes content to 0.005 wt% slightly decreased the rate compared to that of the 0.0005 wt% membranes. However, this rate compared to the blank membrane showed an increase by 32.2%. Further increase in fNT wt% (0.01 wt%) decreased the nanocomposite permeation rate to become a less than that of the blank membrane by 13.6 %.

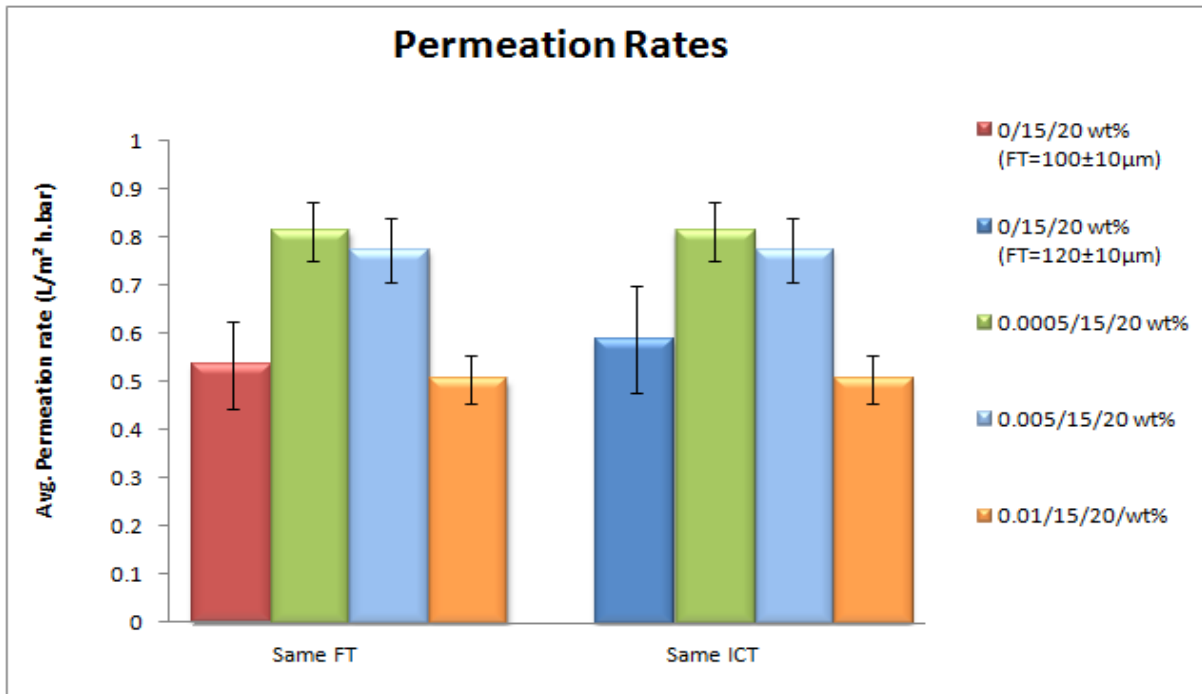


Figure 5.46 Plot showing the effect of fNTs on CA membrane permeation

5.4.2 Salt Retention Rates

Contrary to what other researchers have reported regarding the decrease in salt retention rates with the increase in permeation rates [2-3, 7-8], salt retention rates were not significantly affected by the addition of 0.0005 and 0.005 wt% fNTs when compared to the 0/15/20 wt% fNT/CA/H₂O membrane at the same final thickness, where a slight decrease in the salt retention was noticed for both fNTs contents (-6% and -6.8% respectively). The further addition of fNTs (0.01 wt%), however had a noticeable negative effect on the nanocomposite retention rate by 52.9% as displayed in Figure 5.47. A similar trend can be observed when comparing the nanocomposites to blank CA membranes prepared at the same ICT of 400 µm.

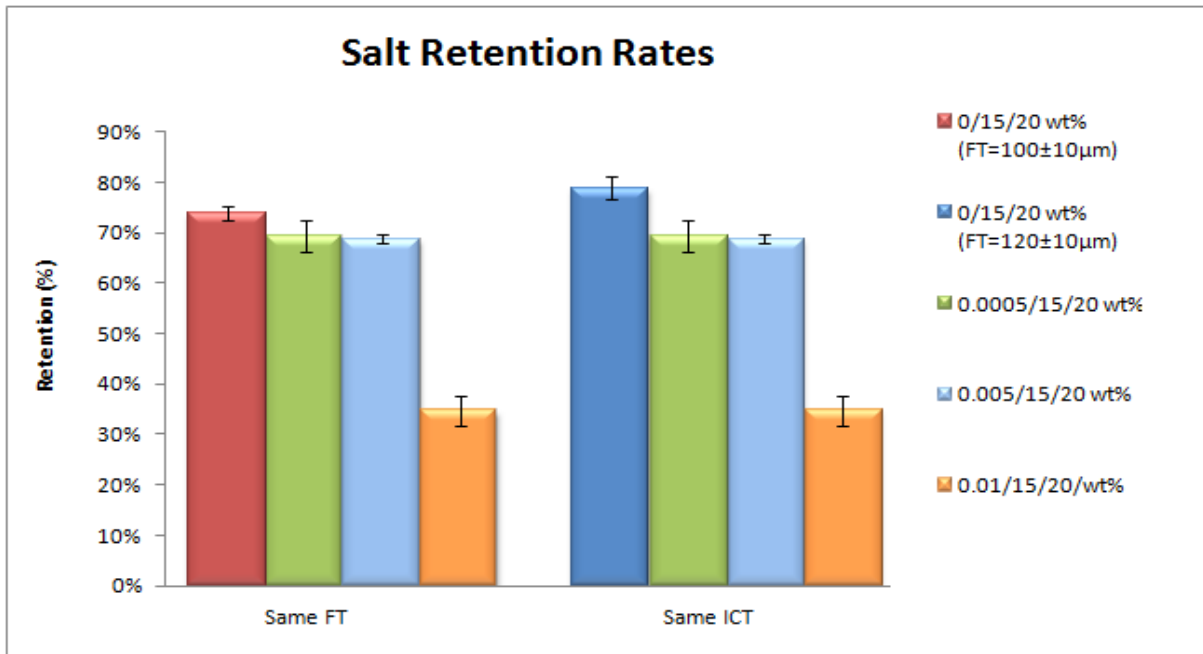


Figure 5.47 Plot showing the effect of fNTs on CA membrane salt retention rates

On comparing the overall membranes' performance using both permeation and salt retention rates, Figure 5.48 displays the enhanced permeation rate with the minor drop in salt retention rate of the 0.0005/15/20 and 0.005/15/20 wt% fNT/CA/H₂O membranes when compared to the two blank 0/15/20 wt% fNT/CA/H₂O membranes and the 0.01 wt% fNT/CA membranes. Accordingly, the 0.0005/15/20 wt% fNT/CA/H₂O nanocomposite was found to be the best performing membrane.

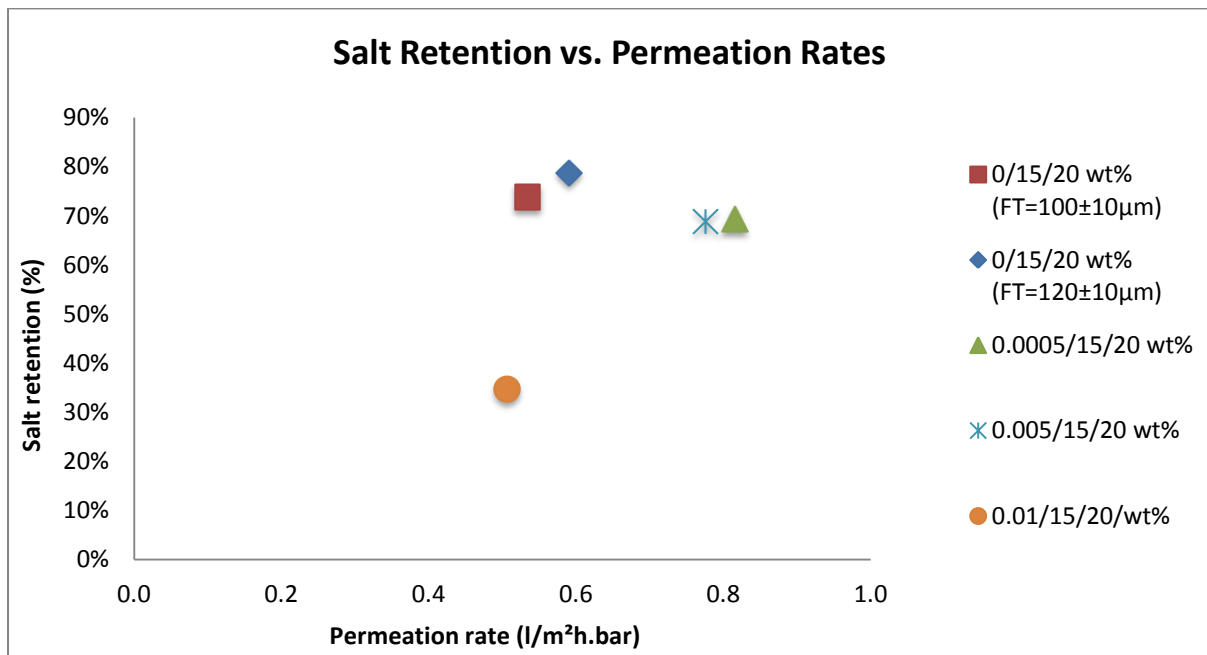


Figure 5.48 Representation of the effect of functionalized fNTs addition on the membrane overall performance at same FT

5.4.3 BET Surface Areas

CA membranes surface area varied according to the fNTs content as displayed in Figure 5.49. The addition of only 0.0005 wt% fNTs had an insignificant effect on the surface area when compared to the blank 0/15/20 wt% fNT/CA/H₂O membranes at the same final thickness ($8.07 \pm 1.19 \text{ m}^2/\text{g}$ vs. $7.96 \pm 0.51 \text{ m}^2/\text{g}$ respectively). Further increase in the nanofiller content started decreasing the surface area to become $7.29 \pm 0.76 \text{ m}^2/\text{g}$, where a sharp decrease is observed on the addition of 0.01 wt% fNTs to become $4.06 \pm 2.11 \text{ m}^2/\text{g}$. The same trend can be observed when comparing the nanocomposites surface areas to the other blank 0/15/20 wt% fNT/CA/H₂O membranes (ICT = 400 μm).

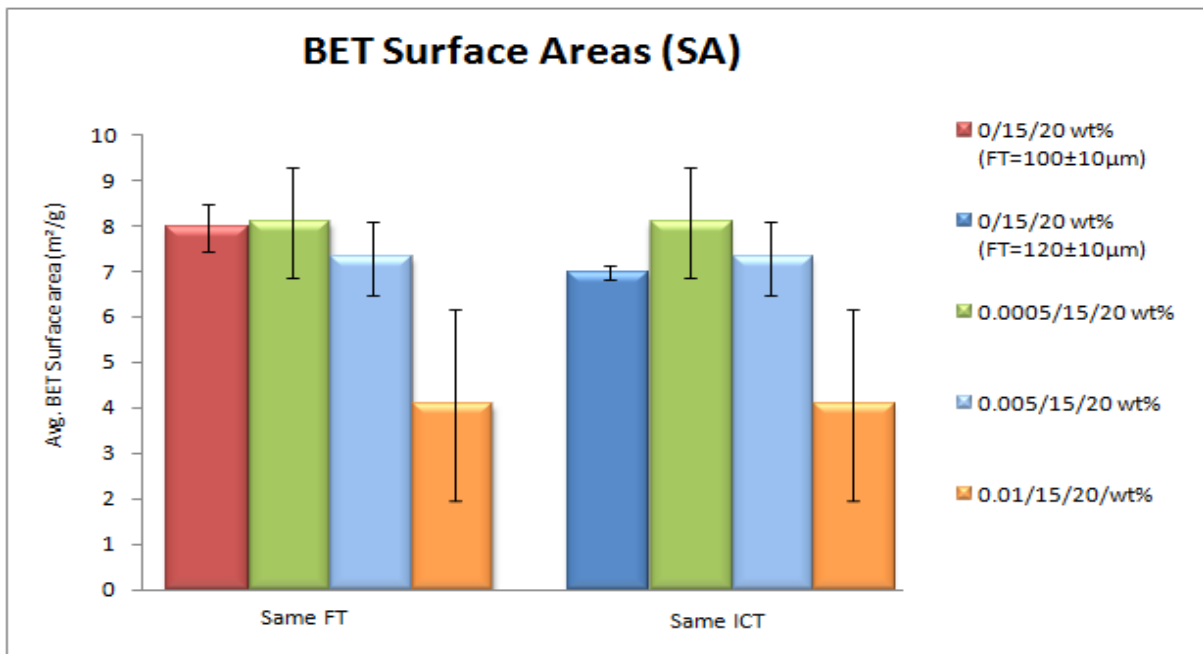


Figure 5.49 Plot showing the effect of different wt% of fNTs on CA membranes surface area

On comparing the overall membranes' performances under the effect of pores' surface area, Figure 5.50 shows that for the 15 wt% CA membranes, although there is a little change in the surface area between the two blank 0/15/20 wt% fNT/CA/H₂O membranes and the 0.0005 and 0.005 wt% fNTs-CA nanocomposites, permeation rates for both nanocomposites increased. As for the 0.01 wt% fNT-CA nanocomposite, although there is a significant decrease in its surface area in comparison to the rest of the 15 wt% CA membranes, it still had a permeation rate comparable to both blank 0/15/20 wt% fNT/CA/H₂O membranes.

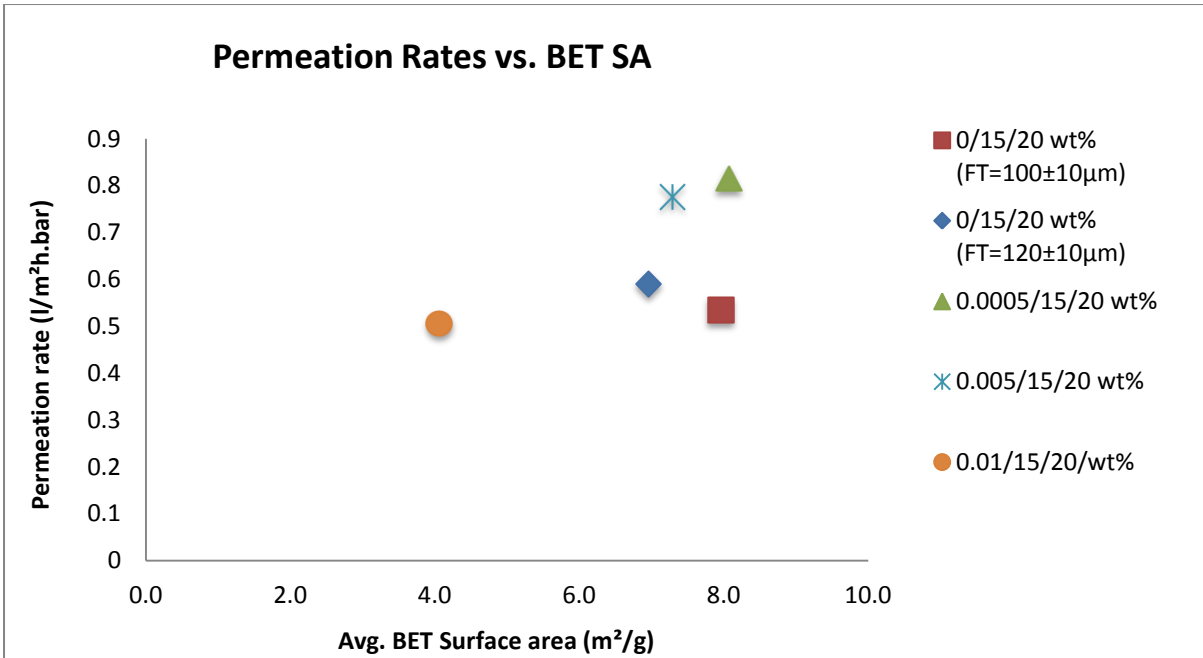


Figure 5.50 Representation of the effect of surface area on the membranes permeation rates

On comparing the overall membranes salt rejection rates in relation to membranes surface area, Figure 5.51 shows that for the 15 wt% CA membranes, the little change in the surface areas of the 0.0005 and 0.005 wt% fNTs CA nanocomposites when compared to both the 0/15/20 wt% fNT/CA/H₂O membranes had a little change in salt rejection rates. The 0.01/15/20 wt% fNT/CA/H₂O membranes behaved differently because the pores surface area decreased leading to a decrease in salt retention.

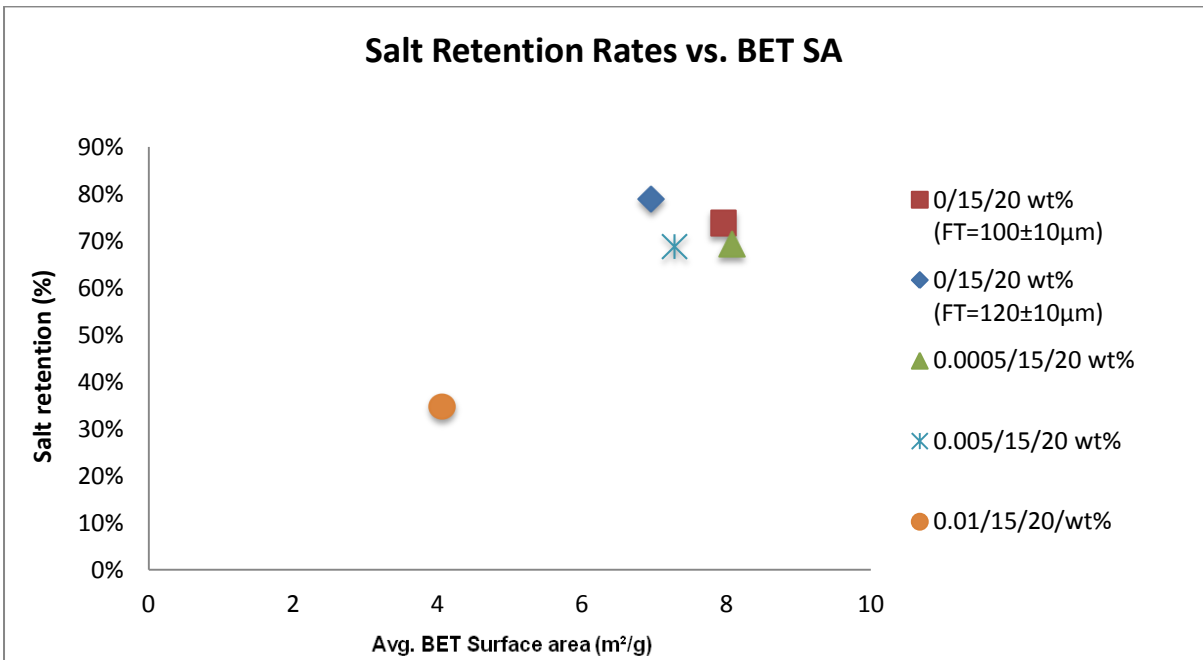


Figure 5.51 Representation of the effect of surface area on the membranes salt retentions

5.4.4 Membrane Morphology and Performance: General Discussion

Table 5.8 summarizes the data for permeation rates, salt retentions, and surface areas with the change in CNT content. Tables 5.9 and 5.10 have the calculated variation in percentages for the same samples due to the mentioned effects to clarify the change in membrane performance.

Table 5.8 Effect of fNTs wt% on permeation, salt retention, and surface area, rate measurements are for 15/20 wt% CA/H₂O membranes using 1000 ppm NaCl solution at 24 bars and room temperature

CA wt%	ICT (μm)	FT (μm)	Additive(s)	Additive %	Permeation rate (L/m ² h.bar)	Avg. Permeation rate (L/m ² h.bar)	Salt retention %	Avg. Salt retention %	BET Surface area (m ² /g)	Avg. BET Surface area (m ² /g)	Name Displayed on Charts
15%	350	~100±10	Water	20%	0.63	0.53 ± 0.088	73.52%	73.82 ± 1.39	8.54	7.96±0.51	0/15/20 wt% fNT/CA/H ₂ O (Blank 1)
					0.53		72.60%		7.57		
					0.45		75.34%		7.77		
15%	400	~120±10	Water	20%	0.62	0.59 ± 0.11	80.56%	78.82±2.26	6.80	6.96±0.16	0/15/20 wt% fNT/CA/H ₂ O (Blank 2)
					0.68		79.63%		6.97		
					0.47		76.26%		7.11		
15%	400	~100±10	CNTs + Water	0.0005% +20%	0.83	0.82 ± 0.057	69.40%	69.37±2.85	6.70	8.07±1.19	0.0005/15/20 wt% fNT/CA/H ₂ O
					0.86		66.50%		8.69		
					0.75		72.20%		8.83		
15%	400	~100±10	CNTs + Water	0.005% + 20%	0.72	0.78 ± 0.067	69.20%	68.80±1.35	6.66	7.29±0.76	0.005/15/20 wt% fNT/CA/H ₂ O
					0.75		69.90%		7.07		
					0.85		67.30%		8.13		
15%	400	~100±10	CNTs + Water	0.01% + 20%	0.55	0.51 ± 0.047	34.48%	34.75±0.30	6.41	4.06±2.11	0.01/15/20 wt% fNT/CA/H ₂ O
					0.46		35.07%		3.45		
					0.51		34.70%		2.33		

Table 5.9 Calculated change in permeation rates and salt retention rates at same membrane final thickness

Name Displayed on Charts	Avg. Permeation rate (L/m ² h.bar)	Change in Avg. Permeation vs. Blank 1	Avg. Salt retention %	Change in Avg. Salt Retention vs. Blank 1
0/15/20 wt% fNT/CA/H ₂ O (Blank 1)	0.53 ± 0.088	-----	73.82 ±1.39	-----
0.0005/15/20 wt% fNT/CA/H ₂ O	0.82 ± 0.057	54.7%	69.37±2.85	-6.0%
0.005/15/20 wt% fNT/CA/H ₂ O	0.78 ± 0.067	47.2%	68.80±1.35	-6.8%
0.01/15/20 wt% fNT/CA/H ₂ O	0.51 ± 0.047	-3.8%	34.75±0.30	-52.9%

Table 5.10 Calculated change in permeation rates and salt retention rates at same membrane initial casting thickness

Name Displayed on Charts	Avg. Permeation rate (L/m ² h.bar)	Change in Avg. Permeation vs. Blank 2	Avg. Salt retention %	Change in Avg. Salt Retention vs. Blank 2
0/15/20 wt% fNT/CA/H ₂ O (Blank 2)	0.59 ± 0.11	-----	78.82±2.26	-----
0.0005/15/20 wt% fNT/CA/H ₂ O	0.82 ± 0.057	39.0%	69.37±2.85	-12.0%
0.005/15/20 wt% fNT/CA/H ₂ O	0.78 ± 0.067	32.2%	68.80±1.35	-12.7%
0.01/15/20 wt% fNT/CA/H ₂ O	0.51 ± 0.047	-13.6%	34.75±0.30	-55.9%

The first point to consider in permeation rates was having a steady rate at an acceptable pressure range. Many membranes with different conditions were tested to evaluate their steady flow rate. The pressure range tested varied from 8 bars all the way to 55 bars. According to literature, CA membranes usually can handle a range of 15-30 bars, beyond which the membranes are damaged under the effect of compaction [47]. This was verified for all the membranes reported in Appendix I. They were damaged due to high pressure. Membranes that performed well, on the other hand, showed a steady flow rates at 24 bars, which lies in the range mentioned in the literature [47].

Comparing the permeation rates of the 0/15/20 wt% fNT/CA/H₂O membranes (FT = 100±10 μm) to the 0.0005/15/20 wt% fNT/CA/H₂O and 0.005/15/20 wt% fNT/CA/H₂O

membranes show that the minor addition of fNTs to CA matrix increased the solution permeation rate even though the fNTs decreased the number of the 93 nm, 117 nm, and 143 nm pores, as demonstrated by the decrease in their surface area and volume, while having a lesser effect on meso and micropores (Figures 5.31, 5.32, 5.34, and 5.35) This suggests that the nanotubes could have created connection channels between the pores, thus enhancing the flow rates. This can also be supported by the interpretation of molecular dynamics simulation of water passage within CNTs, since the hydrophobic channels are expected to enhance permeation rates. The fact that the channels didn't significantly affect the pores surface area justifies the claim that the permeate might have used the new available route, and moved faster than within the 0/15/20 fNT/CA/H₂O membranes. However, MD simulations suggested that after a certain nanotube diameter, the permeate wouldn't sense the effect of the hydrophobic channels, and wouldn't experience the *drift like* motion [77]. This could explain why the increase in the NaCl solution permeation rate for the 0.0005/15/20 wt% fNT/CA/H₂O and 0.005/15/20 wt% fNT/CA/H₂O membranes wasn't several orders of magnitude higher than usual.

Interpreting the permeation rates for the 0.005/15/20 wt% and the 0.0005/15/20 wt% membranes, however, raises a question. Even though the former has more fNTs content, and has higher meso and macropores volume and area than the latter, it still exhibits less permeation rate. This could be clarified from the BET surface area and the t-plot surface area calculations of both as in Table 5.7. According to the data, the 0.005/15/20 wt% membranes have an overall surface area that is less than that of the 0.0005/15/20 wt% membranes, which means that the former membrane is more compact than the latter. Though this was not reflected in the size and number of large meso and macropores, it was reflected in the reduction of the volume, area, and consequently the number of the mesopores with diameters less than 12 nm, as well as in the volume, area, and number of micropores as shown in Figures 5.31 and 5.34. This in turn affected the permeation rate with the small difference shown in Figure 5.50.

Another factor affecting permeation rate is the fact that the fNTs are expected to have enhanced the hydrophilic property of the two nanocomposites due to the existence of the polar functional groups on the nanofiller walls. This is thought to play a role in improving the permeation rates since it facilitates the polar solvent (water in this case) to move inside the matrix faster than for the blank CA matrix. This was suggested by Choi et al. [38] on studying the effect of the addition of fNTs to PSF membranes.

On the other hand, the noticeable decrease in permeation rate of the 0.01/15/20 wt% fNT/CA/H₂O membrane can be related to the significant decrease in the membrane porosity, as reflected by the decrease in pore surface area, pore volume, as well as the overall membrane surface area (Figure 5.50). This was clear in the membrane SEM image in Figure 5.29, and clear in the porosity results in Figures 5.30 and 5.33, where the high content of fNTs compacted the overall pore surface area of the membrane such that the meso and macropores needed to facilitate high permeation rates decreased in size and numbers. Adding

to this, the high content of the fNTs could have blocked the existing pores, as suggested by Tang et al. [40].

Further interpretation of the plot representing permeation rates and the plot representing the relation between surface area and permeation (Figures 5.46 and 5.50) again supports the postulation that the nanotubes created alternative channels for water passage. The 0.01/15/20 wt% fNT/CA/H₂O membranes permeation rate was still comparable to the blank 15/20 wt% CA/H₂O membrane (at the same final thickness) even though the pores surface area of the former is approximately half that of the latter. This implies that water permeation through the nanocomposite membrane was dependent on the effect of CNTs, as well as membrane porosity.

It is worth mentioning that interpretation of the performance of the 0/15/20 wt% fNT/CA/H₂O membranes with ICT of 400 μm and final thickness of 120 ± 10 μm in comparison with the 0.0005/15/20 wt% and 0.005/15/20 wt% fNT/CA/H₂O nanocomposites is thought to be dependent on both the presence of the fNTs, in parallel with the available macro, meso, and micropores. Even though the surface areas of the three membranes are very close (Figure 5.49), the minor increase in the surface area associated with the nanotubes channels of both nanocomposites increased their permeation rates relative to the 0/15/20 wt% membrane as shown in Figure 50. As for the behavior of the 0.01/15/20 wt% fNT/CA/H₂O nanocomposites performance in comparison to the 0/15/20 wt% fNT/CA/H₂O membrane (ICT = 400 μm), the presence of the fNTs didn't enhance the permeation, but rather decreased it by only 3.8% (Table 5.10). This is because the available surface area in the former is half the latter (Figure 5.49). Thus, one of the permeate routes is blocked (the pores) even though the second route (the nanotubes) is used.

Interpretation of the salt retention rates of the 0.0005/15/20 wt% and 0.005/15/20 wt% fNT/CA/H₂O membranes show that the new channels created by the fNTs didn't allow larger quantities of NaCl molecules to pass through when compared to the salt retention rates of the 0/15/20 wt% fNT/CA/H₂O membranes (FT = 100 ± 10 μm) (Figure 5.47). This doesn't seem to agree with what MD simulations suggest, since the large diameter of the nanotubes used in the experiments were expected to allow the passage of ions freely [64, 68]. The results are promising because the addition of small amounts of functionalized CNTs had a good effect on permeation rates without altering salt retention to a significant effect. On the other hand, salt retention seems to be more dependent on membrane porosity, particularly small pores (<6 nm). This can be verified from the salt retention data when compared to porosity data (Figures 5.47, 5.31 and 5.34), where salt retention exhibit small decreases with the addition of fNTs to the membranes as long as the number of small pores is not noticeably reduced (observed salt retention decreases are about 6% and 7% for the 0.0005 wt% CNT and the 0.005 wt% CNT respectively).

The 0.01/15/20 wt% fNT/CA/H₂O nanocomposite salt retention rate, however, was the most unexpected because on comparing it to the 0/15/20 wt% fNT/CA/H₂O membranes, the former has less small pores within the same FT (Figures 5.31 and 5.34). Furthermore, the

former was cast with an ICT of 400 μm to reach the same final thickness as the latter which was cast at ICT = 350 μm , thus it is expected to have more dense polymer layers than the latter (more absolute CA content). At the same time, the two membranes have approximately the same permeation rates (Figure 5.46). Still, the 0.01/15/20 wt% fNT/CA/H₂O nanocomposite salt retention was reduced by more than 50% compared to the 0/15/20 wt% fNT/CA/H₂O membranes (Table 5.10 and Figure 5.47). This behavior could be explained by considering several things. The first is by looking at the micropores and small mesopores (<6 nm) size distribution in Figures 5.31 and 5.34, their sizes and numbers decreased significantly. This can also be supported by the calculated micropores' volumes using the t-plot in table 5.7. The second parameter that could have contributed to this is the possibility that the nanotubes acted as passage routes for the entering salt since there wasn't enough micropores to screen off the salt, which actually agrees with what MD simulations suggests [64]. Last, although the mesopores and macropores are less in number compared to the 0/15/20 wt% fNT/CA/H₂O membranes, water permeation is more prominently taking place through them or through the nanotubes, both of which are less effective in salt retention, leading to the significant decrease in salt retention values obtained.

6 Conclusions

6.1 Conclusion

Having investigated the effects of membranes thickness, CA contents, PI temperature, solvent evaporation, H₂O addition, and CNTs addition, the following conclusions can be drawn.

1. ICT strongly affects voids formation: where the thicker the membrane, the larger the voids. Below a critical thickness, macrovoids are unable to develop probably because the membranes are too thin for nucleation expansion to take place. ICT also affects macrovoids shapes and depth within the membranes.
2. The increase in coagulation bath temperature during membrane PI increased macrovoids sizes, which agrees with literature. However, the shapes and sizes of the macrovoids were found to be dependent of CA content as well.
3. The decrease in CA content increases the macrovoids size. However, decreasing CA content was found to have a limited range because of its effect on the cast solution viscosity. The 13 wt% CA membranes, though having large macrovoids in comparison to the 15 and 17 wt% CA membranes, were found to be non-reproducible in their final thicknesses or morphology. This is also thought to be due to the low viscosity of the cast solution.
4. The main aim of solvent evaporation was to decrease the pores sizes on the top layer of the membrane so that in salt retention tests, the membranes would perform better. Both trials for solvent evaporation (either prior to PI or post incomplete PI) had negatively affected the macrovoids structure, where they decreased in size. A main factor to consider is the high volatility of the acetone solvent used, which could explain the dramatic decrease in macrovoids sizes.
5. The addition of a non-solvent during stock preparation became essential to create large macrovoids especially for the 15 and 17 wt% CA membranes. Different water amounts were tried (5, 10, 15, and 20 wt%), all of which were successful in creating large macrovoids with the increase in water content. Beyond 20 wt% though, having a homogenous stock solutions was unsuccessful since the amount of non-solvent added precipitated the CA in the stock solution creating gelatinous like bulky particles.
6. MWCNTs' addition, both pristine and functionalized, had a compaction effect on membrane morphology. The amount of compactness depended on both the quantity of the nanotubes and how well dispersed they were throughout the membranes. *Agglomeration* was a main issue for pNTs since it was very challenging to disperse them into the hydrophilic medium of the CA matrix. Resorting to functionalization of the nanotubes became a must.
7. MWCNTs functionalization was successful. This facilitated nanocomposites preparation as fNTs dispersion.

8. The proper random dispersion of fNTs showed that networks of fNTs spread throughout the CA matrix with no detectable agglomerates. This was due to the polar graphene walls that enhanced the interaction between the nanofiller and the polymer matrix at the interface. The interaction effect was clear in the decreased number of macrovoids as the wt% of fNTs increased. This is thought to be due to the fact that fNTs presence decreased the rate of the demixing process during PI.
9. Porosity analysis showed that for the fNTs nanocomposites, the increase in fNTs content was associated with a general decrease in pores surface areas relative to the 15/20 wt% CA/H₂O membranes with the same final thickness. This led to a small decrease in salt retention rates. However the permeation rates increased with the increase in the fNTs content until a flipping point at which it decreased again. This is believed to be due to the nanotubes opening new channels for the permeate to pass through along with the existing pores.
10. Porosity analysis showed that fNTs nanocomposites cast with the same ICT as a 15/20 wt% CA/H₂O membranes don't differ significantly, yet their permeation rates were generally higher (except for one), and their salt retention were lower. This lead to a more belief that the permeate passage is not only through the available pores but rather through a parallel route via the nanotubes.

6.2 Future Work

As a continuation for this project, several aspects could be carried out in the future:

- Investigating the possibility of using MWCNTs of different dimensions (aspect ratios, length, and diameter)
- Investigating the effect of SWCNTs addition to CA membranes and their effect on membrane performance and morphology
- Investigating the effect of using a different solvent (like acetic acid) on the nanocomposites performance and morphology
- Investigating the effect of using a pore former on the nanocomposites performance and morphology
- Investigating the effect of lowering the PI coagulation bath temperature to 4°C, and having an annealing step at high temperatures added to the preparation procedure
- Investigating different types of functionalization for MWCNTs, making them more ions selective, thus developing more specialized nanocomposites

- Investigating the nanocomposites performance with real brackish water from open water sources in Cairo or Giza premises, and measuring the nanocomposites rejection rates for different salts
- Investigating different fouling effects on membrane performance

References

1. **Search for Clean Water Continues**
[http://www.nesc.wvu.edu/old_website/ndwc/ndwc_dwh_1.html]
2. Ridgway H: **Membrane Separation...Basics**. In: *Advanced Membrane Technologies*. Stanford University; 2008.
3. **Desalination History**
[<http://www.water.vic.gov.au/programs/desalination/desalination/desalination-history>]
4. **The History of Desalination** [<http://www.rpi.edu/dept/chem-eng/Biotech-Environ/Environmental/desal/history.html>]
5. Henthorne L: **The Current State of Desalination**. In: *2009; Dubai*: International Desalination Association; 2009.
6. Yangali-Quintanilla V, Li Z, Valladares R, Li Q, Amy G: **Indirect desalination of Red Sea water with forward osmosis and low pressure reverse osmosis for water reuse**. *Desalination*, In Press, Corrected Proof.
7. **Water crisis hits Egypt "Country of Nile River"**
[<http://news.egypt.com/en/20070724293/news/-egypt-news/water-crisis-hits-egypt-country-of-nile-river.html>]
8. **Egypt's farmers desperate for clean water**
[<http://edition.cnn.com/2010/WORLD/africa/11/09/egypt.water.shortage/index.html>]
9. **Fishery Country Profile, Arabic Republic of Egypt**. In: *Food and Agriculture Organization of the United Nations*. FAO; 2003.
10. **Sustainable development and water resources in Egypt: Translated page**
[http://www.sis.gov.eg/Ar/LastPage.aspx?Category_ID=1082]
11. Mezher T, Fath H, Abbas Z, Khaled A: **Techno-economic assessment and environmental impacts of desalination technologies**. *Desalination* 2011, **266**(1-3):263-273.
12. Lentz J: **Salinity**. In.: School of Coast and Environment, Louisiana State University; 2010.
13. Van der Bruggen B, Vandecasteele C: **Distillation vs. membrane filtration: overview of process evolutions in seawater desalination**. *Desalination* 2002, **143**(3):207-218.
14. Alyson Sagle BF: **Fundamentals of Membranes for Water Treatment**. *The Future of Desalination in Texas* 2004, **2**(363):137-154

15. Ma Q, Lu H: **Wind energy technologies integrated with desalination systems: Review and state-of-the-art.** *Desalination* 2011, **277**(1-3):274-280.
16. Corry B: **Designing Carbon Nanotube Membranes for Efficient Water Desalination.** *The Journal of Physical Chemistry B* 2007, **112**(5):1427-1434.
17. Mark LeChevallier K-KA: **Removal Process.** In: *Water Treatment and Pathogen Control: Process Efficiency in Achieving Safe Drinking Water.* World Health Organization; 2004: 33-39.
18. Darunee Bhongsuwan TB: **Preparation of Cellulose Acetate Membranes for Ultra-Nano- Filtrations.** *Kasetsart Journal: Natural Sciences* 2008(42):311 - 317.
19. Edward S. K. Chian JPC, Ping-Xin Sheng, Yen-Peng Ting, Lawrence K. Wang: **Reverse Osmosis Technology for Desalination.** In: *Handbook of Environmental Engineering: Advanced Physicochemical Treatments Technologies.* vol. 5, 1 edn: 329-366.
20. Lee KP, Arnot TC, Mattia D: **A review of reverse osmosis membrane materials for desalination—Development to date and future potential.** *Journal of Membrane Science* 2011, **370**(1-2):1-22.
21. Li Z, Ren J, Fane AG, Li DF, Wong F-S: **Influence of solvent on the structure and performance of cellulose acetate membranes.** *Journal of Membrane Science* 2006, **279**(1-2):601-607.
22. Ye SH, Watanabe J, Iwasaki Y, Ishihara K: **Novel cellulose acetate membrane blended with phospholipid polymer for hemocompatible filtration system.** *Journal of Membrane Science* 2002, **210**(2):411-421.
23. Haddad R, Ferjani E, Roudesli MS, Deratani A: **Properties of cellulose acetate nanofiltration membranes. Application to brackish water desalination.** *Desalination* 2004, **167**:403-409.
24. Boricha AG, Murthy ZVP: **Preparation of N,O-carboxymethyl chitosan/cellulose acetate blend nanofiltration membrane and testing its performance in treating industrial wastewater.** *Chemical Engineering Journal* 2010, **157**(2–3):393-400.
25. Cano-Odena A, Spilliers M, Dedroog T, De Grave K, Ramon J, Vankelecom IFJ: **Optimization of cellulose acetate nanofiltration membranes for micropollutant removal via genetic algorithms and high throughput experimentation.** *Journal of Membrane Science* 2011, **366**(1–2):25-32.
26. Lv C, Su Y, Wang Y, Ma X, Sun Q, Jiang Z: **Enhanced permeation performance of cellulose acetate ultrafiltration membrane by incorporation of Pluronic F127.** *Journal of Membrane Science* 2007, **294**(1–2):68-74.

27. Chen J, Li J, Zhan X, Han X, Chen C: **Effect of PEG additives on properties and morphologies of polyetherimide membranes prepared by phase inversion.** *Frontiers of Chemical Engineering in China* 2010, **4**(3):300-306.
28. Saljoughi E, Sadrzadeh M, Mohammadi T: **Effect of preparation variables on morphology and pure water permeation flux through asymmetric cellulose acetate membranes.** *Journal of Membrane Science* 2009, **326**(2):627-634.
29. Ani Idris KYL, H. K. Hing: **Preparation of cellulose acetate dialysis membrane for separation of bovine serum albumin.** *Jurnal Teknologi, Universiti Teknologi Malaysia* 2005(42 F):35-46.
30. Saljoughi E, Mohammadi T: **Cellulose acetate (CA)/polyvinylpyrrolidone (PVP) blend asymmetric membranes: Preparation, morphology and performance.** *Desalination* 2009, **249**(2):850-854.
31. Sivakumar M, Mohan DR, Rangarajan R: **Studies on cellulose acetate-polysulfone ultrafiltration membranes: II. Effect of additive concentration.** *Journal of Membrane Science* 2006, **268**(2):208-219.
32. Arthanareeswaran G, Sriyamuna Devi TK, Raajenthiren M: **Effect of silica particles on cellulose acetate blend ultrafiltration membranes: Part I.** *Separation and Purification Technology* 2008, **64**(1):38-47.
33. Chen W, Su Y, Zhang L, Shi Q, Peng J, Jiang Z: **In situ generated silica nanoparticles as pore-forming agent for enhanced permeability of cellulose acetate membranes.** *Journal of Membrane Science* 2010, **348**(1-2):75-83.
34. Mahendran R, Malaisamy R, Mohan DR: **Cellulose acetate and polyethersulfone blend ultrafiltration membranes. Part I: Preparation and characterizations.** *Polymers for Advanced Technologies* 2004, **15**(3):149-157.
35. Mänttari M, Pihlajamäki A, Nyström M: **Effect of pH on hydrophilicity and charge and their effect on the filtration efficiency of NF membranes at different pH.** *Journal of Membrane Science* 2006, **280**(1-2):311-320.
36. Rodrigues-Filho UP, Gushikem Y, Gonçalves MdC, Cachichi RC, de Castro SC: **Composite Membranes of Cellulose Acetate and Zirconium Dioxide: Preparation and Study of Physicochemical Characteristics.** *Chemistry of Materials* 1996, **8**(7):1375-1379.
37. Arthanareeswaran G, Thanikaivelan P: **Fabrication of cellulose acetate-zirconia hybrid membranes for ultrafiltration applications: Performance, structure and fouling analysis.** *Separation and Purification Technology* 2010, **74**(2):230-235.

38. Choi J-H, Jegal J, Kim W-N: **Fabrication and characterization of multi-walled carbon nanotubes/polymer blend membranes.** *Journal of Membrane Science* 2006, **284**(1-2):406-415.
39. Qiu S, Wu L, Pan X, Zhang L, Chen H, Gao C: **Preparation and properties of functionalized carbon nanotube/PSF blend ultrafiltration membranes.** *Journal of Membrane Science* 2009, **342**(1-2):165-172.
40. Tang C, Zhang Q, Wang K, Fu Q, Zhang C: **Water transport behavior of chitosan porous membranes containing multi-walled carbon nanotubes (MWNTs).** *Journal of Membrane Science* 2009, **337**(1-2):240-247.
41. Shawky HA, Chae S-R, Lin S, Wiesner MR: **Synthesis and characterization of a carbon nanotube/polymer nanocomposite membrane for water treatment.** *Desalination* 2011, **272**(1-3):46-50.
42. Wang Y, Yang L, Luo G, Dai Y: **Preparation of cellulose acetate membrane filled with metal oxide particles for the pervaporation separation of methanol/methyl tert-butyl ether mixtures.** *Chemical Engineering Journal* 2009, **146**(1):6-10.
43. Haddada R, Ferjani E, Roudesli MS, Deratani A: **Properties of cellulose acetate nanofiltration membranes. Application to brackish water desalination.** *Desalination* 2004, **167**:403-409.
44. B. McCray S, Vilker VL, Nobe K: **Reverse osmosis cellulose acetate membranes II. Dependence of transport properties on acetyl content.** *Journal of Membrane Science* 1991, **59**(3):317-330.
45. Suzana Pereira Nunes K-VP: **Membrane Technology: in the Chemical Industry**, 2 edn: Wiley-VCH; 2006.
46. Valente AJM, Polishchuk AY, Burrows HD, Lobo VMM: **Permeation of water as a tool for characterizing the effect of solvent, film thickness and water solubility in cellulose acetate membranes.** *European Polymer Journal* 2005, **41**(2):275-281.
47. Baker RW: **Reverse Osmosis.** In: *Membrane Technology and Applications.* Wiley; 2004: 197-200.
48. Kucera J: **Membranes.** In: *Reverse Osmosis: Design, Processes, and Applications for Engineers.* Wiley; 2010: 47-51.
49. Vogrin N, Stropnik C, Musil V, Brumen M: **The wet phase separation: the effect of cast solution thickness on the appearance of macrovoids in the membrane forming ternary cellulose acetate/acetone/water system.** *Journal of Membrane Science* 2002, **207**(1):139-141.

50. Su J, Zhang S, Chen H, Chen H, Jean YC, Chung T-S: **Effects of annealing on the microstructure and performance of cellulose acetate membranes for pressure-retarded osmosis processes.** *Journal of Membrane Science* 2010, **364**(1–2):344-353.
51. Baker R: **Membrane Technology and Applications:** Wiley; 2004.
52. Smolders CA, Reuvers AJ, Boom RM, Wienk IM: **Microstructures in phase-inversion membranes. Part 1. Formation of macrovoids.** *Journal of Membrane Science* 1992, **73**(2–3):259-275.
53. Kim HJ, Tyagi RK, Fouda AE, Ionasson K: **The kinetic study for asymmetric membrane formation via phase-inversion process.** *Journal of Applied Polymer Science* 1996, **62**(4):621-629.
54. Ren J, Wang R: **Preparation of Polymeric Membranes.** In: *Membrane and Desalination Technologies.* Edited by Wang LK, Chen JP, Hung Y-T, Shamma NK, vol. 13: Humana Press; 2008: 47-100.
55. Wara NM, Francis LF, Velamakanni BV: **Addition of alumina to cellulose acetate membranes.** *Journal of Membrane Science* 1995, **104**(1-2):43-49.
56. Aparecida da Silva C, Maria Favaro M, Pagotto Yoshida IV, do Carmo Gonçalves M: **Nanocomposites derived from cellulose acetate and highly branched alkoxysilane.** *Journal of Applied Polymer Science* 2011, **121**(5):2559-2566.
57. Damme HV: **Nanocomposites: The End of Compromise.** In: *Nanomaterials and nanochemistry.* Edited by Catherine Bréchnignac PH, Marcel Lahmani, vol. 2: Springer Berlin Heidelberg; 2008: 347-380.
58. A.E. Gash RLS, T.M. Tillofson, J.H. Safcher, L. W. Hrubesh: **Making Nanostructured Pyrotechnics in a Beaker.** In.: International Pyrotechnics Seminars, Grand Junction, CO; 2000.
59. Ajayan P: **Nanocomposite Science and Technology:** Wiley-VCH Verlag GmbH Co; 2003.
60. Erik T. Thostenson CL, Tsu-Wei Chou: **Nanocomposites in Context: Review.** *Composites Science and Technology* 2005(65):491–516.
61. Michler GH: **Polymer Nanocomposites.** In: *Electron Microscopy of Polymers* vol. 3: Springer Berlin Heidelberg; 2008: 419-428.
62. Xie X-L, Mai Y-W, Zhou X-P: **Dispersion and alignment of carbon nanotubes in polymer matrix: A review.** *Materials Science and Engineering: R: Reports* 2005, **49**(4):89-112.

63. Hirsch A, Vostrowsky O: **Functionalization of Carbon Nanotubes**. In: *Functional Molecular Nanostructures*. Edited by Schlüter AD, vol. 245: Springer Berlin / Heidelberg; 2005: 193-237.
64. Aleksandr Noya HGP, Francesco Fornasieroa, Jason K. Holta, Costas P. Grigoropoulosb, Olgica Bakajina: **Nanofluidics in carbon nanotubes: Review**. *Nanotoday* 2007, **2**(6):22-29.
65. Ahir SV, Huang YY, Terentjev EM: **Polymers with aligned carbon nanotubes: Active composite materials**. *Polymer* 2008, **49**(18):3841-3854.
66. Maser W, Benito AM, Muñoz E, Martínez MT: **Carbon Nanotubes: From Fundamental Nanoscale Objects Towards Functional Nanocomposites and Applications**. In: *Functionalized Nanoscale Materials, Devices and Systems*. Edited by Vaseashta A, Mihailescu IN: Springer Netherlands; 2008: 101-119.
67. **Various Carbon Forms** [<http://www.nano-enhanced-wholesale-technologies.com/faq/carbon-forms.htm>]
68. Alexiadis A, Kassinos S: **The density of water in carbon nanotubes**. *Chemical Engineering Science* 2008, **63**(8):2047-2056.
69. Thostenson ET, Li C, Chou T-W: **Nanocomposites in context**. *Composites Science and Technology* 2005, **65**(3-4):491-516.
70. Mohl M, Kónya Z, Kukovecz Á, Kiricsi I: **Functionalization of Multi-Walled Carbon Nanotubes (MWCNTS)**. In: *Functionalized Nanoscale Materials, Devices and Systems*. Edited by Vaseashta A, Mihailescu IN: Springer Netherlands; 2008: 365-368.
71. Gao C, Vo CD, Jin YZ, Li W, Armes SP: **Multihydroxy Polymer-Functionalized Carbon Nanotubes: Synthesis, Derivatization, and Metal Loading**. *Macromolecules* 2005, **38**(21):8634-8648.
72. Upadhyayula VKK, Deng S, Mitchell MC, Smith GB: **Application of carbon nanotube technology for removal of contaminants in drinking water: A review**. *Science of The Total Environment* 2009, **408**(1):1-13.
73. **Scientific basis for the definition of the term “nanomaterial”**. In. European Union: Scientific Committee on Emerging and Newly Identified Health Risks; European Commission; 2010.
74. John A. Thomas AJHM, Ottoleo Kuter-Arnebeck: **Pressure-driven water flow through carbon nanotubes: Insights from molecular dynamics simulation**. *International Journal of Thermal Sciences* 2010, **49**:281–289.

75. Hanasaki I: **Flow structure of water in carbon nanotubes: Poiseuille flow or plug-like?** *J Chem Phys* 2006, **124**(14):144708.
76. Kotsalis EM, Walther JH, Koumoutsakos P: **Multiphase water flow inside carbon nanotubes.** *International Journal of Multiphase Flow* 2004, **30**(7-8):995-1010.
77. Hummer G, Rasaiah JC, Noworyta JP: **Water conduction through the hydrophobic channel of a carbon nanotube.** *Nature* 2001, **414**(6860):188-190.
78. Liu Y: **Fluid structure and transport properties of water inside carbon nanotubes.** *J Chem Phys* 2005, **123**(23):234701.
79. Kalra A, Garde S, Hummer G: **Osmotic water transport through carbon nanotube membranes.** *Proceedings of the National Academy of Sciences* 2003, **100**(18):10175-10180.
80. Goodhew PJ, Humphreys FJ, Beanland R: **Electron Microscopy and Analysis, Third Edition:** Taylor & Francis Group; 2001.
81. Goldstein J: **Scanning Electron Microscopy and X-Ray Microanalysis:** Kluwer Academic Pub; 2003.
82. Everhart T: **Wide-Band Detector For Micro-Microampere Low-Energy Electron Currents.** *Journal of Scientific Instruments* 1960, **37**:246–248.
83. Bubert H, Jenett H: **Surface and Thin Film Analysis:** Wiley; 2011.
84. Allen T: **Particle Size Measurement: Volume 2: Surface Area and Pore Size Determination:** Springer; 1996.
85. **Gas Adsorption Theory.** In. Edited by Corporation MI: Micromeritics Instrumental Corporation.
86. **Gas Sorption Analysis** [<http://www.micromeritics.com/>]
87. Lowell S, Shields JE, Thomas MA, Thommes M: **Characterization of Porous Solids and Powders: Surface Area, Pore Size and Density:** Springer; 2006.
88. Lowell S, Shields JE: **Powder Surface Area and Porosity:** Springer; 1991.
89. Marsh H, Rodríguez-Reinoso F: **Activated Carbon:** Elsevier Science & Tech; 2006.
90. Gregg SJ, Sing KSW: **Adsorption, surface area, and porosity:** Academic Press; 1967.
91. Strickland ML: **Physical Adsorption Theory.** In.: Micromeritics Instrument Corp.

92. **Powder Tech Note 18**
[http://www.atomikateknik.com/pdf/QCI_PowderTech_18.pdf]
93. Condon JB: **Surface Area and Porosity Determinations by Physisorption: Measurements and Theory**: Elsevier Science; 2006.
94. Lastoskie CM, Gubbins KE: **Characterization of porous materials using density functional theory and molecular simulation**. In: *Studies in Surface Science and Catalysis*. Edited by K.K. Unger GK, Baselt JP, vol. Volume 128: Elsevier; 2000: 41-50.
95. **Micrometrics ASAP 2020** [<http://www.micromeritics.com/product-showcase/ASAP-2020-Physisorption.aspx>]
96. Stobinski L, Lesiak B, Kövér L, Tóth J, Biniak S, Trykowski G, Judek J: **Multiwall carbon nanotubes purification and oxidation by nitric acid studied by the FTIR and electron spectroscopy methods**. *Journal of Alloys and Compounds* 2010, **501**(1):77-84.
97. Coates J: **Interpretation of Infrared Spectra, A Practical Approach**. In: *Encyclopedia of Analytical Chemistry*. Edited by Meyers RA: John Wiley & Sons Ltd, Chichester; 2001: 10815–10837.
98. Li M, Kim I-H, Jeong YG: **Cellulose acetate/multiwalled carbon nanotube nanocomposites with improved mechanical, thermal, and electrical properties**. *Journal of Applied Polymer Science* 2010, **118**(4):2475-2481.

Appendix I

Unsuccessful Membranes

Permeation and salt retention rates measurements were carried out to evaluate membranes' performance and to find the best possible combination of conditions. The table below summarizes the unsuccessful membranes' preparation conditions that didn't allow permeation through the membranes at the maximum operating pressure used (55 bars).

Combination of conditions that failed to allow a permeation rate

CA%	Additive(s)	Additive %	ICT (μm)	ISE (sec)
13%	Water	0	1000	0
13%	Water	0	1000	30
13%	Water	0	1000	60
13%	Water	0	1200	0
13%	Water	0	1200	30
13%	pNT	0.5	1000	0
13%	Water	5	1000	0
13%	Water	5	1200	0
13%	Water	10	800	0
13%	Water	10	800	30
13%	Water	10	1000	0
14%	Water	0	1000	0
14%	Water	5	800	0
14%	Water	5	800	30
14%	Water	5	1000	0
14%	Water	10	800	0
15%	Water	0	600	0
15%	Water	0	700	0
15%	Water	0	800	0
15%	Water	0	900	0
15%	Water	5	300	0

CA%	Additive(s)	Additive %	ICT (μm)	ISE (sec)
15%	Water	10	400	0
15%	Water	10	500	0
15%	fNT + Water	0.5+20	300	0
15%	fNT + Water	0.05+21	300	0
15%	fNT + Water	0.05+22	360	0
15%	fNT + Water	0.05+23	400	0
15%	fNT + Water	0.05+24	500	0
15%	fNT + Water	0.05+24	550	0
17%	Water	0	500	0
17%	Water	0	600	0
17%	Water	0	700	0
17%	Water	0	800	0
17%	Water	0	1000	0
17%	pNT	0.5	1000	0
17%	pNT	1	1000	0
17%	Water	5	1000	0
17%	Water	5	1000	30
17%	Water	10	700	0
17%	Water	10	800	0
17%	Water	20	200	0
17%	Water	20	260	0
17%	Water	20	700	0